Interface Fracture Mechanics Of High Strength Concrete: Size Effect And Aggregate Roughness

by

Uwe Trende

Technische Universität Berlin, Germany

Submitted to the Department of Civil and Environmental Engineering
in partial fulfillment of the requirements for the degree of

Master of Science
in Civil and Environmental Engineering

at the

MASSACHUSETTS INSTITUTE OF TECHNOLOGY

February 1995

Author .....
Department of Civil and Environmental Engineering
January 19, 1995

Certified by ....
Oral Büyüköztürk
Professor, Department of Civil and Environmental Engineering
Thesis Supervisor

Accepted by .....
Joseph M. Sussmann
Chairman, Departmental Committee on Graduate Students

Interface Fracture Mechanics Of High Strength Concrete: Size Effect And Aggregate Roughness

by

Uwe Trende

Submitted to the Department of Civil and Environmental Engineering
on January 19, 1995, in partial fulfillment of the
requirements for the degree of
Master of Science
in Civil and Environmental Engineering

Abstract

The properties of concrete are strongly dependent on the nature of the aggregate–cement paste interfacial zone. By lowering the water–cement ratio and introducing silica fume into the mix, high strength concrete is produced. Such concretes have very dense and strong interfaces but are less ductile than normal strength concretes. In order to improve the material's ductility an interface fracture mechanics concept must be developed to thoroughly study interfaces in high strength concretes. The objectives of the research reported in this thesis were threefold: (1) to investigate the size scale effect on interface fracture, (2) to study the effect of aggregate roughness, and (3) to establish more interface fracture data for different material combinations.

I developed a Compact Sandwiched Beam Specimen, which is based on the previously used Sandwiched Four Point Bending Test Specimen. Specimens were manufactured in three different sizes with all dimensions in the ratio 1:2:3. The materials were a high strength mortar combined with Mason or Chelmsford granite. The surfaces of the aggregate were smooth, sandblasted, and flamed. I also varied the portion of opening to shear at the interface to establish fracture toughness curves as a function of the loading angle.

The results show a strong size effect that complies with Bažant's size effect law. Increasing aggregate roughness has noticeable effect on the fracture energy release rate in pure Mode I and a strong effect at higher loading angles due to the shielding effect.

Keywords: Interface fracture mechanics, high strength concrete, interfacial zone, size scale effect, aggregate roughness.

Thesis Supervisor: Oral Büyüköztürk
Title: Professor, Department of Civil and Environmental Engineering

To Margareta

Acknowledgments

I should like to thank my thesis supervisor, Professor Oral Büyüköztürk, for his support and guidance throughout the twelve months of my research. Thanks also go to Professor A. G. Evans and Professor J. W. Hutchinson of Harvard University for their contributions to my understanding of interface fracture mechanics. Professor C. K. Y. Leung of MIT is to be thanked for his valuable comments on this work. I would also like to thank Professor K. M. Lee, who, while a Ph.D. student at MIT, helped pioneer the application of interface fracture mechanics to high strength concrete composites. This work is a continuation of his. I greatly appreciate his suggestions.

My appreciation is extended to Arthur and Stephen Rudolph of the machine shop for their help with technical questions, especially when the equipment caused trouble. I also wish to thank Matt Sandholm, who in his Undergraduate Research Opportunity Project helped carry out the final test series.

This work was partially supported by the National Science Foundation, Grant No. MSS-9313062. Additional funding was provided by the German American Society with the Quadrille Ball Scholarship. I want to thank Mr. John Baretto from Fletcher Granite Co., Mr. Glenn Shaefer from W. R. Grace & Co., and Boston Sand & Gravel Co. for providing most of the materials for this study.

I am very grateful to the Technical University of Berlin, Germany, for providing the support for the first two semesters of my stay at MIT. I am also indebted to the many people at TUB who helped and encouraged me to pursue my studies at MIT, among them my friend Kai Haase, Professor M. Specht, Professor J. Pahl, and Professor S. Savidis. Special thanks go to Jutta Gbur and Astrid Peter at the International Students Office of TUB for their commitment during the application and grant awarding procedure.

Nathan is to be thanked for his helpful comments and his company. He has shared the lab with me while there was a wonderful summer outside... I am very grateful to my friend Daniel, with whom I enjoyed what one should not expect at MIT: a social life. His wonderful dishes kept me alive, and so did his belay. While thousands of miles away, Margareta has provided the energy for all of this. I hope that this phenomenon is not restricted to a single undertaking, that it will not vanish when the distance does, and that it works both ways. My most profound thanks go to my father and mother, who have the greatest share in what you hold in your hands. It was my best idea to chose them as parents, and I have been trying ever since to make my more conscious decisions at least half as good.

Contents

List of Figures

List of Tables

Conversion of Units

Metric		Imperial
1 cm	=	0.3937 inches
1 MPa	=	145.00 psi

Nomenclature

a	crack length
E_i	Young's modulus of material i
ν_i	Poisson's ratio of material i
$\bar{E}_i$	$E_i/(1-\nu_i^2)$
G	energy release rate
h	thickness of aggregate layer
$K = K_1 + iK_2$	interface stress intensity factor
$K^\infty = K_I + K_{II}$	apparent stress intensity factor
$l, b, d,$	structure size: length, depth, height
a/d	relative crack lenght
S_0, S_1, S_2	loading geometry
P	fracture load
$\hat{L}$	fixed length for reporting fracture data
α, β	Dundurs' elastic moduli mismatch parameters
Γ_i	interface fracture toughness
δ_1, δ_2	crack face displacements
ϵ	oscillation index
σ_{22}, σ_{12}	normal stress and shear stress
ϕ	$\arctan(K_{II}/K_I)$
ψ	phase angle of $KL^{i\epsilon}$
$\hat{\psi}$	phase angle of $K\hat{L}^{i\epsilon}$
ψ^*	phase angle of $Kh^{i\epsilon}$
$\omega(\alpha, \beta)$	phase shift in sandwich specimen.

Chapter 1

Introduction

1.1 Problem Definition

Despite significant advances in concrete construction technology over the past 50 years, utilized concrete strengths have essentially stayed the same in a range of 20 to 40 MPa (2,900 to 5,800 psi). High strength concretes with compressive strengths of up to 140 MPa (20,300 psi) using standard technology and of up to 650 Mpa (94,250 psi) using special laboratory technology, such as warm pressing, have been developed during the past 15 years. There are several methods of producing high strength concrete. The most common of these methods is based on the reduction of the water–cement ratio to values as low as 0.2, which is only possible through the use of superplastizisers, and the introduction of mineral admixtures, such as silica fume, into the mix. Such changes lead to dense and less porous interfacial zones between the aggregate and the cement paste, which, in turn, results in higher compressive strengths.

High strength concrete (HSC) has the potential to reduce the cross–sectional area of columns and beams and can, therefore, help maximize the rentable space in a building and reduce the dead weight. Taking advantage of the high early strength one can achieve short concreting cycles that allow for shorter construction times. The high Young's moduli of HSC result in less elastic column shortening and less creep. High strength concrete is also more durable with respect to aggressive environments and

freeze–thaw cycles than normal strength concrete. However, the applications of high strength concrete are still limited. Design engineers and construction companies are reluctant to use high strength concrete. This is not because the use of high strength concrete would be inefficient, but because the material exhibits several undesired characteristics, with the lack of sufficient ductility and tensile strength as the most serious ones. Unreinforced high strength concrete fails in a brittle or even explosive manner, whereas normal strength concrete shows a pronounced post–peak strain–softening.

This increase in brittleness may be attributed to the same characteristics that are responsible for the high compressive strength of HSC: strong aggregate–mortar interfaces. For normal strength concrete, one observes multiple, distributed cracking and localization of cracking prior to failure into larger fractures. Cracks usually propagate around aggregate particles. In contrast, cracking in high strength concrete starts at much higher relative stress levels and is more likely to be localized into a single crack from early on with cracks generally propagating through aggregate particles. Comparably little energy is absorbed by crack formation, and failure occurs after little deformation.

It is the overall goal to improve the ductility of high strength concretes without having to give up the high compressive strength, Young's modulus, and durability. One could try to alter the interfaces so that they are still strong enough to make high strength concrete but weak enough to allow cracks to travel around aggregate particles, therefore dissipating more energy prior to failure. Also, polymer solutions could be used to toughen the cement paste and the interfacial zone. Other concepts would be to introduce crack arrestors into the mix that consist of tough, rubberlike material to inhibit localized crack propagation or to select an aggregate with its properties, such as compressive strength, tensile strength, fracture energy, surface roughness, adsorption, shape, and size, at an optimum.

However, we are not at that stage yet. The questions that need to be answered first are: Can we find the optimal values of the abovementioned aggregate properties? What are the interfacial properties of high strength concrete depending on the ag-

gregate used? How do these parameters depend on the loading angle, the portion of pure opening to pure shear, at the interface? How important is the size scale effect? Can we establish a universal interface fracture mechanics approach to the problem?

This work contributes information on the basic understanding of interface fracture in high strength concrete composites. It establishes data for different aggregates, their surfaces, loading conditions, and specimen sizes.

1.2 Background

1.2.1 High Strength Concrete and the Interfacial Zone

High strength concretes have compressive strength in excess of 69 MPa (10,000 psi).[1] They are frequently referred to as high performance concrete, with the implication of high compressive strength and high durability. In this thesis, the term high strength concrete is used but could as well be replaced with high performance concrete.
There are two methods of producing high strength concrete:

1. Lowering the water–cement ratio[2] to values as low as 0.2 or less and careful material selection.

2. Introducing mineral admixtures into the mix such as silica fume and fly ash.

The first method is successful for the following reasons. In fresh normal strength concrete, bleeding water collects on the surface of aggregate particles. Not all of this water is used during the hydration reaction. Excess water will evaporate, leaving behind pores. The interfacial zone is further weakened by autogeneous shrinkage[3] and differential thermal shrinkage. During later stages of the reaction, the pores are partly filled by large calciumhydroxide and ettringite crystals, and effect called autogeneous healing. However, the aggregate–cement paste interface remains porous

[1] From the definition at the workshop held in Chicago in 1979.

[2] The term water–cement ratio is used in this thesis with the implication that mineral admixtures are taken into account. It should read more precisely water–cementitious materials ratio.

[3] The hydrated cement gel has a smaller volume than the sum of cement and water.

and may be considered the weak link in normal strength concrete. This can also be seen from the propagation of cracks along these interfaces instead of through the bulk paste or the aggregate. Therefore, attempts have been made to improve the interface strength by lowering the amount of bleeding water at the interface and reducing the pore size as well as the size of the crystals growing in the phase of autogeneous healing. Low water–cementitious materials ratios can only be employed using superplastizisers, such as high range water reducers on the basis of naphthalene sulfonate, to maintain a workable concrete mix. With water–cementitious materials ratios below about 0.38[4], some cement will remain unhydrated within the hardened concrete. However, a significant reduction in bleeding and, therefore, porosity is achieved, resulting in denser and stronger interfaces.

The second method is based on the small size, large surface area, and pozzolanic nature of mineral admixtures such as silica fume and fly ash. The main contribution to strength is the filler action of these particles. They also reduce bleeding, serve as condensation spots for crystals, which results in smaller and less oriented crystals, and react themselves chemically with some of those compounds. [*Chatterji et al.* (1992)]

For a more in-depth coverage of high strength concrete and the interfacial zone refer to Chapter 2.

1.2.2 Fracture Mechanics and Size Effect

Concrete structures are full of cracks. Cracks usually form as early as during hydration due to the mismatch in the thermal expansion coefficients of cement paste and aggregate material. These initial cracks are often closed during further crystal growth at the interfaces, an effect called autogeneous healing. However, micro- and macrocracks are generally present in concrete. This is known and accounted for by design code provisions for strength and minimum reinforcement.

The existing cracks typically develop into larger, spreaded cracking zones while growing stable until large fractures form just before failure. However, concrete design

[4]This number is reported differently in the literature. It depends on the cement, the aggregate, the curing, and the environmental conditions.

is not based on fracture mechanics, although fracture mechanics concepts have been available for more than half a century. Nevertheless, these theories are only applicable to homogeneous and brittle materials such as glass and to homogeneous brittle–ductile materials such as metals.

A fracture mechanics theory for concrete must account for inhomogeneity, strain–softening as a result of distributed cracking, localization of cracking, and possible bridging stresses across the crack tip. Such theories have been available for the past ten or so years.

It is widely believed among fracture researchers that the introduction of fracture mechanics into concrete design will have significant gains in terms of more uniform safety margins. It would be desirable that fracture mechanics be applied to all brittle types of failure, such as shear (punching and diagonal), pull out, torsion, and for failures of large structures, such as dams and nuclear reactor vessels.

Equally important is the consideration of the fracture mechanics size effect. The size effect simply states that a structure twice the size will fail at less than twice the load. In other words, the nominal stress at failure becomes less with increasing structure size. This is due to a greater energy release into a localized crack from the strain energy stored within the structure. The size effect is not of a statistical nature. Current design practice neglects the size effect. Since most of the calibrating tests for building code provisions are done on laboratory scale, the size effect clearly results in an overestimation of the strength of large structures.

For further treatment of fracture mechanics and the size effect, refer to Chapter 3 and Chapter 5, respectively.

1.3 Research Objective

The objectives of my research were to

1. investigate the size effect on interface fracture of high strength mortar–granite composites as a concrete model,

2. evaluate the influence of aggregate roughness on interface fracture parameters, and

3. generate additional interface fracture data for certain high strength mortar–aggregate combinations.

This is a fundamental study of the fracture behavior of mortar–aggregate interfaces in high strength concrete and is essentially a continuation of the work of K. M. Lee [*Lee* (1993)].

General Approach

The general approach to the development of high strength concrete via an interface fracture mechanics approach is as follows.

First, interfacial toughness data for a variety of mortar–aggregate combinations are established. This involves the development of a physical model, an interface fracture mechanics analysis, and a microstructural study. The necessary data is to be drawn from experiments on suitable specimens. Second, a study of the crack propagation in the interfacial region must be undertaken. Numerical and experimental methods need to be employed to establish criteria that predict crack deflection versus kinking of the crack out of the interface. Third, with the knowledge of the two previous stages of the research it should be possible to make recommendations for the material selection for high strength concrete with improved ductility and tensile strength.

This study is part of the first stage as it investigates the fundamental nature of interfaces in high strength concrete to establish fracture parameters and information on the influence of specimen size and aggregate roughness on those fracture parameters. The major task was to investigate the size scale effect of interface fracture.

1.4 Research Approach

This work is essentially experimental. A linear elastic interface fracture mechanics theory as developed by Hutchinson and his co–workers [*Hutchinson et al.* 1992,*Hutchinson* 1990] is used to process the data from fracture tests. The specimens were sandwiched four–point bending beams and newly developed compact sandwiched beams. They consist of an aggregate layer bearing an artificial crack in form of a layer of epoxy resin embedded in high strength mortar. Specimens were manufactured in three sizes with all dimensions in the ratio of 1:2:3. Three different roughnesses were used for the aggregate: diamond saw cut, sandblasted, and flamed surfaces. The specimens were tested with the loading angle, a measure of the contribution of Mode I vs. Mode II, at about 0° (pure Mode I), 30°, and 60°. The evaluation of the size effect was made on the basis of Bažant's size effect law [*Bažant* (1992)].
Refer to Chapter 7 for more detailed information about the research approach.

1.5 Thesis Organization

Chapter 1 provides the general background of this work, its motivation, and the research approach.

Chapter 2 reviews pertinent literature on high strength concrete, with regard to production, material selection, and properties, and examines the characteristics of interfaces and interface fracture in normal and high strength concrete.

Chapter 3 reviews the interface fracture mechanics theory as applicable to mortar–aggregate systems.

Chapter 4 explains the theoretical background of several interface fracture test specimens.

Chapter 5 studies the size effect and Bažant's size effect law.

Chapter 6 contains all information regarding the experimental work: specimens, materials, testing procedure.

Chapter 7 reports test results in form of tables and graphs and procedures for the necessary calculations for fracture parameters and size effect.

Chapter 8 summarizes the test results and concludes the work.

Since Chapters 2, 3, and 5 are reviews, the reader familiar with the topics may skip them and refer directly to Chapter 7 and Chapter 8.

Chapter 2

High Strength Concrete

This chapter reviews the state of the art in high strength concrete (HSC) technology. It provides information on the production of HSC, its properties, its applications, and compares HSC to normal strength concrete (NSC). Also, the nature of aggregate–paste interfaces in HSC and NSC are discussed.

2.1 Introduction

Most structural concrete applications call for 20 to 40 MPa compressive strength. However, the use of HSC is gaining wider acceptance. The first 50 MPa concrete was made industrially in 1965 for columns for the Lake Point Tower in Chicago. In the 1970's, a 60 MPa concrete was utilized for columns in the lower 28 of 70 stories of Chicago's Water Tower building, and a 75 MPa concrete was used in the River Plaza. The Chicago Mercantile Building (1982) contains some 100 MPa concrete. An experimental column in 225 W. Wacker Drive in Chicago is made of 117 MPa concrete. In the 1980's, several buildings in New York used 50–80 MPa concrete. The Nova Scotia Plaza building in Toronto contains 90 MPa concrete [*Ryell et al.* (1987)]. In Seattle, 120 MPa and 131 MPa concretes were used for elements in the Two Union Square building and the Pacific First Center building, respectively [*Mehta et al.* (1990), *Randall et al.* (1989)]. In Norway, HSC is extensively being used for the construction and repair of pavements. Strengths of up to

140 MPa are reported [*Danielsen* (1987b)].

The above mentioned applications incorporated standard materials and used standard technology. Using more sophisticated materials[1] and technologies,[2] some researchers have arrived at 600 MPa compressive strengths [*Leung* (1993)]. See Table 2.1 on page 44.

2.2 Definition

Concretes with compressive strength in excess of 69 MPa (10,000 psi) are called high strength concretes or high performance concretes, with the implication of high compressive strength and high durability or other improved properties. In this thesis, the term high strength concrete is used because high compressive strength is the only property on which there is consensus in the literature. Some researchers arrive at somewhat contradicting conclusions about the service performance of HSC, especially with respect to the freeze–thaw resistance of HSC [*Hammer et al.* (1990), *Sellevold* (1987)].

2.3 Advantages

High strength concrete can be produced to have certain desired properties. Most of all, as the name suggests, HSC has a higher compressive strength than normal strength concrete. This property can be utilized to reduce the cross–sectional area of columns, beams, and walls. Such a reduction results in lower structure weight and can increase the rentable space. Another important property of HSC, the high Young's modulus, can result in less column shortening due to elastic deformation. Also, the long–term behavior of HSC can be influenced favorably. HSC can have less creep and less shrinkage than normal strength concrete. HSC is generally less permeable than NSC, making it more durable in severe environments and requiring a smaller

[1] For example, perfectly graded calcinated bauxite or carborundum
[2] High temperature curing and pressure compacting, for example.

concrete cover to protect reinforcing steel. Making use of the high early strength of HSC, one can achieve short concreting cycles and, therefore, shorter construction times. HSC has a higher abrasion resistance than NSC, can have a better freeze–thaw performance, and may incorpo rate aggregate that is recycled or of inferior quality. HSC is less likely to show segregation and bleeding.

2.4 Application

Preferred applications of high strength concrete include:

- Concreting where normal strength concrete may segregate or bleed,
- Sewer pipes and waste water treatment structures,
- Slabs and beams, especially prestressed,
- Columns and composite columns,
- Bridge decks and pylons,
- Dam spillway bases,
- Tunnel linings,
- Shells,
- Arches,
- Road pavements,
- Offshore structures,
- Pipes and floating bridges,
- Nuclear radiation shielding concrete,
- Trusses, space frames and tubular structures,
- Complex shapes that involve thin cross–sections and high local stresses.

The use of light–weight aggregate is very promising. In Norway, many projects already utilize LC55.[3] A future project for a two–span cantilever concrete bridge with a main span of 420 m is under investigation. The bridge will use C85, LC55, C55, and C45 for different parts of the structure, thus achieving savings of up to 6% of the total cost as compared to a bridge using a single concrete type. A comparable cable–stayed bridge would cost an estimated 23% more. [*Jakobsen et al.* (1987)]

2.5 Disadvantages

Unfortunately, the tensile strength of concrete does not increase proportionally to the compressive strength. High strength concrete is more brittle than normal strength concrete. This characteristic limits the current use of HSC to a far extent. It is the subject of many research projects, including this one, to improve the ductility of HSC so that it can find a broader range of applications. The tensile strength of NSC is roughly one seventh, while for HSC the tensile strength is about one tenth of the respective compressive strength. Less energy is dissipated during crack formation, which results in a relatively low fracture toughness. HSC may fail in a highly undesirable explosive manner. One may argue that reinforcement can provide sufficient ductility for a structure. However, the strength of the concrete and the reinforcing steel are usually considered separately, and the exact influence of reinforcement on the ductility of plain concrete is not well known yet.

Other disadvantages of HSC include: the higher material cost (higher cement content, higher quality aggregate, presence of mineral admixtures, superplasticizers, and retarder), elaborate quality control, higher hydration heat, lesser workability, stronger dependence on curing conditions, limited knowledge about the long–term behavior, and the characteristic dark gray to black color.

[3]The European notation has a C for concrete, LC for leightweight concrete, followed by the specified 28–day compressive strength.

2.6 The Strength of Brittle Solids: Principles

Because of the highly complex microstructure of concrete, microstructure–property relations are not fully developed for concrete. Nevertheless, some fundamental principles that govern the behavior of other brittle solids that show microstructural similarities to concrete, such as ceramics, can be applied to describe the microstructure and properties of concrete.

The dependence of the tensile strength on the porosity of a single phase crystalline material is generally expressed by the exponential relation $S = S_0 e^{-bP}$, where S is the tensile strength of the material with a porosity P, S_0 is the tensile strength of the same material at zero porosity, and b is a factor depending on the shape and size of the pores [*Mehta et al.* (1990)]. Other important factors that influence the strength of concrete are the size of the grains and the presence of inhomogeneities.

The tensile strength of brittle solids is usually much lower than the compressive strength. In tension, the material can fracture by propagation of a single crack that develops from a flaw or a microcrack. In contrast, several tensile cracks must coalesce before failure occurs in compression, thereby dissipating more energy. It can be predicted[4] that the compressive strength of a homogeneous ceramic is about eight times higher than the tensile strength. [*Mehta et al.* (1990)]

From empirical studies, many researchers have reported that the data for compressive strengths can be fitted with the equation $C = C_0(1 - P)^m$, where C is the compressive strength of the concrete at the porosity P, C_0 is the compressive strength at zero porosity, and m is a factor depending on the shape and size of pores and flaws, intercrystalline bonding, grain size, and the presence of impurities. Compressive strength generally increases with decreasing pore size and with decreasing grain size.

Rice [*Rice et al.* (1977)] noted that while most other properties are closely related to averages rather than extremes of the microstructural features, strength and fracture

[4]Using the Griffith tensile fracture criterion, the assumption that the compressive failure is a multiple of several tensile failures, and concepts of continuum mechanics. [*Rice et al.* (1977)]

depend critically on microstructural extremes, such as pore size. One could say that fracture is a weak link problem, especially in compression[5] [*Mehta et al.* (1990)]. Therefore, the number, size, shape, concentration, and spatial relation of pores are controlling factors in concrete.

2.7 Production of High Strength Concrete

High strength concrete is generally characterized by a low water–binder ratio[6], a moderate to high cement content, and the presence of several admixtures such as superplasticizer, retarder, and, most of all, mineral admixtures, such as silica fume, fly ash, and blast furnace slag. The mix proportions for HSC are generally derived from empirical laboratory tests. There are no guidelines for the production of HSC like the ACI[7]211 "Recommended Practice for Selecting Proportions for Concrete Mixtures"[8] for normal strength concrete.

2.7.1 Materials and Material Selection

Cement

Most high strength concrete is produced with regular Portland cement, Type I.[9] However, the cements meeting the ASTM[10] Standard Specification 150 may vary considerably in fineness and chemical composition, which can result in problems when making HSC. Furthermore, some cements show chemical or physical interactions with some water–reducing admixtures. An undesired consequence is the rapid stiffening of fresh concrete, which requires the addition of water. Since low water–binder ratios are of utmost importance, this problem will be further studied here.

[5] We will see in Section 5.2 that this statement is not really true, since concrete undergoes significant redistribution of stresses before fracture.

[6] Also called water/cementitious materials ratio.

[7] American Concrete Institute

[8] Covers concretes with compressive strengths in the range of 13 – 40 MPa.

[9] Type I cement is standard cement, used for 28–day compressive strength, normal environments, and normal hydration heat. Other types include low hydration heat cement, high early strength cement, and low sulfate cement.

[10] American Standard for Testing Materials

When water is added to cement, calcium sulfate (C_3S, C_2S) and tricalcium aluminate (C_3A)are among the first anhydrous phases that go into solution. Normal cement has gypsum (calcium sulfate) added to it to slow down the reaction of tricalcium aluminate with water to tricalcium aluminate hydrate (C_3AH_6) in order to prevent the so-called flash set. As a result, within the first minutes, ettringite is formed by tricalcium aluminate and calcium sulfate ($C_3A + 3C\bar{S} + 32H \rightarrow C_6A\bar{S}_3H_{32}$). Due to its low solubility, ettringite precipitates out. In addition to the formation of ettringite, flocs of precipitating crystals and poorly crystallized ettringite with high surface adsorption binds, entraps, and immobilizes a considerable amount of free water. Consequently, the rate at which cement paste loses its consistency depends mostly on the rate of ettringite formation and the morphology of the crystalline product. [*Mehta et al.* (1990)]

From these considerations and a test series undertaken by Hanna [1989], it may be concluded that high C_3A contents in cement are less favorable for the production of HSC. Furthermore, with high C_3A cements, high fineness, sulfate and alkali contents enhanced the rapid stiffening reaction. The procedure used by Hanna involving the Rheopump and the Marsh Cone offers a good tool to test certain cements for their suitability to produce HSC. When high early strengths are desired, it is better to use finely ground Type II cement instead of Type I or III because the latter contains often more than 8% C_3A. Cements with a very low C_3A content (Type V) usually contain a considerable amount of tetracalcium aluminoferrit (C_4AF), which may result in very slow setting.

Also, high pozzolan cements such as Portland pozzolan (Type IP) and Portland–slag (Type IS) may be used for HSC.

Mineral Admixtures

Although it is generally possible to produce HSC without mineral admixtures,[11] most high strength concretes will incorporate mineral admixtures. First, concretes with

[11] For example, an 87 MPa concrete containing 570 kg/m^3 and no mineral admixtures was produced by Aitcin et al. [*Mat*(1987)]

more than 500 kg/m^3 cement tend to be very sticky and difficult to handle. Second, the excessive heat development in such concretes will lead to thermal cracks in thick cross-sections unless costly preventive measures are taken[12], and third, such concretes are more expensive than those with mineral admixtures.

Generally, 10-25% of the cement content is replaced by one or more mineral admixtures. Those concretes have better workability, less heat of hydration, higher compressive strength, and usually better durability. Mineral admixtures can be classified in three basic groups:

1.	cementitious	granulated or pelletized blast furnace slag high-calcium fly ash
2.	pozzolanic	low-calcium fly ash, volcanic glasses and tuffs calcined clays, diatomaceous earth
3.	reactive pozzolanic	condensed silica fume, rice hull ash

For a more thorough coverage of mineral admixtures, refer to Figure 2-1. Mineral admixtures generally have a smaller particle size and a higher relative surface area than cement. The mineralogical composition is similar to silicate glasses or noncrystalline silica, which eventually hydrate to form cementitious products in the presence of calcium and hydroxyl ions.

Silica fume (SF) is a by-product of the production of silicon and ferrosilicon alloys in electric arc furnaces from the reduction of high-purity quartz with coal. The gas, consisting of almost pure silicondioxide (SiO_2), is collected and condensed. Condensed silica fume has very small, spherical particles of about 0.01 - 1 μm. The surface area is of the order of 20,000 m^2/kg, compared to fly ash with 400-700m^2/kg and cement with 300-400 m^2/kg. The specific gravity of SF is about 2.2, compared to 3.1 for Portland cement, and the bulk density is about 250-300 kg/m^3, compared to about 1,200 kg/m^3 for Portland cement. [*226* (1987)]

The incorporation of fine particles generally leads to improved workability and cohesiveness. Probably the most important function of the fine particles is filler

[12]Like reinforcement and cooling.

action [*Nilsen et al.* (1992), *Sellevold* (1987)]. Pores are filled by the silica fume particles, especially in the vicinity of aggregate grains. However, the total pore volume stays unchanged, according to [*Sellevold* (1987)], but is subdivided into smaller pores. An important consequence is reduction in bleeding, which normally takes place via small channels between the aggregate particles and the cement paste. The same phenomenon reduces the tendency of the mix to segregate. By the drastic reduction of bleeding and segregation, two major sources of inhomogeneity are drastically reduced.

Small particles also act as nucleation sites for the precipitation of crystalline hydration products. This leads to smaller, better dispersed, and directionally less oriented crystals. These effects are among the major reasons for the improved properties of aggregate/cement paste interfaces. A 10% addition[13] of mineral admixtures results in approximately 20% higher 28–day compressive strengths [*Mehta et al.* (1990)]. Since this increase is also true for pure carbon black, which is non–reactive, it seems that the filler action is the key function of mineral admixtures, and that the pozzolanic reaction becomes more important at later stages of hydration [*Detwiler et al.* (1989)].

In conjuntion with lower water/binder ratios, the introduction of mineral admixtures into the concrete mix leads to smaller transition zones between the aggregate particles and the bulk cement paste. A simplified representation of the transition zone in normal strength concrete is shown in Figure 2-4. While the transition zone width in NSC is about 50 to 100 μm, it reduces to about 20 to 50 μm in HSC [*Mehta et al.* (1990), *Maso* (1992), *Alexander et al.* (1992b)]. See also Section 7.5.1 for results of X–ray diffraction measurements of the width of the interfacial zone.

Besides the more important physical effects, condensed silica fume and fly ash are pozzolanic, as mentioned above. Silica fume reacts with free lime (calcium hydroxide) to form calcium silicate hydrate (CSH) [*Mehta et al.* (1990), *Sellevold* (1987)]. It was also shown [*Sellevold et al.* (1982)] that a SF content of about 24% by weight of cement eliminates the free calcium hydroxide in the hardened cement paste. This research suggests a possible upper limit for SF contents in concrete, since calcium hydroxide provides most of the corrosion protection for reinforcing steel.

[13]By weight of the cement.

As a summary, mineral admixtures improve the rheological properties of fresh concrete, reduce bleeding and segregation, and reduce the size of pores and crystalline products, leading to a denser and stronger concrete that can also show improved durability and abrasion resistance.

Aggregate

For the production of HSC, more attention must be given to the selection of fine and coarse aggregate than for normal strength concrete. The major properties of the aggregate are: compressive strength, grading, shape, adsorption, mineralogy, and maximum size. To keep the water demand of the aggregate as low as possible, only well graded fine and coarse aggregate should be used. As fine aggregate, any natural sand or crushed rock is possible. Since clay and silt should not be present, it is best to use only washed aggregate. Concretes as rich in fine particles as HSC do not need very fine sand; on the contrary, the fineness modulus[14] was found to be at best between 2.4 and 2.9, with the higher value preferred because coarse sands help keep the water demand low.

It is more problematic to select suitable coarse aggregate. In general, crushed rock[15] can always be used. It is usually more expensive than gravel. The disadvantage of gravel is that it almost always contains microcracks resulting from the size reduction process. However, it is reported that a 120 MPa concrete was made in the Northwestern U.S. from a glacial gravel that apparently contained no microcracks. [*Mehta et al.* (1990)]

There is no uniform opinion regarding the maximum aggregate size (MSA). Some researchers conclude that an MSA of about 12 to 20 mm is optimal [*Mehta et al.* (1990), *Leung* (1993)], whereas others claim that the optimal MSA for HSC made with superplasticizer is the same as that for normal strength concrete, namely 20 to 25 mm [*de Larrard et al.* (1992)]. From considerations of the size effect that takes the max-

[14]Described closer in Table 6.1.

[15]For example from granite, syenit, gabbro, diabase, basalt, limestone, sandstone, quartzite, rhyolite, andesite.

imum aggregate size into account, Bažant concludes that a small MSA is better for smaller structures and that larger MSA are beneficial for large structures, for example dams. [*Bažant* (1992)] For practical purposes it may be stated that with a stronger aggregate, a higher MSA can be used.

This leads us to the topic of mineralogy. In a recent study [*Aïtcin et al.* (1990)], four different coarse aggregates were compared: granite, gravel, diabase, and limestone. The results show that the concrete made with limestone yielded the highest compressive strength, followed by diabase, gravel, and granite.[16] The high strength of the limestone concrete may be attributed to the chemical interaction of the cement paste with the aggregate, besides its high compressive strength and Young's modulus [*Monteiro et al.* (1986)]. It is known that the presence of mica (muscovite and biotite) and laumontite is detrimenta

l to the concrete quality [*Danielsen* (1987a)].

Some researchers believe that the shape of the aggregate is more important to concrete strength than its roughness [*Saouma et al.* (1989)]. Generally, equidimensional particles are best. Aggregates for HSC will usually be crushed, with the exception of gravel, which appears to perform not as well as crushed aggregate. With gravel, one often observes intergranular fracture [*Mehta et al.* (1990)]. The compressive strength of the aggregate should be in the range of 120–300 MPa [*Danielsen* (1987a)].

Chemical Admixtures

A large number of chemical admixtures has been developed to accomplish various objectives. Of highest interest for the production of high–strength concrete is the reduction of the water content. At the same time, a good workability of the fresh concrete should be maintained. The water–cement system has a tendency to form flocs in which large amounts of water are entrapped. This entrapped water does not

[16]The compressive strengths of the concretes were 101 MPa, 97 MPa, 92 MPa, and 85 MPa, respectively. The mix proportions were: 500 kg/m^3 Portland Type I cement, 42 kg/m^3 condensed silica fume, 137.5 kg/m^3 water, 10.6 l/m^3 naphtalene sulfonate type superplasticizer, 675 kg/m^3 sand (fineness modulus 2.75), and 1130 kg/m^3 coarse aggregate. The MSA was 10 mm, except for the granite with 14 mm.

contribute to the workability of the mix, moreover, it is likely to produce regions of higher porosity. Since the water is entrapped mostly because of its high surface tension, the use of surfactants recommends itself.

There are many water-reducing agents on the market. Most important of those are the so-called superplasticizers, which are derived from naphtalene or melamine sulfonate formaldehyde. Superplasticizers have a high molecular weight, are anionic, and have a large number of polar groups in the hydrocarbon chain. The superplasticizers are adsorbed on the cement particles and prevent, with their large negative charges, the attraction of cement particles, therefore resulting in a better dissipation of cement particles within the fresh concrete. At the same time, the surface tension of the water molecules is reduced. [*Leung* (1993), *Mehta et al.* (1990)]

Superplasticizers are almost mandatory for the production of high quality high-strength concrete. Their contribution to low water-cement ratios, to high workability, and ultimately to dense and strong interfaces should not be underestimated. Standard contents for superplasticizers, often referred to as high range water reducers (HRWR) are between 1 and 3% of weight of the cement. It should be noted that superplasticizers entrain some air and are slightly retarding, however, these effects are greatly reduced compared to conventional water reducers on the basis of salts of sulfonated lignin, hydroxy acids, or hydroxylated polymers. Since the water–reducing effect is only temporary, superplasticizers are usually added on the construction site.

Other important chemical admixtures are retarder, which is used to extend the fresh life of concrete and, perhaps more important, to improve the strength of HSC[17] and air–entraining admixture, which is used to improve the freeze–thaw resistance of concrete. It may be impossible to produce the desired air–entraining effect when using certain superplasticizers. However, a mixture of naphtalene sulfonate and conventional melamine sulfonate can be used produce concrete with the desired air-volume. [*Danielsen* (1987b)]

[17]This effect is due to the longer available time for the reactants to activate and dissolve before the hydration reaction takes place. Described closer in Section 6.2.2 on page 89.

2.7.2 Mix Proportioning

The mix proportions of high-strength concrete are generally derived from empirical tests. The properties of high–strength concrete are more dependent on the aggregate properties than they are for normal strength concrete. For NSC, empirical equations exist for mix proportions depending on specified strength and workability. These equations generally cannot be applied to HSC. In [*Addis et al.* (1990)], a procedure for the mix proportioning of trial mixed is proposed. However, the design of HSC will involve trial tests until reliable test data allow the development of design equations. In addition to the factors necessary to design normal strength concrete, the type and amount of superplasticizer and the type, shape, and roughness of the aggregate must also be included. With the use of superplasticizers, it is especially difficult to predict the workability of a mix. Suggested mix proportions for trial batches of concretes in five strength groups are shown in Figure 2-2. Some utilized mix proportions of high–strength concrete mixes are summarized in Figure 2-3.

2.8 Characteristics of High Strength Concrete

2.8.1 Elastic Behavior in Uniaxial Compression

Typical stress–strain curves for unreinforced concretes with different compressive strengths are shown in Figure 2-5. It should be noted that while the ascending branch becomes steeper and more linear with increasing compressive strength the total strain until failure increases only slightly, and the post–peak ability to transfer stresses at increasing strains decreases [*Carrasquillo et al.* (1981b), *Gerstle* (1979), *Shah* (1979)].

It should be noted that it is very difficult to obtain reliable post–peak curves for high–strength concrete because of the often explosive manner in which it fails. Even with extremely stiff testing machines, the so–called snap–back effect[18] can often only be recorded when using the crack mouth opening displacement (CMOD) of a pre–notched beam as feedback.

[18]Explained in Section 5.5

2.8.2 Young's Modulus and Poisson's Ratio

It has been shown that most design code equations for the Young's modulus of normal strength concretes overestimate this value when applied to high-strength concretes [*Ahmad et al.* (1987), *Brooks et al.* (1987)]. Extensive investigation of the elastic behavior of HSC has been carried out, and several, basically similar, equations to estimate the Young's modulus as a function of the compressive strength have been proposed. For example, for concretes with compressive strengths in the range of 40-90 MPa, following equations are applicable: $E_C = 9.1 f_{cube}^{1/3}$ [*Teychenné et al.* (1978)] and $E_C = 4.7 f_{cyl}^{1/2}$ [*209* (1978)], both using the compressive strength in MPa and giving the result in GPa. Another equation recommended by the ACI Committee 363 [*363* (1984)] is $E_C = 3.32 f_{cyl}^{1/2} + 6.9$. Shih et al. [*Shih et al.* (1989)] have suggested another equation: $E_C = 4.66 f_{cyl}^{1/2} - 1.37$. This equation is especially useful to estimate the Young's modulus of HSC incorporating silica fume.

Based on a least square analysis of high-strength mortars used in this study, the Young's modulus can be estimated for a range of compressive strengths of mortars from about 30 to 100 MPa with $E_M = 2.1 f_{cyl}^{1/2} + 16.4$, giving the Young's modulus in GPa for a compressive cylinder strength in MPa.[19] There is very little information on the Poisson's ratio for high-strength concrete. The Poisson's ratio is usually not constant but an increasing function of the axial strain. In [*Ahmad et al.* (1987)], an equation for the estimation of the Poisson's ratio is presented: $\nu = 1.55(f_c')^{-0.77}$, where f_c' is in 1000 psi (ksi).[20] The lateral strain in HSC is generally less than that of NSC, resulting in less external microcracking but also resulting in a smaller effect of confinement [*Ahmad et al.* (1987), *Bjerkeli et al.* (1990), *Thorenfeldt et al.* (1987)].

[19] The analysis is based on approximately 16 specimens of each of the first four of the mix proportions given in Table 6.2 and an additional 32 MPa mix. For 7-day mortar, the values are about 3 GPa lower. Because of the limited number of specimens tested, the above equation should be used with care.

[20] 1MPa=145 psi.

2.8.3 Tensile Splitting Strength and Modulus of Rupture

In HSC, the tensile strength is usually between 5 and 10% of the compressive strength. For concretes with compressive strength between 20 and 80 MPa, Carrasquillo et al. [*Carrasquillo et al.* (1981b)] proposed the following equation: $f'_{sp} = 0.59\sqrt{f'_c}$ (in MPa). Ahmad and Shah analysed available data via a mean curve: $f'_{sp} = 0.46(f'_c)^{0.55}$ (in MPa). The modulus of rupture is given by the respective researchers as: $f'_r = 0.94\sqrt{f'_c}$ and [21] $f'_r = 0.44(f'_c)^{2/3}$ (both equations in MPa). It should be noted that, although the tensile strength and modulus of rupture for HSC are higher than those of NSC, they do not increase proportionally with the compressive strength but rather with roughly its square root.

2.8.4 Shrinkage and Creep

Not much data is currently available regarding the long–term behavior of high–strength concrete. There is, however, a consensus about shrinkage and creep of HSC. Shrinkage of high–strength concretes with moderate water/binder ratios (0.25–0.4) is found to be less or equal to that of normal strength concrete, whereas shrinkage of HSC with low water/binder ratios (less than 0.25) is slightly less than shrinkage of NSC. The slight reduction in shrinkage can be attributed to less free water in the hardened concrete to evaporate. It is also found that the introduction of silica fume has little or no effect on the shrinkage behavior of concrete. However, the initial shrinkage rate of HSC is higher because of the higher rate of hydration [*Swamy* (1986)]. In other words, as the water/binder ratio decreases, the autogeneous shrinkage increases, thermal shrinkage depending on the cement content may occur superimposed on the autogeneous shrinkage, skin cracking due to drying is reduced, and the drying shrinkage decreases [*de Larrard* (1990)].

The maximum specific creep of HSC is less than that of NSC. Some researchers report that the creep deformations of HSC are 40 to 70 % of the creep deformations of NSC and the so–called CEB formula, which is used to predict creep deformation

[21] As compared to $f'_r = 0.62\sqrt{f'_c}$ for normal strength concrete.

[*Penttala et al.* (1987)]. However, since HSC is subjected to higher stresses, the total creep is about the same for both concretes [*Ngab et al.* (1985)]. Again, the initial creep rate was found to be higher in HSC [*Swamy* (1986)], which indicates a higher prestressing loss if prestressed at the same age. It is also reported that the desiccation creep is reduced and practically eliminated with silica fume contents of more than 7%, thus proving that there is no scale effect on creep [*de Larrard* (1990)]. It was shown that shrinkage and creep of silica fume concrete are hardly influenced by changes in humidity [*de Larrard* (1990)].

2.8.5 Ductility and Fracture Toughness

As already mentioned above, ductility decreases with increasing compressive strength. This decrease in ductility is the major reason for the slow introduction of HSC into construction industry. However, as is described below, heavier reinforcement can compensate this loss.

Ductility in pure tenson of plain concrete can conveniently be expressed as the ratio of the fracture energy[22] per unit area crack extension, which is a material property, over the maximum elastic strain energy per unit concrete volume.

$$l_{ch} = \frac{EG_f}{f_t^2} \tag{2.1}$$

where l_{ch} is a measure of the ductility, E is Young's modulus of the material, G_f is the fracture energy release rate, and f_t is the tensile strength of the material. This parameter has the unit of length and is called characteristic length. The smaller the characteristic length, the less ductile the behavior of the material. It was shown that the characteristic length decreases with increasing compressive strength [*Thorenfeldt et al.* (1990)].

There are several methods of obtaining reference values for the fracture energy G_F of concrete. Probably best known is the so–called RILEM method, which uses

[22]The fracture energy is equal to the area under the post–peak curve or the area between two load–displacement lines obtained from different crack lengths.

a three-point bending test set-up, but also the wedge-splitting test has been used successfully. Often, only the fracture toughness K_I is reported, which cannot account for non-linear effects. In linear elastic fracture mechanics (LEFM), there is a simple conversion from one to another: $G_F = K_I^2/E$. However, since non-linear fracture mechanics must generally be used to describe the behavior of concrete, an approach using R-curves instead is recommended. Such curves can account for the influence of different crack lengths on the toughness of a structure. Values for the fracture energy of concrete are, for example, 70.90 J/m^2, 92.90 J/m^2, and 90.76 J/m^2 for 20 MPa, 60 MPa, and 100 MPa, respectively[23] [*Kim et al.* (1992)]. It is noted that the fracture energy does not increase proportionally with increasing compressive strength.

The loss of ductility can be explained with considerations of the cracking scenarios in normal and high strength concretes. While for NSC bond cracking occurs at the aggregate-mortar interfaces at low relative stress levels, followed by the formation of crack bands in the mortar before failure, the strong interfaces in HSC result in delayed cracking, which occurs at higher relative stress levels almost simultaneously with the formation of mortar or aggregate cracks, thus dissipating less energy before failure and showing less deflection. The simultaneous occurrence of bond and mortar cracks in HSC is one of the major reasons for its explosive fracture behavior. In addition, cracks, which travel usually around aggregate particles in NSC, propagate through the the aggregate in HSC, indicating stronger interfaces. Although the fracture energy required to propagate a crack through an aggregate material is higher than for an interface, the crack length is reduced and less energy is consumed by crack formation a

s measured relative to the stored strain energy in the structure. Consequently, one may think of improving the ductility by providing interfaces just weak enough to still allow interface fracture or by introducing crack arrestors that spread the cracks which propagate through aggregates into crack bands. Another important concept is

[23]These values are reported to give an order of magnitude idea. They will vary significantly for different aggregates, mix prop
ortions, environmental conditions and test methods.

the use of steel fibers to bridge existing cracks, thus improving ductility. However, the fiber content needed to provide sufficient ductility is usually beyond what can be handled on the construction site in terms of workability and what is advisable in terms of cost.[24]

2.8.6 Effect of Confinement

Providing lateral reinforcement has become standard practice to ensure a ductile behavior of beams and columns under compression and bending. Early applications of HSC used it inside steel tubes to provide full confinement. It was shown that the required reinforcement in form of spirals, circular, and rectangular stirrups must be increased to obtain a ductile behavior in high–strength concrete structures [*Bjerkeli et al.* (1990)]. For example, a circular column made of C95 required 3.1% lateral reinforcement by volume to obtain ductile behavior, while 1.1% did prove insufficient [*Bjerkeli et al.* (1990)]. Figure 2-6 shows typical stress–strain curves for unreinforced and reinforced structures. Circular stirrups are much more effective than rectangular ones. It is generally possible to use HSC in virtually any situation, provided there is sufficient lateral reinforcement. One may ask, consequently, why we need to improve the ductility of unreinforced high–strength concrete. First, the abovementioned tests have been made on entire columns, in which significant stress redistributions take place before failure; the exact stress–strain curve of plain concrete under the influence of confinement is yet unknown but necessary to assess a structure's response to load and to develop design methods. Second, there is a danger that high lateral reinforcement ratios lead to costly and difficult to build structures. Figure 2-7 shows a typical interaction diagram for unreinforced and reinforced concrete, indicating a somewhat smaller relative moment bearing capacity of HSC column.[25]

[24]Such fiber contents would be of the order of 10 % and more by volume. However, 1 to 4% fibers can always be included to improve the post–peak behavior.

[25]This figure is based on a steel yield strain of $\epsilon_y = 2.5 \times 10^{-3}$, a reinforcement ratio $\rho = A_s f_y / A_c f_{cn}$, rectangular cross–section, and a CEB parabola–constant diagram for the concrete. It is taken from [*Thorenfeldt et al.* (1987)].

2.8.7 Freeze–Thaw Resistance

It is reported that the freeze–thaw resistance of HSC with intermediate water–binder ratios (0.25–0.4) is less than that of NSC, provided that both concretes incorporate air–entraining admixtures. However, with very low water–binder ratios (0.22 and less), very good freeze–thaw resistance was obtained even without air-entraining admixtures. This effect can be attributed to the smaller pore size and less available free water in the concrete. In Norway, 130 MPa concretes are used for paving without air-entrainment [*Danielsen* (1987b), *Helland* (1990)].

2.8.8 The Aggregate–Mortar Interface

Interfaces are actually interfacial regions, in which physical and chemical transitions takes place. The mortar–aggregate interfacial zone is about 50 μm in NSC and 25 μm in HSC incorporating silica fume [*Chatterji et al.* (1992)]. The aggregate–mortar interface in normal strength concrete is characterized by higher porosity due to bleeding, more and stronger spatially oriented calcium hydroxide crystals (CH), and lower strength compared to the bulk cement paste. Many researchers consider the interfacial zone in concrete the weak link [*Chatterji et al.* (1992), *Mehta et al.* (1990)]. With the introduction of silica fume and low water–binder ratios, the interfacial zone is densified, the size and amount of CH–crystals is reduced, and the hydration products generally have smaller sizes, resulting in higher strength compared to the interfacial zones of normal strength concrete. These changes are the major reasons for the improved performance of HSC compared to NSC [*Nilsen et al.* (1992), *Diamond et al.* (1992), *Mitsui et al.* (1992)].

It should be noted that the nature of the interface is a function of mortar and aggregate material. With carbonate rocks, for example, chemical interactions have been observed [*Monteiro et al.* (1986)]. The roughness of the aggregate plays an important role for the mechanical interlocking at the interface, which is studied in this work. The physical interaction itself (adhesion) is a function of the total contact area, hence of porosity and roughness.

2.9 Cracks and Cracking Scenarios in Concrete

Concrete structures are full of cracks. Among the earliest cracks to occur are interfacial cracks due to differences in the thermal properties of aggregate and mortar. These cracks are often "repaired" by an effect called autogeneous healing, the filling of widened interfacial zones with hydration products.

It is evident that the larger the aggregate the higher the strain and the wider the "gap" between aggregate and mortar. Some researchers attribute the decreasing compressive strength at increasing MSA only to a size effect [*Bažant* (1992)]. It must be kept in mind that there are physical and chemical reasons as well. So it is not only the smaller maximum aggregate size that leads to higher strengths in HSC because of smaller strains due to differences in the thermal properties of aggregate and cement paste, but also the delayed pozzolanic action of the silica fume that can better compensate for the widening of interfacial cracks by means of autogeneous healing of such disturbed zones.

Another family of cracks are shrinkage cracks, which are caused by water loss of the mortar. Since shrinkage cracks occur at later stages of hydration, they are healed to a lesser degree than thermal cracks [*Chatterji et al.* (1992)]. Shrinkage cracks occur in the mortar and at the interfaces, often acting as starter cracks. As mentioned above, bond cracks in HSC occur at higher relative stresses, and the mortar cracks which eventually link the bond cracks at complete failure form almost simultaneously, resulting in brittle or explosive fracture.

Material	**Procedure**	f'_c [MPa]	f_t [MPa]
Reference Materials:			
Concrete	Standard, cured at room temperature	30-50	7
Alumina	Sintered above 1300°C	3000-4000	300-400
Systems based on cementitious materials:			
Silica-fume cement	Cured at room temperature	100	12
DSP* cement	Cured at room temperature with superplasticizers added, w/c=0.12-0.22	140-270	$0.1f'_c$
Warm pressed cement	Pressed at 345 MPa at 250° for 1 h Pressed at 345 Mpa at 150° for1 h	650 410	68 43
MDF† cement	Calcium aluminate cement with Dow polymer, press set hydrated and dried at 80°	300	150
Comtek CBC tooling material	Calcium silicate with steel aggregate cured at 150°	500	70
* Densified Systems with fine Particles † Macro Defect Free cement			

(From reference [*Leung* (1993)].)

Table 2.1: Properties of some cement based ceramics (CBC) compared with concrete and alumina.

Classification	Chemical and mineralogical composition	Particle characteristics
Cementitious and pozzolanic		
Granulated blast-furnace slag (cementitious)	Mostly silicate glass containing mainly calcium, magnesium, aluminum, and silica. Crystalline compounds of melilite group may be present in small quantity.	Unprocessed material is of sand size and contains 10–15% moisture. Before use it is dried and ground to particles less than 45 μm (usually about 500 m^2/kg Blaine). Particles have rough texture.
High-calcium fly ash (cementitious and pozzolanic)	Mostly silicate glass containing mainly calcium, magnesium, aluminum, and alkalies. The small quantity of crystalline matter present generally consists of quartz and C_3A; free lime and periclase may be present; $C\bar{S}$ and $C_4A_3\bar{S}$ may be present in the case of high-sulfur coals. Unburnt carbon is usually less than 2%.	Powder corresponding to 10–15% particles larger than 45 μm (usually 300–400 m^2/kg Blaine). Most particles are solid spheres less than 20 μm in diameter. Particle surface is generally smooth but not as clean as in low-calcium fly ashes.
Highly active pozzolans		
Condensed silica fume	Consists essentially of pure silica in noncrystalline form.	Extremely fine powder consisting of solid spheres of 0.1 μm average diameter (about 20 m^2/g surface area by nitrogen adsorption).
Rice husk ash (Mehta–Pitt process)	Consists essentially of pure silica in noncrystalline form.	Particles are generally less than 45 μm but they are highly cellular (about 60 m^2/g surface area by nitrogen adsorption).
Normal pozzolans		
Low-calcium fly ash	Mostly silicate glass containing aluminum, iron, and alkalies. The small quantity of crystalline matter present generally consists of quartz, mullite, sillimanite, hematite, and magnetite.	Powder corresponding to 15–30% particles larger than 45 μm (usually 200–300 m^2/kg Blaine). Most particles are solid spheres with average diameter 20 μm. Cenospheres and plerospheres may be present.
Natural materials	Besides aluminosilicate glass, natural pozzolans contain quartz, feldspar, and mica.	Particles are ground to mostly under 45 μm and have rough texture.
Weak pozzolans		
Slowly cooled blast-furnace slag, bottom ash, boiler slag, field burnt rice husk ash	Consists essentially of crystalline silicate materials, and only a small amount of noncrystalline matter.	The materials must be pulverized to very fine particle size in order to develop some pozzolanic activity. Ground particles are rough in texture.

(From reference [*Mehta* (1986)].)

Figure 2-1: Classification, composition, and particle characteristics of mineral admixtures for concrete

Strength Grade	Avg. Strength MPa	Option	Cementitious Materials			Total* Water	Coarse Agg.	Fine Agg.	Total Batch	W/C
			PC	FA or BFS	CSF					
A	65	1	534	--	--	160	1050	690	2434	0.30
		2	400	106	--	160	1050	690	2406	0.32
		3	400	64	36	160	1050	690	2400	0.32
B	75	1	565	--	--	150	1070	670	2455	0.27
		2	423	113	--	150	1070	670	2426	0.28
		3	423	68	38	150	1070	670	2419	0.28
C	90	1	597	--	--	140	1090	650	2477	0.23
		2	447	119	--	140	1090	650	2446	0.25
		3	447	71	40	140	1090	650	2438	0.25
D	105	--	--	--	--	--	--	--	--	--
		2	471	125	--	130	1110	630	2466	0.22
		3	471	75	42	130	1110	630	2458	0.22
E	120	--	--	--	--	--	--	--	--	--
		2	495	131	--	120	1120	620	2486	0.19
		3	495	79	44	120	1120	620	2478	0.19

+The mix proportions are for non-air-entrained concrete, although 2% entrapped air is assumed.
*Total water includes the water in the superplasticizing admixture, the dosage of which may range from 10 to 20L/m^3, depending on consistency and strength requirements.

(From reference [*Mehta et al.* (1990)].)

Figure 2-2: Suggested mix proportions for first trial batches in five strength groups, in kg/m^3

No.	Description of concrete	Avg. 28-d Compressive strength, MPa	Component Materials in 1 m³ Concrete Batch kg/m³							L/m³	Water to cementitious ratio by weight	Ref. No.
			Cementitious material				total water	fine aggregate	coarse aggregate	super-plasticizer		
			PC	FA	BFS	CSF						
1	Water Tower Place, Chicago	65	500	60	-	-	178	608	1068	*	0.32	10
2	Commerce Tower, Houston	65	390	100	-	-	161	575	1141	*	0.33	11
3	Inter First Plaza, Dallas	80	360	150	-	-	148	603	1157	3*	0.29	12
4	Nova Scotia Plaza, Toronto	82	315	-	135	36	145	745	1130	6	0.30	13
5	Experimental Column, Montreal	90	500	-	-	30	135	700	1100	15	0.25	16
6	Laboratory Mixture	70	485	-	-	-	130	762	1143	3.4	0.27	15
7	Laboratory Mixture	72	317	-	167	-	133	749	1145	7.0	0.28	15
8	Laboratory Mixture	80	315	-	155	35	143	744	1142	7.5	0.29	15
9	Laboratory Mixture	82	449	-	-	39	130	758	1149	11.0	0.27	15
10	Laboratory Mixture	91	427	-	-	59	132	754	1139	14.9	0.27	15
11	Laboratory Mixture	93	450	-	-	50	140	687	1108	17	0.28	14
12	Laboratory Mixture	97	500	-	-	42	138	675	1130	10	0.25	6
13	Laboratory Mixture	100	486	-	-	54	135	661	1112	20	0.25	14
14	Laboratory Mixture	103	580	-	-	70	140	620	1025	12	0.22	8
15	Laboratory Mixture	107	517	-	-	58	126	641	1126	25	0.22	14
16	Two Union Square, Seattle	120	564	-	-	44	124	682	1100	21	0.20	+

*Concrete Nos. 1 and 2 contained only a normal water-reducing admixture; Concrete No. 3 also contained a normal water-reducing admixture in addition to a superplasticizer.
+Personal communication, Professor Weston Hester, University of California at Berkeley.

(From reference [*Mehta et al.* (1990)].)

Figure 2-3: Mix proportions for selected high-strength concrete mixtures

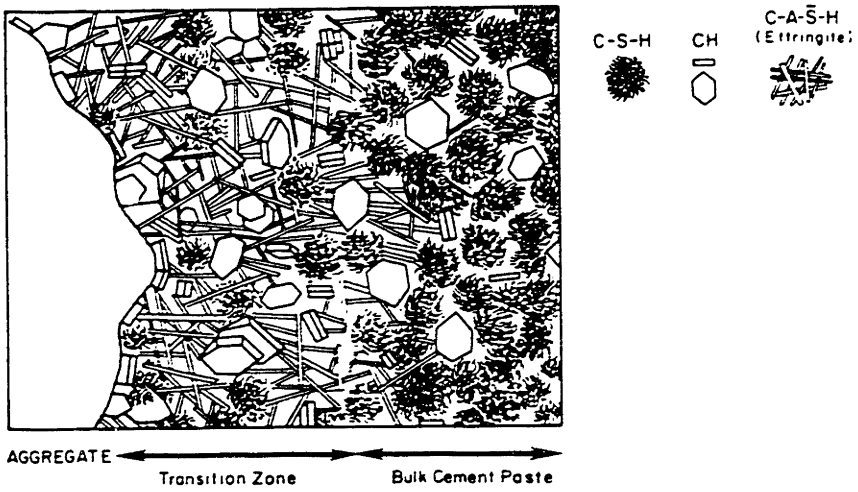

(From reference [*Mehta* (1986)].)

Figure 2-4: Simplified representation of the transition zone and the bulk cement paste adjacent to an aggregate particle

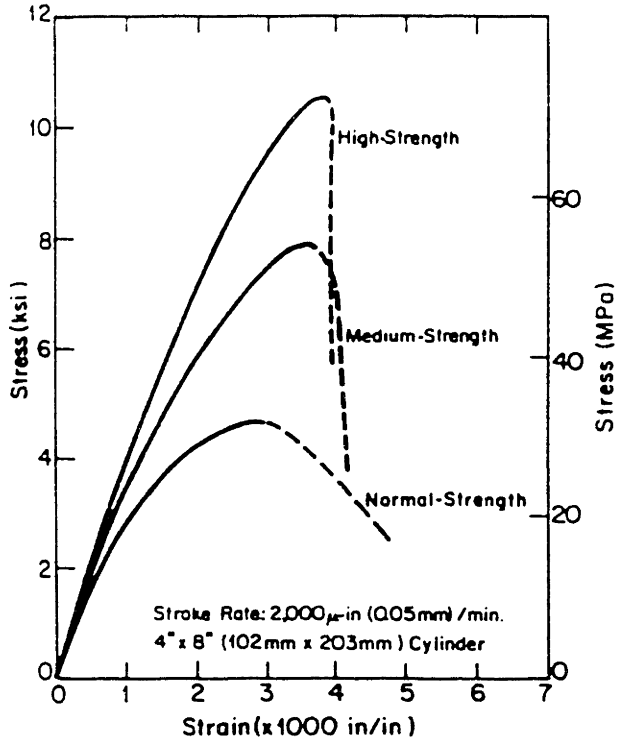

(From reference [*Carrasquillo et al.* (1981b)].)

Figure 2-5: Uniaxial compressive stress–strain curves for concretes of different strength levels

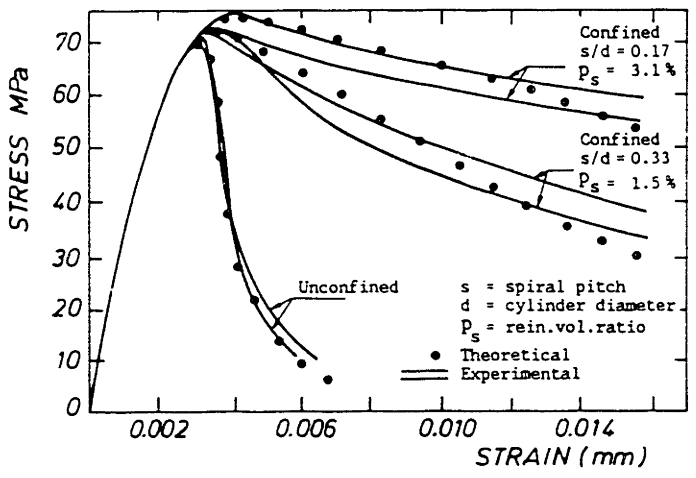

(From reference [*Holand* (1987)].)

Figure 2-6: The influence of spiral reinforcement on the ductility of high–strength concrete

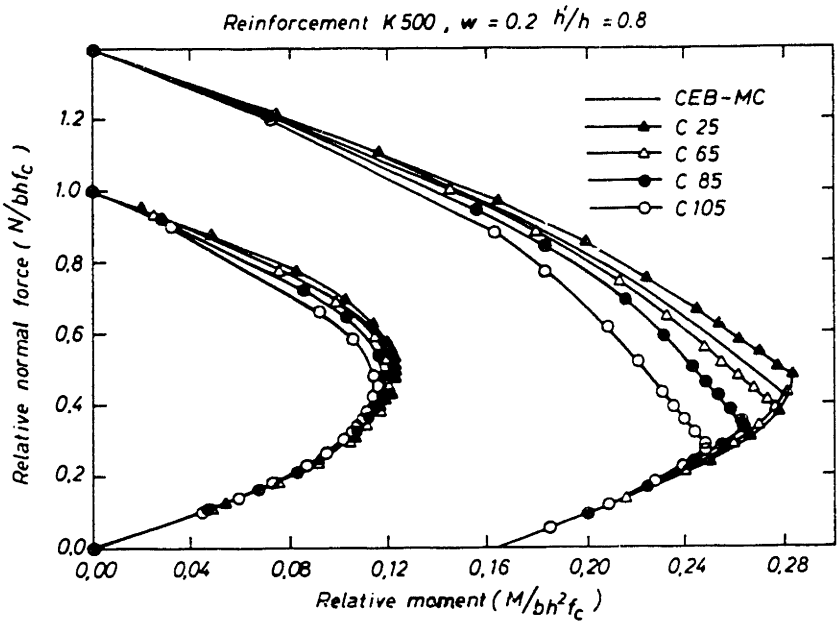

(From reference [*Thorenfeldt et al.* (1987)].)

Figure 2-7: Interaction diagrams for high–strength concrete columns with rectangular cross–sections

Chapter 3

Interface Fracture Mechanics

The objectives of interface fracture mechanics are twofold, first, to seek a useful definition of interfacial toughness and second, to assess this parameter for bimaterial systems. Interface fracture toughness is a material property that characterizes the resistance of a bimaterial interface to fracture. This chapter reviews the fundamental concepts of interface fracture mechanics as applied to mortar–aggregate interfaces. It is based on the recent works of Hutchinson and his co–workers [*Rice* (1988), *Suo* (1989), *Evans et al.* (1989), *Hutchinson* (1990), *Hutchinson et al.* (1992)]. This review is an altered version of a chapter in K. M. Lee's Ph.D. thesis [*Lee* (1993)].

3.1 Bimaterial Elasticity

A composite of two homogeneous materials with continuity of traction and displacement is called a bimaterial. In the following, only isotropic bimaterials under plane strain conditions will be discussed. Figure 3-1 shows the conventions for an interface crack consisting of material 1 and material 2 with the interface along the x_1–axis. E_1, μ_1, and ν_1 are the Young's modulus, the shear modulus and the Poisson's ratio of material 1, whereas E_2, μ_2, and ν_2 are these quantities of material 2. We define material 1 as lying above the interface.

Dundurs [*Dundurs* (1969)] observed that a wide range of plane problems of bimaterial elasticity depends only on two non–dimensional factors that are combinations

of the elastic moduli. Those factors, further called Dundurs' parameters α and β, are defined as follows:

$$\alpha = \frac{\bar{E}_1 - \bar{E}_2}{\bar{E}_1 + \bar{E}_2}, \qquad \beta = \frac{1}{2}\frac{\mu_1(1-2\nu_2) - \mu_2(1-2\nu_1)}{\mu_1(1-2\nu_2) + \mu_2(1-2\nu_1)} \tag{3.1}$$

where $\bar{E} = E/(1-\nu^2) = 2\mu/(1-\nu)$. The parameter α describes the relative stiffness of the two materials. When material 1 is much stiffer than material 2, α approaches +1. Conversely, α converges to -1 when material 1 is extremely compliant. The parameter β vanishes only in plane strain and when the two materials are incompressible (that is if $\nu_1 = \nu_2 = 1/2$, for example rubber). Both α and β vanish when there is no dissimilarity of the elastic properties. Values for Dundurs' parameters for certain material combinations are shown in Figure 3-2.

3.1.1 Crack Tip Fields

Consider a semi–infinite, traction–free crack lying along the interface between two homogeneous isotropic half–planes, with material 1 above and material 2 below the interface, as in Figure 3-1. Note that there are two coordinate systems and that no specific length or load is present in this problem [*Suo* (1989)].

Solutions to this problem were presented first by England, Erdogan, and Rice and Sih in 1965 [*England* (1965), *Erdogan* (1965), *Rice et al.* (1965)]. Williams discovered the oscillatory near–tip behavior of an interface crack in 1959 [*Williams* (1959)]. In this thesis I use the notations of Rice [*Rice* (1988)]. They have the advantage of reducing to the conventional notation when the elastic moduli mismatch vanishes.

For plane problems, the normal and shear stresses of the singular field acting on the interface at a distance r ahead of the crack tip are given by

$$\sigma_{22} + i\sigma_{12} = \frac{K}{\sqrt{2\pi r}} r^{i\epsilon} \tag{3.2}$$

or

$$\sigma_{22} = Re[Kr^{i\epsilon}](2\pi r)^{-1/2}, \qquad \sigma_{12} = Im[Kr^{i\epsilon}](2\pi r)^{-1/2} \tag{3.3}$$

where $K = K_1 + iK_2$ is the complex stress intensity factor, $i \equiv \sqrt{-1}$, and ϵ is the oscillation index, given as a function of β:

$$\epsilon = \frac{1}{2\pi} ln \left(\frac{1-\beta}{1+\beta} \right) \tag{3.4}$$

This parameter brings in some complications that are not present in the elastic fracture mechanics of homogeneous solids. Note that K_1 and K_2 do not strictly measure the normal and shear stress singularities on the interface ahead of the crack tip because of the term $r^{i\epsilon}$ in Eqn. 3.2.

The associated crack face displacements at a distance r behind the crack tip, $\delta_i = u_i(r, \theta = \pi) - u_i(r, \theta = -\pi)$, are given by

$$\delta_2 + i\delta_1 = \frac{8K}{E(1+2i\epsilon)\cosh(\pi\epsilon)} \left(\sqrt{\frac{r}{2\pi}} \right) r^{i\epsilon} \tag{3.5}$$

For convenience, let us define an average stiffness E^* as

$$\frac{1}{E^*} = \frac{1}{2} \left(\frac{1}{\bar{E}_1} + \frac{1}{\bar{E}_2} \right) \tag{3.6}$$

The energy release rate per unit area crack extension [*Malyshev et al.* (1965)] then follows as

$$G = \frac{1}{E^* \cosh^2(\pi\epsilon)} |K|^2 \tag{3.7}$$

where $|K|^2 = K_1^2 + K_2^2$ and $\cosh^2(\pi\epsilon) = 1/(1-\beta^2)$. From Eqn. 3.3, the phase angle $\hat{\psi}$, a measure of the contribution of shear vs. opening mode, is defined as

$$\hat{\psi} = \tan^{-1} \left(\frac{Im(K\hat{L}^{i\epsilon})}{Re(K\hat{L}^{i\epsilon})} \right) \tag{3.8}$$

where $\hat{L}$ is a reference length. The measure of the proportion of mode 2 to mode 1 in the vicinity of a crack tip requires the specification of a length quantity, since the ratio of the shear traction to normal traction varies slowly with the distance to the tip when $\beta \neq 0$. Note that $\hat{\psi}$ is always non–zero due to the elastic moduli mismatch

across the interface even under pure Mode I loading conditions, that is when geometry and loading are symmetric with respect to the crack plane.

The reference length $\hat{L}$ can be chosen rather freely. For example, one can chose a distance based on an inplane length of the specimen geometry, such as crack length, or one that is based on the material length scale, such as the size of the fracture process zone. The former is useful for discussing the mixed mode character of a bimaterial crack solution, independent of material fracture behavior, while the latter is advantageous in interpreting mixed mode fracture data. For solutions to common interface fracture problems, see for example [*Suo et al.* (1990)].

3.2 Interfacial Fracture Toughness

The fracture mode of an interface of dissimilar materials is usually mixed. The differences in the elastic moduli disrupt the symmetry even when the geometry and the loading are symmetric with respect to the crack plane. Furthermore, an interface is typically more brittle compared to the bulk materials themselves. An interface crack also has a high tendency to propagate along the plane of the interface even with a large portion of shear stresses present.

For any interfacial crack problem, the complex K will have the form

$$KL^{i\epsilon} = YT\sqrt{L}e^{i\psi} \tag{3.9}$$

where T is the applied traction loading, L is a length describing the geometry, such as crack length or uncracked ligament length, Y is a dimensionless real positive number, and $\hat{\psi}$ is the phase angle of the quantity $KL^{i\epsilon}$, but is often called the phase angle of the stress intensity factor or the loading phase angle. Both Y and $\hat{\psi}$ generally depend on the ratios of various applied loads and lengths and, for a traction–prescribed problem, on α and β. The magnitude, $|KL^{i\epsilon}| = |K|$, is given by $YT\sqrt{L}$.

From the peak value of T at the onset of crack propagation, the critical interface toughness $|K|_c$ can be calculated according to Eqn. 3.9.

It is clear that this value is also a function of the phase angle. Hence, a fracture toughness curve (K vs. $\hat{\psi}$) is needed to fully characterize the toughness of an interface. Generally, the toughness increases with increasing phase angle. However, it is current practice to report the (G_c vs. $\hat{\psi}$)–curve instead. $|K|$ is related to G_c by Eqn. 3.7.

Together with the toughness curve, the used characteristic length $\hat{L}$ must be reported. The freedom in the choice of $\hat{L}$ in the definition of $\hat{\psi}$ is a consequence of a simple transformation rule from one choice to another. Let ψ_1 be associated with L_1 and ψ_2 be associated with L_2. From the definition in Eqn. 3.8 one can show that

$$\psi_2 = \psi_1 + \epsilon \ln\left(\frac{L_2}{L_1}\right) \tag{3.10}$$

Therefore, toughness data can be transformed easily [*Rice* (1988)].

Let $\hat{L}$ denote a length characterizing the size of the fracture process zone or the typical size of the plastic zone at fracture, and let $\hat{\psi}$ be associated through Eqn. 3.8. Since small scale yielding or a small scale fracture process zone is assumed, $\hat{L}$ necessarily lies within the zone of dominance of the K–field. Given the choice of $\hat{L}$, the criterion for interface fracture can be stated as

$$G = \Gamma_i(\hat{\psi}, \hat{L}) \tag{3.11}$$

where the implicit dependence of the toughness function on $\hat{L}$ has been noted. In other words, $\Gamma_i(\hat{\psi}, \hat{L})$ is the critical value of the energy release rate needed to advance the crack in the interface in the presence of a combination of tractions whose relative proportion is given by $\hat{\psi}$. Using Eqn. 3.10, a change in the choice of the length L in the definition of $\hat{\psi}$ to another involves only a shift of the $\hat{\psi}$–origin of Γ_i, according to

$$\Gamma_i(\psi_2, L_2) = \Gamma_i(\psi_1 + \epsilon \ln\left(\frac{L_2}{L_1}\right), L_1) \tag{3.12}$$

When ϵ is small, the shift will generally be negligible even for changes in $\hat{L}$ of several orders of magnitude.

3.3 Interface Toughness with $\beta = 0$

The results presented in the previous section become much simpler for conditions that satisfy $\beta = 0$, see Eqn. 3.1. When $\beta = 0$ and thus $\epsilon = 0$, Eqn. 3.2 becomes

$$\sigma_{22} + i\sigma_{12} = \frac{(K_1 + iK_2)}{\sqrt{2\pi r}} \tag{3.13}$$

and Eqn. 3.5 reduces to

$$\delta_2 + i\delta_1 = \frac{8(K_1 + iK_2)}{E^*} \left(\sqrt{\frac{r}{2\pi}}\right) \tag{3.14}$$

Here, the interface stress intensity factors K_1 and K_2 are analogous to their counterparts in linear elastic fracture mechanics for homogeneous, isotropic solids. Because of the difficulties in decoupling the normal and shear components for $\beta \neq 0$ and the fact that for most mortar/aggregate interfaces β is close to zero anyway, it is convenient to set $\beta = 0$. Now with $\epsilon = 0$ the phase angle is given by

$$\psi = \tan^{-1}\left(\frac{K_2}{K_1}\right) \tag{3.15}$$

With $\epsilon = 0$, ψ is indeed the phase angle. Here, $\psi = 0°$ corresponds to pure Mode I and $\psi = 90°$ to pure Mode II.

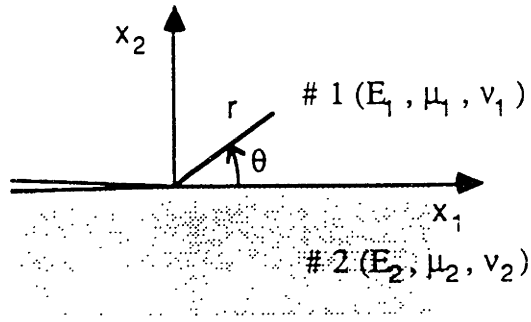

Figure 3-1: Geometry and conventions for an interface crack

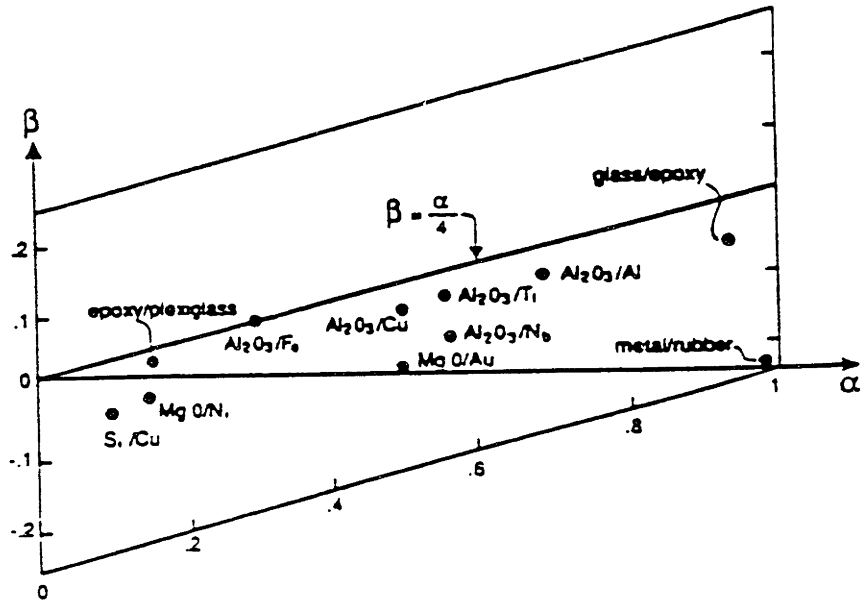

Figure 3-2: Values of Dundurs' parameters for bimaterials

Chapter 4

The Sandwiched Test Specimen

Although there is a variety of test methods available to obtain fracture data from concrete, mortars, and rocks, there is no established test for interface fracture parameters. The Brazilian disk specimen was used for ceramic–metal interfaces by Hutchinson [*Hutchinson* (1990)] and for mortar–aggregate interfaces by Kwang-Myong Lee [*Lee* (1993)] with success. However, Bažant concludes that Brazilian disk specimens cannot be used to investigate the size scale effect because of a sudden change in the failure mode with increasing specimen size [*Bažant* (1992)]. For this study, I chose to use a Sandwiched Beam test specimen. It consists of a thin layer of material 2 sandwiched between two blocks of material 1 (Fig. 4-1). Each material is considered isotropic and linearly elastic. The crack lies along the interface and the x_1–axis, with the tip at the origin.

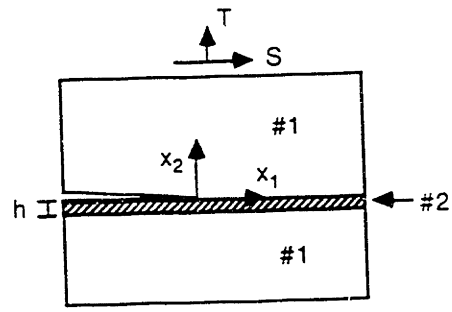

Figure 4-1: Interface crack problem in a sandwiched specimen

4.1 Universal Relation for Sandwiched Beams

A universal relation between the interface stress intensity factors, K_1 and K_2, and the stress intensity factors, K_I and K_{II}, can be formulated when the thickness of the aggregate layer h is small compared to the crack length a [*Suo et al.* (1989)]. For a homogeneous specimen, the far field for the problem in Fig. 4-1 is characterized by the Mode I and Mode II stress intensity factors, K_I and K_{II}. The traction at a distance r ahead of the crack tip is given by

$$\sigma_{22} + i\sigma_{12} = \frac{K^\infty}{\sqrt{2\pi r}} \tag{4.1}$$

where $K^\infty = K_I + iK_{II}$. The energy release rate is

$$G = \frac{1}{\bar{E}_1}(K_I^2 + K_{II}^2) \tag{4.2}$$

with $\bar{E}_1 = E_1/(1-\nu_1^2)$. It appears from energy arguments that Eqn. 3.7 and Eqn. 4.2 must be equal, therefore

$$|Kh^{i\epsilon}| = p|K^\infty| \tag{4.3}$$

with $p = \sqrt{\frac{1-\alpha}{1-\beta^2}}$ and $|Kh^{i\epsilon}| = |K|$. From that we obtain the universal relation between the interface stress intensities and the applied stress intensities as

$$Kh^{i\epsilon} = pK^\infty e^{i\omega(\alpha,\beta)} \tag{4.4}$$

or,

$$K_1 + iK_2 = p(K_I + iK_{II})h^{-i\epsilon}e^{i\omega(\alpha,\beta)} \tag{4.5}$$

in which $\omega(\alpha,\beta)$ is a real function. This function was extracted from the numerical solution to the integral equation and is given in Table 4.1 (from [*Suo et al.* (1989)]). The parameter ω can be regarded as the shift in phase of the interface intensity factors with respect to the applied intensity factors and is a non–dimensional function of Dundurs' parameters α and β. We also define

ω–Values from Dundurs' Parameters									
β	α								
	-0.8	-0.6	-0.4	-0.2	0.0	0.2	0.4	0.6	0.8
-0.4	2.2	3.5							
-0.3	3.0	4.0	3.3	1.4					
-0.2	3.6	4.1	3.4	2.0	-0.3	-3.3			
-0.1	4.0	4.1	3.3	2.0	0.1	-2.3	-5.5	-10.8	
0.0	4.4	3.8	2.9	1.6	0.0	-2.1	-4.7	-8.4	-14.3
0.1			2.3	1.1	-0.5	-2.3	-4.5	-7.4	-11.6
0.2					-1.3	-3.0	-4.9	-7.3	-10.5
0.3							-5.8	-7.8	-10.4
0.4									-11.1

Table 4.1: ω–Values as a function of Dundurs' parameters α and β (from [*Suo et al.* (1989)].

$$\begin{aligned} Kh^{i\epsilon} &= |K|e^{i\psi^*} \\ K^{\infty} &= |K^{\infty}|e^{i\phi} \end{aligned} \tag{4.6}$$

where $\psi^* = \tan^{-1}[Im(Kh^{i\epsilon})/(Re(Kh^{i\epsilon})]$ is the phase angle and $\phi = \tan^{-1}(K_{II}/K_I)$. This yields Eqn. 4.4 as

$$\psi^* = \phi + \omega \tag{4.7}$$

where $\omega = \omega(\alpha, \beta)$. If one sets $L_1 = h$ and $L_2 = \hat{L}$ in Eqn. 3.10 and substitutes Eqn. 4.7 into Eqn. 3.10, the loading phase angle is obtained as:

$$\hat{\psi} = \psi^* + \epsilon \ln(\frac{\hat{L}}{h}) = \phi + \omega + \epsilon \ln(\frac{\hat{L}}{h}) \tag{4.8}$$

With a choice of $\hat{L}$ as a fixed length, one can calculate the loading phase angle $\hat{\psi}$ from Eqn. 4.8. The actual stress intensity factors, K_1 and K_2, can be calculated from the applied, or apparent, stress intensity factors, K_I and K_{II}, using the universal relationship given in Eqn. 4.5. Since β is usually very small compared to α and the

dependence of ω on β is very weak, one can set $\beta = 0$. This yields Eqn. 4.5 as

$$K_1 + iK_2 = \sqrt{1-\alpha}(K_I + iK_{II})e^{i\omega(\alpha,0)} \tag{4.9}$$

in which ω is a function of α only.

4.2 Four–Point Bending Specimen for Testing in Mode I

The application of the universal relation to a particular test specimen is straightforward. For Mode I testing, the four–point bending test specimen has already proven successful [*Lee* (1993)].

The apparent stress intensity factor K_I for the specimen in Fig. 4-2 can be obtained from either a finite element analysis [1] or for general geometries from handbooks such as the *Stress Analysis of Cracks Handbook* [*Tada et al.* (1985)] as

$$K_I = f_1 \sigma_r \sqrt{\pi a} \tag{4.10}$$

where

$$\sigma_r = \frac{6M}{bd^2} \tag{4.11}$$

in which M is the applied moment, a the crack length, b the width, and d the height of the specimen (see Fig. 4.2). The correction factor f_1 for four-point pure bending is

$$f_1 = 1.122 - 1.4\left(\frac{a}{d}\right) + 7.33\left(\frac{a}{d}\right)^2 - 13.08\left(\frac{a}{d}\right)^3 + 14.0\left(\frac{a}{d}\right)^4 \tag{4.12}$$

in which $\left(\frac{a}{d}\right)$ is called the relative crack length. The interface stress intensity factors K_1 and K_2 are obtained from substituting Eqn. 4.10 into Eqn. 4.5. With $\beta = 0$, we have

[1] for example utilizing virtual crack extension method and non–local elements

$$\begin{aligned} K_1 &= \sqrt{1-\alpha}(f_1\sigma\cos\omega)\sqrt{\pi a} \\ K_2 &= \sqrt{1-\alpha}(f_1\sigma\sin\omega)\sqrt{\pi a} \end{aligned} \tag{4.13}$$

From Eqn. 4.2 the energy release rate can be calculated as

$$G = \frac{K_I^2}{\bar{E}_1} = \frac{f_1^2\sigma_r^2\pi a}{\bar{E}_1} \tag{4.14}$$

Since for Mode I $\phi = 0$, the phase angle from Eqn. 4.8 is

$$\hat{\psi} = \omega + \epsilon \ln\left(\frac{\hat{L}}{h}\right) \tag{4.15}$$

Note that the specimen will not be in pure Mode I condition. However, the shift in the range of 0 to 5 degrees is very small so the specimen can be considered to be essentially in Mode I.

4.3 Specimens for Mixed Mode Testing

The mixed mode four–point bending specimens is shown in Fig. 4-3. An alternative three–point mixed mode bending specimen is shown in Figure 4-4. These specimens have not been used for mortar–aggregate interfaces before. There are reports on their use for soda–lime glass and PMMA [*He et al.* (1989)] and for stainless steel [*Hua et al.* (1982)].

The apparent stress intensities are

$$\begin{aligned} K_I &= \frac{M}{bd^{3/2}} f_b\left(\frac{a}{d}\right) \\ K_{II} &= \frac{Q}{bd^{1/2}} f_s\left(\frac{a}{d}\right) \end{aligned} \tag{4.16}$$

where $f_b\left(\frac{a}{d}\right)$ and $f_s\left(\frac{a}{d}\right)$ are given in Table 4.2. Again, b is the specimen thickness, d is the specimen height, M and Q are the applied moment and shear force, respectively.

The interface stress intensity factors can be obtained from Eqn. 4.5 with the

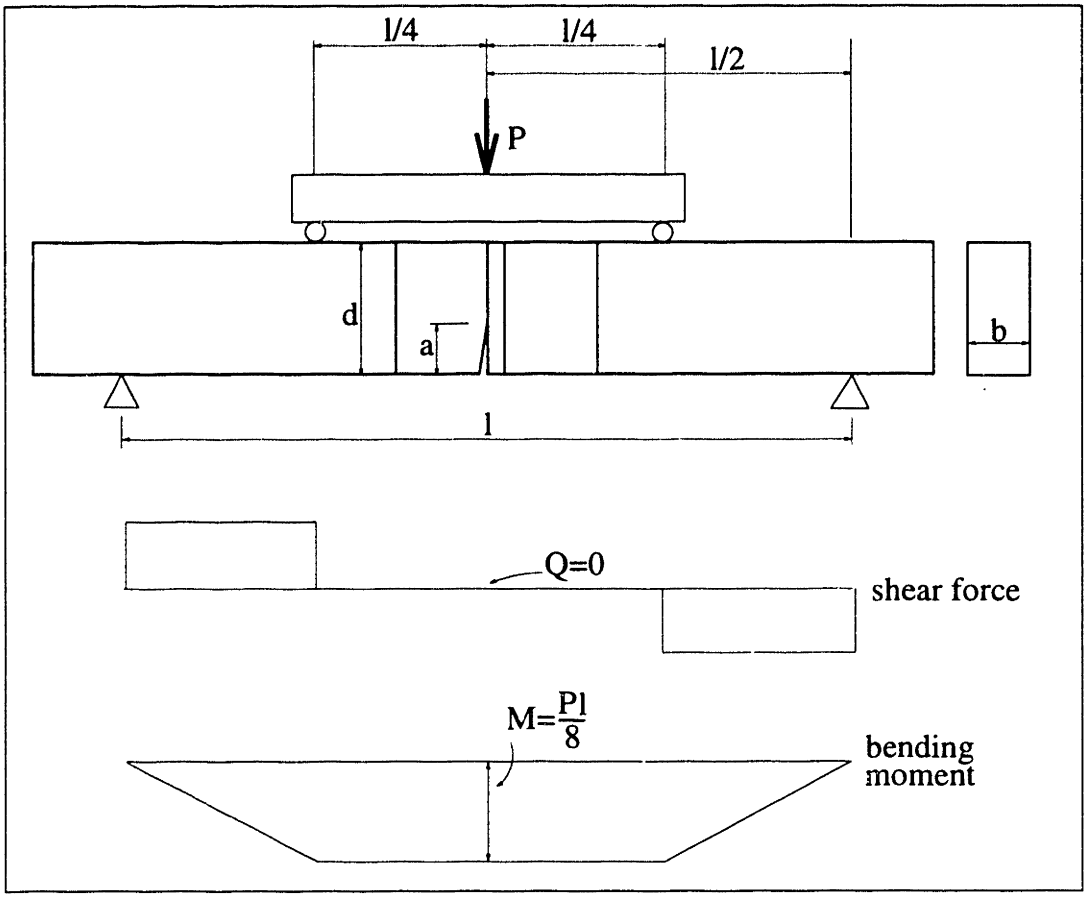

Figure 4-2: Four–point Mode I test specimen

$\left(\frac{a}{d}\right)$	$f_b\left(\frac{a}{d}\right)$	$f_s\left(\frac{a}{d}\right)$
0.20	4.97	0.496
0.25	5.67	0.667
0.30	6.45	0.857
0.35	7.32	1.080
0.40	8.35	1.317
0.50	9.60	1.557
0.55	11.12	1.838
0.60	15.06	2.441
0.65	19.17	2.794

Table 4.2: Stress intensity coefficients

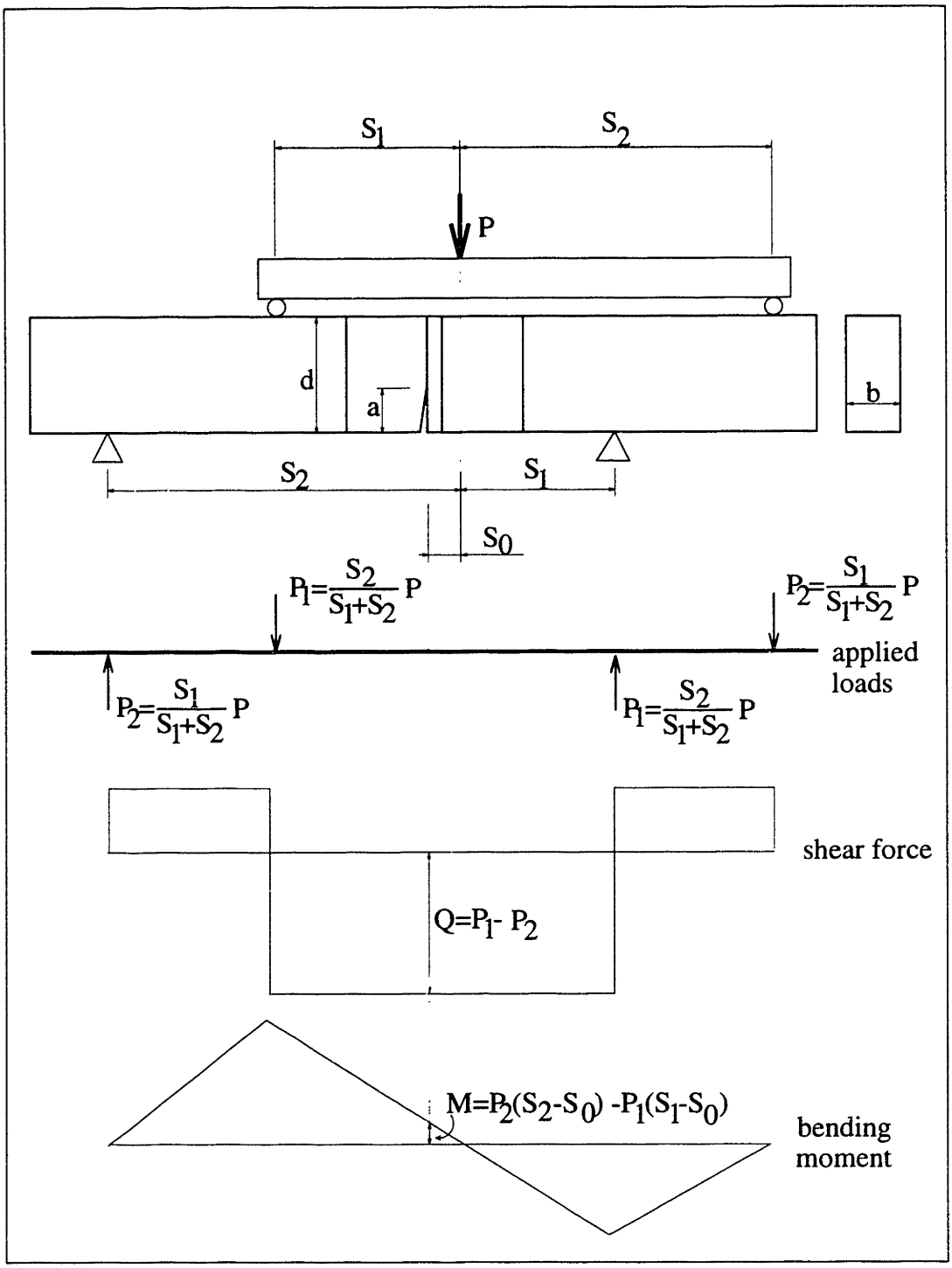

Figure 4-3: Four–point mixed mode bending specimen

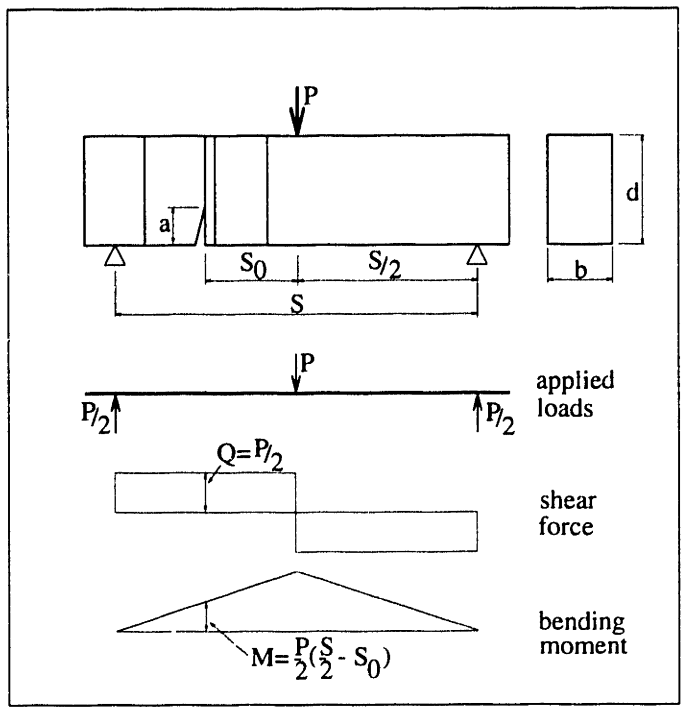

Figure 4-4: Three–point mixed mode bending specimen

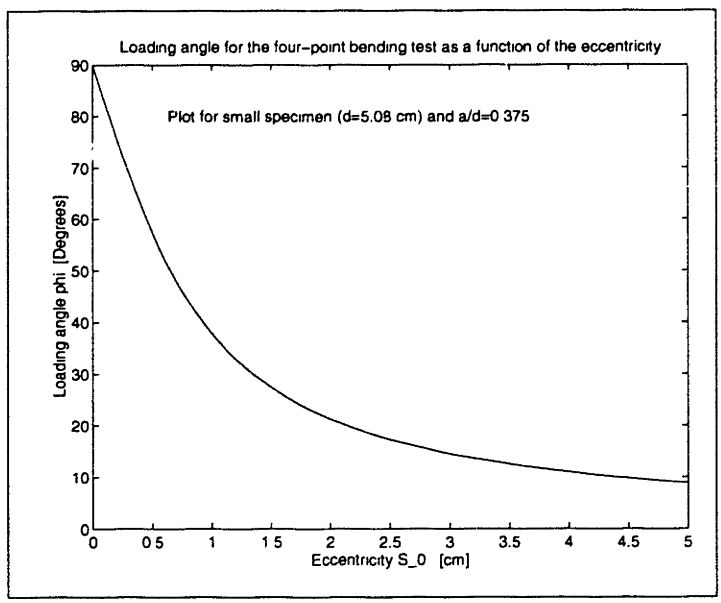

$$\phi = \tan^{-1}\left(\frac{f_s d}{f_b S_0}\right)$$

$(f_s = 1.1985,\ f_b = 7.835,\ d = 5.08\text{cm})$

Figure 4-5: Loading angle as a function of S_0

condition $\beta = 0$ as

$$\begin{aligned} K_1 &= \sqrt{1-\alpha}(K_I \cos\omega - K_{II} \sin\omega) \\ K_2 &= \sqrt{1-\alpha}(K_{II} \cos\omega + K_I \sin\omega) \end{aligned} \tag{4.17}$$

and the energy release rate from Eqn. 4.2 as

$$G = \frac{1}{\bar{E}_1}(K_I^2 + K_{II}^2) \tag{4.18}$$

The loading angle can be calculated from Eqn. 5.8. See also Table 7.2 on page 120 for a summary of the required calculations and typical resulting values.

From Fig. 4-5 it can be seen that the loading angle is not a linear function of the eccentricity S_0. The four-point bending mixed mode specimen is useful for fracture experiments in the range of $\phi = 90° \ldots 15°$. For a specimen with a height of 5.08 cm and a desired loading angle of 60°, an error in the position of the load of 1 mm results in a change of the loading angle of about 6°, whereas for a loading angle of 30°, the error is only about 2°.

Figure 4-5 is true for the three-point mixed mode specimen if flipped about a vertical axis. One has to exchange S_0 in the equation by $S/2 - S_0$. This means that for increasing eccentricities the loading angle is also increasing.

Chapter 5

Size Scale Effect

The size scale effect[1] is the most important practical consequence of fracture mechanics. Typical load–deflection diagrams for geometrically similar structures are shown in Figure 5-1. To illustrate the size effect, let us define a nominal stress in a structure as simply $\sigma_N = P/bd$, where P is the load at failure and b and d the specimen dimensions.[2] Most structures are designed using methods (such as plastic limit analysis, elastic analysis with allowable stress, or any other method that uses strength limits or failure criteria in terms of stresses) for which the nominal stress σ_N is constant, hence independent of structure size. If one plots the formulas of these methods, which are all of the same form, as (σ_N vs. $\ln(size)$), they all appear as

a straight line as in Fig. 5-2. Therefore, failures that are calculated according to yield or strength criteria exhibit no size effect.

To define a size scale effect, geometrically similar structures are compared in terms of the nominal stress σ_N at failure. If the nominal stress is equal for all sizes of specimens tested, then there is no size effect. If, however, the stress is not independent of the size, one refers to this as a size effect. Figure 5-1 shows load–deflection diagrams of geometrically similar structures of different sizes, indicating decreasing nominal stress at failure with increasing structure size.

[1] The terms size scale effect and size effect are used interchangeably in this thesis. However, the first term is more specific.

[2] The nominal stress does not have to be an actual stress in the structure.

In contrast to the analytical methods which exhibit no size effect, failures that are calculated according to linear elastic fracture mechanics (LEFM) exhibit a very strong size effect, as shown in Fig. 5-2. In the (σ_N vs. ln($size$)) plot, LEFM is represented as a line with the slope -1/2. The true behavior of concrete structures, including reinforced ones, is transitional, as illustrated by the solid curve in Fig. 5-2. The curve approaches the horizontal line for very small structures and the inclined line of linear fracture mechanics for very large structures.[3] It seems obvious that such a size effect needs to be included into the building design code provisions, but only few European countries have done so. In this thesis, the approximate size effect law developed by Zdeněk P. Bažant is used [*Bažant* (1992), *Bažant et al.* (1990a)]. A brief derivation of Bažant's size effect law is included here for completeness.

5.1 Review of the size scale effect law

The nominal stress at failure, which is used to describe the size effect, can be written as

$$\begin{aligned} \sigma_N &= c_n \frac{P_u}{bd} \quad \text{for two–dimensional similarity,} \\ \sigma_N &= c_n \frac{P_u}{d^2} \quad \text{for three-dimensional similarity,} \end{aligned} \tag{5.1}$$

where P_u is the load at fracture or the maximum load, b is the specimen thickness, d is a characteristic dimension of the specimen, preferably its length or height, and c_n is an arbitrarily chosen factor. It should be noted that the nominal stress σ_N does not have to be an actual stress in the structure. The factor c_n can be $c_n = \frac{3l}{2d}$, which gives the exact stress for a simply supported beam of length l, or $c_n = l/d$ for the plastic bending stress, but it can also be $c_n = 2\frac{(2+\alpha_0)^2}{1-\alpha_0}$ with $\alpha_0 = a_0/d$ and a_0 as the initial crack length. Bažant now makes the hypothesis that the energy dissipated at failure is a smooth function of the specimen size and the fracture process zone

[3] There is another size effect with respect to ductility. The larger a structure, the more brittle it becomes.

width. The fracture process zone width[4] is also considered constant. Bažant showed further [*Bažant* (1986)] that by simple similitude arguments and dimensional analysis the nominal stress at failure is of the form

$$\sigma_N = Bf_t'\{\beta[1 + \beta^{-1} + A_1\beta^{-2} + A_2\beta^{-3} + \ldots + A_n\beta^{-n}]\}^{-1/2}, \quad \text{with}\beta = d/d_0 \quad (5.2)$$

where B, d_0, $A_1 \ldots A_n$ are empirical coefficients, f_t' is a measure of the material tensile strength, and $\beta = d/d_0$ is the relative structure size. Eqn. 5.2 "represents an asymptotic expansion with respect to an infinitely large specimen" [*Bažant et al.* (1990a)]. A truncation of Eqn. 5.2 after the linear term is justified for a size range of 1:20 [*Bažant* (1987)]. That leads to the size effect law proposed by Bažant: [*Bažant* (1985), *Bažant* (1984)]

$$\boxed{\sigma_N = Bf_t'\left(1 + \frac{d}{d_0}\right)^{-1/2}} \quad (5.3)$$

where B and d_0 are empirical coefficients depending on the type of failure and the geometry of the specimen. If these coefficients are known for a particular failure and overall specimen geometry, the nominal stress at failure can be calculated depending on the characteristic dimension d of the specimen in question. Furthermore, since d is known, one can calculate the so–called brittleness number $\beta = d/d_0$, as will be discussed in Section 5.3. This stress is then equal to the stress obtained from Eqn. 5.1. It should be pointed out that the size effect law in Eqn. 5.3 can be used to express the size effects in pure compression, tension, or bending, as will be discussed in Section 5.6.

From Eqn. 5.3, it can be seen that for very large structures ($d \gg d_0$), one obtains the size effect of linear elastic fracture mechanics, which is of the form $\sigma_N = \text{constant}/\sqrt{d}$.[5] For very small structures ($d \ll d_0$), Eqn. 5.3 leads to $\sigma_N = Bf_u$, which is the nominal stress at failure as it is computed from the plastic limit analysis,

[4]The width of the crack band. The fracture process zone length is not constant; it decreases with increasing structure size.

[5]This is based on the assumption that in LEFM the crack length at failure is equal to the initial crack length, which is true for an infinitely large structure.

elastic analysis with allowable stress, etc. Hence, the size effect law in the form of Eqn. 5.3 gives a transition from the plastic limit to the linear elastic fracture mechanics size effect as can be seen in Fig. 5-2. One of the major advantages of Bažant's size effect law is that it can be transformed to a linear regression plot

$$Y = AX + C \tag{5.4}$$

where

$$X = d \tag{5.5}$$

$$Y = \left(\frac{f_t'}{\sigma_N}\right)^2 \tag{5.6}$$

$$B = 1/\sqrt{C} \tag{5.7}$$

$$\text{and} \quad d_0 = \frac{C}{A} \tag{5.8}$$

As can be seen in Fig. 5-3, A is the slope of the regression plot that is obtained by plotting (Y vs. d), and C is the Y–intercept of the regression line. Thus, it is fairly straightforward to get the values B and d_0 for the size effect law from a regression analysis of the test data. It should be noted, however, that for a proper derivation of the size effect plot the values of C and A must be positive. The size effects of different types of structures are compared to the size effect law in Figures 5-4 and 5-5.

The two fundamental hypotheses underlying the above derivation are: (1) the energy required to propagate a crack or crack band of unit width by unit distance is approximately constant, and (2) the potential energy released by the structure is a function of the length of the fracture and the size of the fracture process zone.

5.1.1 Effect of Maximum Aggregate Size

The fracture and size effect parameters are valid only if obtained from similar specimens. That includes the specimen dimensions as well as the maximum aggregate size (MSA). Therefore, adjustments to the size effect law must be made to account for changes in MSA. Bažant [*Bažant* (1992)] proposed to replace the measure of the

material's tensile strength f_t' in Eqn. 5.3 by

$$f_t' = f_t^0 \left(1 + \sqrt{\frac{c_0}{d_a}}\right) \tag{5.9}$$

where f_t^0 is the tensile strength for a certain reference concrete with a particular MSA, c_0 is an empirical constant, and d_a is the maximum aggregate size of the different concrete. The factor c_0 can be determined from the reference concrete.

It should be noted that this equation is of the same form as one derived for the effect of grain size on yield strength of polycrystalline solids using dislocation theory.[6]

The introduction of the factor d_a into the size effect law shifts the size effect curves vertically and horizontally because d_0 is now $d_0 = nd_a$, where n is roughly constant for similar aggregate types.[7] Some curves are shown in Figure 5-6. Bažant [1992] concludes that for small structures, a small MSA is advantageous, whereas for large structures, such as dams, a large aggregate size seems to be beneficial. However, this needs to be researched further. Fracture tests on dam concretes by Saouma et al. [*Saouma et al.* (1989)] indicate that aggregate shape has a much stronger influence than aggregate size.

5.2 Nature of the Size Effect

5.2.1 Is the Size Effect of Statistical Origin?

The size scale effect is due to energy release and therefore not a statistical problem. Although one may find a statistical nature of the fracture behavior of a uniformly tensioned concrete bar, for example, the size effect cannot be universally explained with statistical considerations. Bažant discussed the applicability of a Weibull–type theory to the size effect in [*Bažant* (1992)]. He points out that although one may fit the Weibull coefficients to one particular size effect, say uniform tension, those parameters will be unable to predict the size effect in another failure mode.

[6] The so–called Petch formula.

[7] It may not hold for a comparison of river and crushed aggregates, for example.

The intrinsic shortcoming of a Weibull–type explanation of the size effect is that it assumes a structure to fail at the onset of cracking. This is called a weak link theory. Since concrete structures undergo a significant amount of redistribution of stresses prior to failure and spreading of cracks into crack bands, such a theory is not applicable. Therefore, a proper explanation of the size effect must be derived from energy arguments of fracture mechanics.

However, there may be a statistical size effect "on top" of the fracture mechanics size effect because the probability of a larger flaw that initiates crack growth is greater in a larger structure.

5.2.2 Energy explanation of the size effect

(Adapted from [*Bažant* (1992)], Page 14 ff.)

Consider a uniformly stressed plate as in Figure 5-7 with a crack band of the initial length a_0.The formation of a crack band of thickness h reduces the strain energy density $\sigma_N^2/2E$ in the less densely cross hatched area to zero. When the crack band of the length a extends by $\triangle a$, the strain energy to form this new crack surface is supplied by the densely cross hatched strip of the width $\triangle a$. If the failure modes of specimens of different sizes are similar, which is a condition for the applicability of the size effect law, then the absolute crack length at failure of a larger specimen will be greater than the ultimate crack length of a smaller specimen. Therefore, the area of the densely cross hatched strip is also greater for a larger specimen, given roughly by $h \triangle a + 2ka \triangle a$, where k is a constant that takes the shape of the structure into account. Hence, in a larger structure, more energy is released per unit extension

of a the crack band. The energy released from the strip is $-\delta\Pi/\delta a = G_f\, b$, that is

$$\frac{1}{\triangle a}(h \triangle a + 2ka \triangle a)\frac{\sigma_N^2}{2E} = G_f b \tag{5.10}$$

where Π is the potential energy stored in the structure, b is the thickness, and G_f is the fracture energy release rate, the energy required to form a unit area crack extension. Solving the above equation for the nominal stress at failure, one arrives at

the size effect law proposed by Bažant [1984]:

$$\sigma_n = Bf_t'(1+\beta)^{-1/2} \tag{5.11}$$

where $\beta = d/d_0$, $B = (2G_f Eb/h)^{1/2}/f_t'$, $d_0 = (h/2k)(d/a)$ is a reference size depending on the shape of the structure, f_t' is a measure of the tensile strength, and h is the width of the crack band.

The above explanation holds not only for a crack band but also for a sharp line crack. There is always a fracture process zone ahead of the crack tip in concrete structures. The stress in this fracture process zone drops gradually from f_t' to zero. The length c of this fracture process zone can be considered roughly constant. Therefore, the elastically equivalent crack length, which causes the release of energy into the crack, is by a distance c longer than the crack length a. When the crack extends by a distance $\triangle a$, the energy released by the corresponding strip of the area $k(a_0+c)$ is

$$\frac{1}{\triangle a} 2k(a_0+c)\,\triangle a \frac{\sigma_N^2}{2E} = G_f b \tag{5.12}$$

Solving again for the nominal stress, on arrives at the size effect law of Eqn. 5.11, where $B = (EG_f b/kc)^{1/2}/f_t'$, and $d_0 = c(d/a)$ =constant.

5.3 Brittleness Number

A measure to express the brittleness of a structure has been proposed by several investigators, among them Hillerborg and Jenq. However, only the brittleness number derived by Bažant [1987] describes the brittleness of a structure independent of its shape. On the basis of the size effect law in Eqn. 5.11, the brittleness number is expressed as

$$\beta = \frac{d}{d_0} = B^2 g(\alpha_0) d \frac{f_t'^2}{EG_f} = AB^2 f_t'^2 d \tag{5.13}$$

where $g(\alpha_0)$ is the nondimensional energy release rate defined by the total energy release rate in the form $G = g(\alpha_0)P^2/(Eb^2 d)$. Using $G = K_I^2/E$, $g(\alpha_0)$ can be

determined from the equation for K_I, which is always of the form $K_I = f(\alpha_0)P/b\sqrt{d}$, and $f(\alpha_0) = \sqrt{g(\alpha_0)}$. The factor $f(\alpha_0)$ can be obtained from handbooks.

The brittleness number agrees with the transition of the size effect law; in fact, the size effect law is plotted usually as the normalized nominal stress (σ_N/Bf_t) vs. the brittleness number β. When $\beta > 10$, the failure may be analyzed using linear elastic fracture mechanics (LEFM). When $\beta < 0.1$, a strength criterion or plastic limit analysis may be used to determine the failure. The error involved in these two boundaries is less than 4.7 % [*Bažant* (1992), p. 62]. For $0.1 < \beta < 10$, nonlinear elastic fracture mechanics must be used to calculate the failure. If an error of less than 2 % is desired, these boundaries must be expanded to 1/25 and 25, respectively.

Since the brittleness number proposed by Bažant is universal, because independent of structure shape, it may easily be included in current limit–analysis based code formulas. It would take into account nonlinear fracture mechanics by replacing the nominal stress at ultimate load, $v_u^{\min}$ in the ACI–Code, with the expression

$$\sigma_N = \frac{v_u}{\sqrt{1+\beta}} \geq v_u^{\min} \tag{5.14}$$

One has to be aware of a possible transition in the failure mode, as in the Brazilian disk specimen. Bažant points out [*Bažant* (1992)] that the methods to calculate d_0, on which β depends, still need to be researched further.

5.4 Parameter–free Notation of the Size Effect Law

The size effect law makes it possible to calculate the failure load within the nonlinear range using linear elastic fracture mechanics. To do this, the parameters G_f and c_f must be known. They represent, respectively, the energy release rate and the size of the fracture process zone of an infinitely large specimen. The first can be calculated from $G_f = g(\alpha_0)f_t^2/c_n^2AE$, where α_0 is the initial relative crack length (a/d), and the latter from $c_f = g(\alpha_0)d_0/g'(\alpha_0)$, for which not only the function $g(\alpha_0)$ but also

its derivative with respect to the crack length must be known [*Gettu et al.* (1990)]. This also implies that, if $g(\alpha_0)$ and $g'(\alpha_0)$ are known, one can determine the fracture energy and fracture process zone length of an infinitely large specimen from the size effect analysis using linear fracture mechanics.

Using these two parameters, the definition for $d_0 = c_n g'(\alpha_0)/g(\alpha_0)$, and that

$$B = \frac{c_n}{f_t'} \left(\frac{EG_f}{c_f g'(\alpha_0)} \right)^{1/2} \tag{5.15}$$

one can rewrite the size effect law as

$$\sigma_N = c_n \left(\frac{EG_f}{g'(\alpha_0)c_f + g(\alpha_0)d} \right)^{1/2} \tag{5.16}$$

This formulation of the size effect law contains only true material parameters, G_f and c_f. The effect of the structure shape is included in the factors $g(\alpha_0)$ and $g'(\alpha_0)$. The above equation can also be written as $\sigma_N = c_n(EG/g(\alpha)d)^{1/2}$, but this expression is only useful if the actual crack length α and the actual fracture energy G have been determined, which is practicable when using R–curves.

5.5 Explanation of the Size Effect on Ductility

Concrete structures consist of undamaged and damaged sections. This can be illustrated by a seriell coupling of uncracked, hence elastic, material, and cracked material. This is shown in Figure 5-8 on Page 80. If the elastic body is sufficiently soft, the coupled system can produce what is called a snap–back effect. It is very difficult to obtain exact load displacement curves for concrete even with extremely stiff loading machines. The behavior is unstable and the structure will fail at the maximum deflection u_{cr}. The deflection u_{cr} is a combination of the displacement due to cracking and the displacement due to elastic deformation of the elastic body. The less stiff the spring and the more distributed cracking occurs, the larger the ultimate displacement u_{cr}. Therefore, u_{cr} can be regarded as a measure for the structure's ductility. A stiffer spring element, which is equivalent to a larger size of the structure, would result in a

smaller u_{cr} and, conse

quently, less ductility. Ductility is, therefore, not a material property but a structure property, depending on the material and the size.

Hawkins [*NAT*(1984)] reported 29 provisions in the ACI–Code that seem to be empirical but could be explained by fracture mechanics. They include ductility requirements and conditions for crack spacing, crack width, and minimum reinforcement.

5.6 Experimental Evidence for the Size Effect

A large number of tests has been carried out to verify the size effect law in Eqn. 5.3. The different types of failure include

1. Diagonal shear failure of beams [*Bažant et al.* (1986), *Bažant et al.* (1990b)],
2. Punching shear failure of slabs [*Bažant et al.* (1987)],
3. Torsional failure of beams [*Bažant et al.* (1988b)],
4. Pullout failure of reinforcing bars [*Bažant et al.* (1988a)],
5. Double-punch tests of cylinders [*Marti* (1989)].

All these failures were shown to comply with Bažant's size effect law Eqn. 5.3). Some examples are shown in Figure 5-5.

This work shows the applicability of the size effect law to interface fracture in high–strength concrete–granite composites, as discussed in Chapter 7.

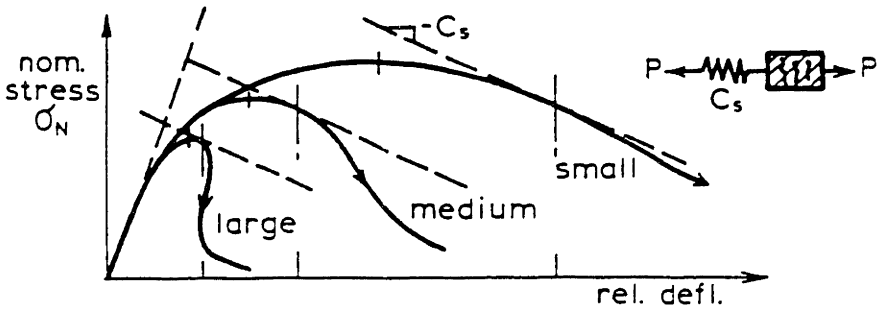

(From reference [*Bažant* (1992), p.11].)

Figure 5-1: Load–deflection diagrams for geometrically similar structures of different sizes

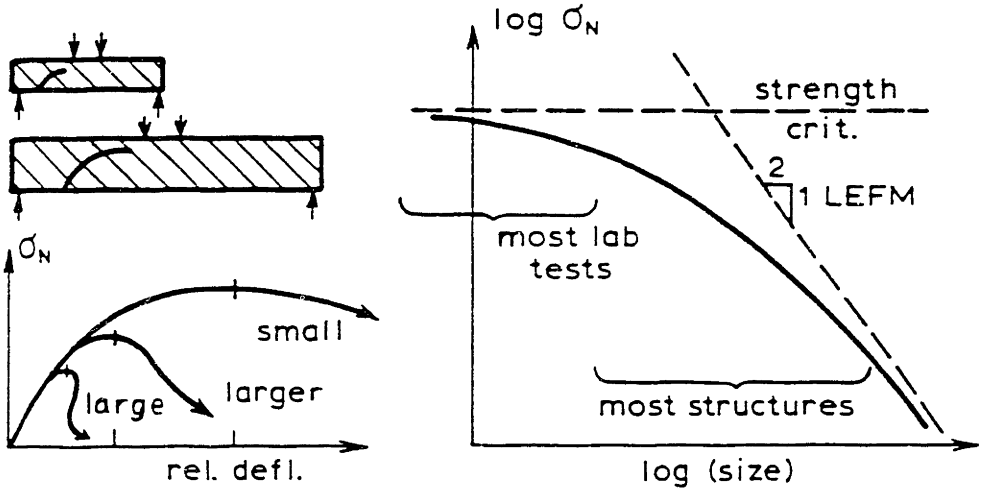

(From reference [*Bažant et al.* (1987)].)

Figure 5-2: Size effect of concrete structures

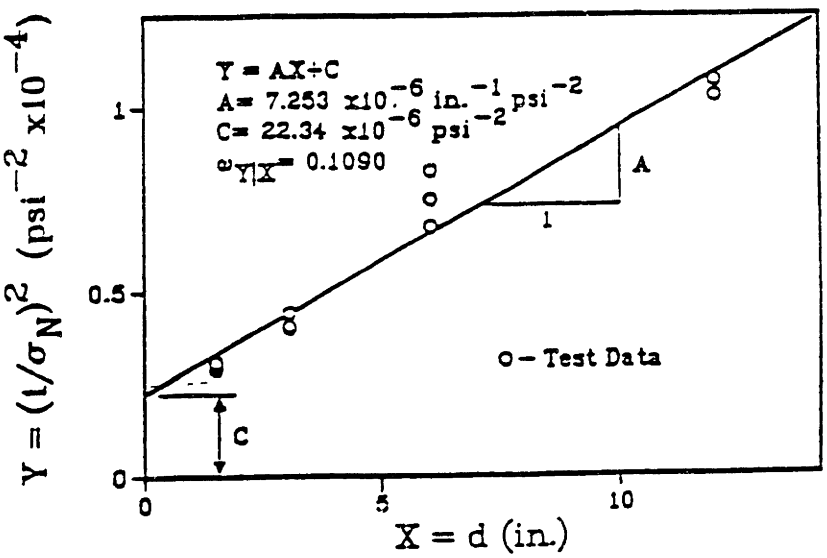

(From reference [*Bažant* (1992), p.93].)

Figure 5-3: Sample regression plot of test data for size effect law

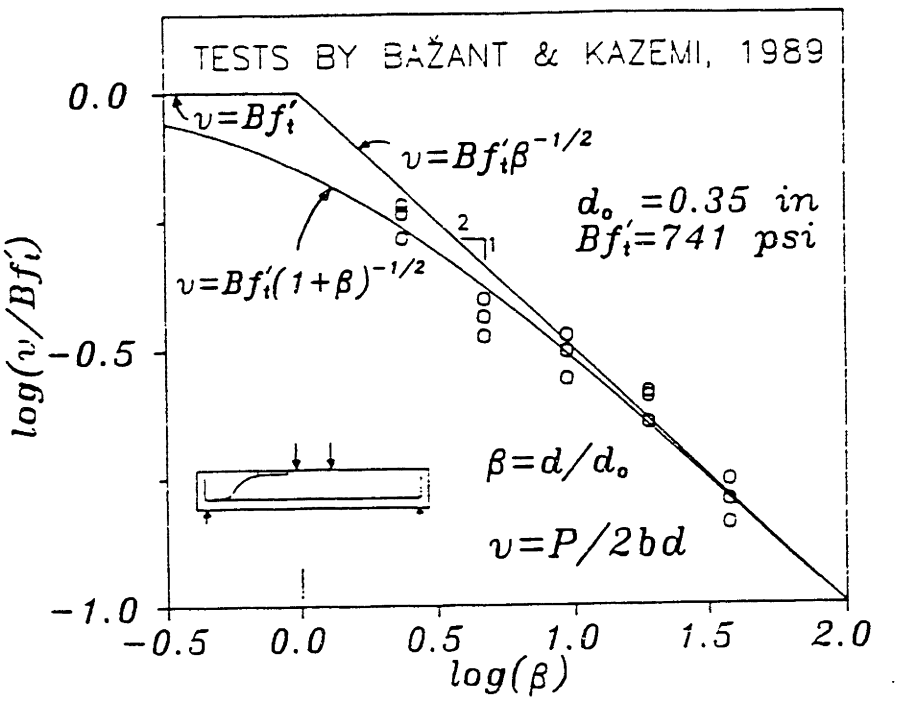

(From reference [*Bažant* (1992)].)

Figure 5-4: Sample size effect plot for diagonal shear failure

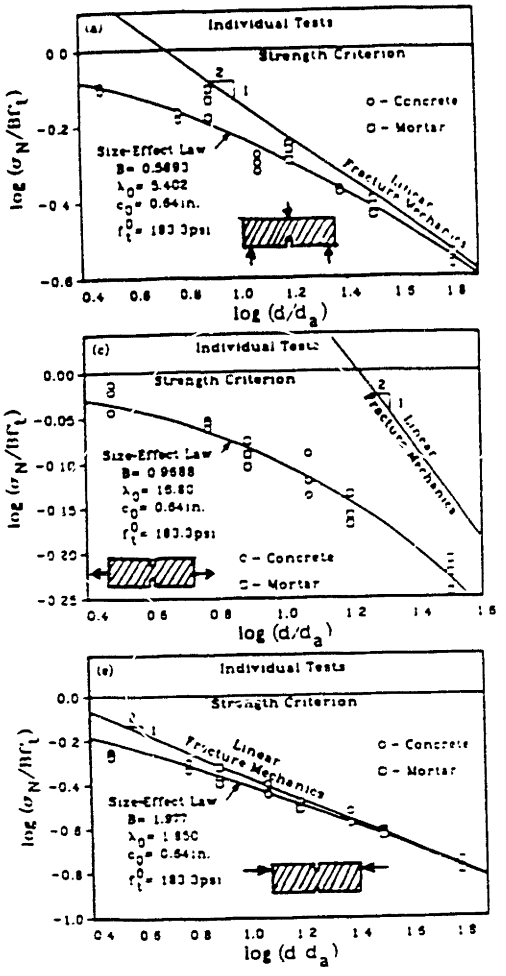

(From reference [*Bažant* (1992), p.61].)

Figure 5-4: Comparision of size effect law with test data on specimens with different geometries and loading conditions.

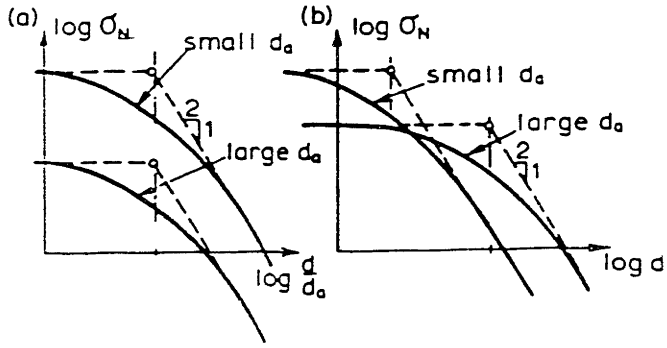

(From reference [*Bažant* (1992), p.61].)

Figure 5-5: Sample curves for the structural size effect for different aggregate sizes

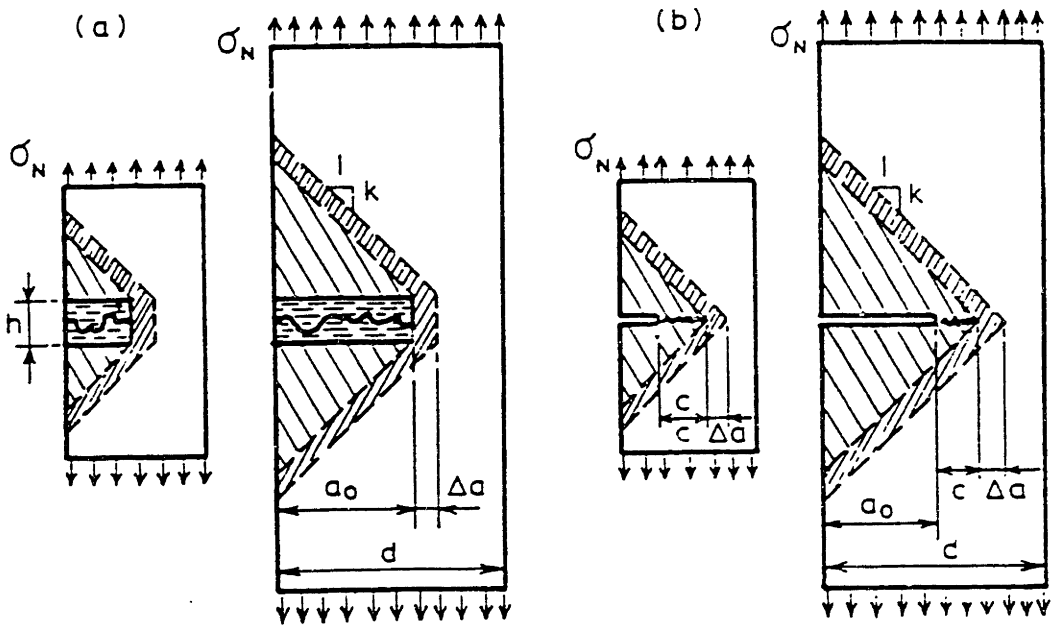

(From reference [*Bažant* (1992), p.15]

Figure 5-6: Areas of energy release in similar specimens of different size for single crack and crack band model

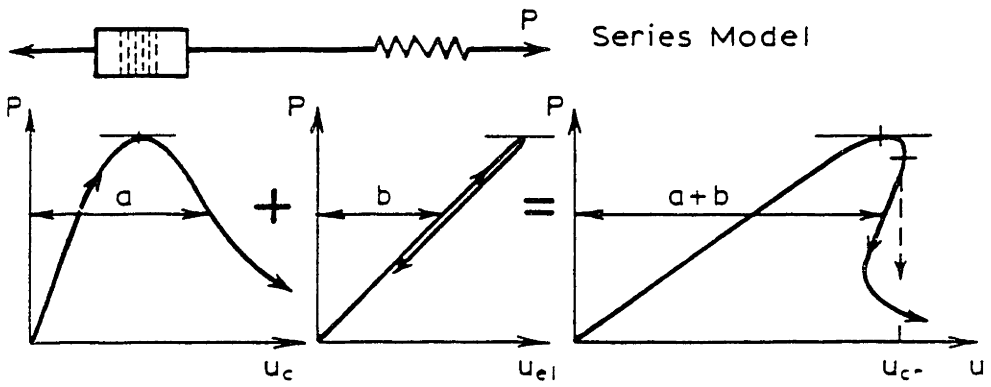

(From reference [*Bažant* (1992), p.23].)

Figure 5-7: Simplified series model for concrete as explanation for post–peak behavior

Chapter 6

Experimental Work

This chapter provides information about the specimens, materials for mortars, rocks, mix–proportions, and equipment. It also gives the procedures for the manufacturing and the testing of sandwiched specimens.

6.1 Introduction

Most researchers consider concrete a one–phase material. This simplification is reasonable for most applications. However, a two–phase model which describes, for instance, the mortar and the aggregate separately is able to describe the behavior of concrete more accurately. Consequently, a composite beam specimen was used to investigate the two–phase nature of concrete more closely.

Concrete consists of numerous constituents and chemical compounds, which have chemical bonds or physical interfaces with one another. Many researchers believe that the interfacial zone is the weakest part in the concrete [*Maso* (1992)]. Changes in the aggregate–mortar interface may lead to higher strength when porosity and crystal size are reduced (see Chapter 2). The fracture behavior in high –strength concrete appears to be very different from that of normal strength concrete [*Bažant* (1992), *Lee* (1993)]. For example, while fracture in normal–strength concrete usually occurs around aggregate particles, hence, along the interface, a crack generally travels through aggregate particles in high–strength concrete, indicating a stronger interfacial zone. Since the

interface has been found to be so important, it would be desirable to quantify the properties of interfaces and their contribution to the overall performance of the concrete.

However, little research has been done to develop an interface fracture mechanics approach to fracture in concrete. The works of Lee [1993] and Büyüköztürk [1993], Mitsuru and Mitsunori [1986], Oumera [1991], Struble [1988], Alexander and Mindess [1992], and others have laid the foundation for this approach. This work contributes information about interface fracture parameters for certain aggregate–mortar combinations and the influence of roughness on these properties. Most of all, it investigates the size effect in interface fracture mechanics. The experimental work was divided into four phases (See Section 7.1 on page 118):

Phase 1: A first test series on full–length beams in Mode I to show the reproducibility of Lee's results [*Lee* (1993)] and to get an idea of the order of magnitude of the influence of aggregate roughness on the interface fracture parameters.

Phase 2: A second tests series on full–length beams in different loading angles that was intended as the core of this study. It led (1) to the development of the compact sandwiched beam specimen, (2) an improved test set–up for the determination of the size effect, (3) rough data for interface fracture properties of the chosen aggregate–mortar interfaces for different loading angles, and (4) the decision to use only Mason granite in all following tests because no differences between the two granites could be detected.

Phase 3: A test series designed to assess the mechanical properties of the rocks and mortars used.[1]

Phase 4: A final test series using the newly developed compact sandwiched beam specimen to establish data regarding the size effect and the

[1]For each set of beam specimens, the mortar was tested for compressive strength and Young's modulus.

influence of aggregate roughness under different loading angles. This test series was the core of this study.

6.2 Specimens

6.2.1 Details of Sandwiched Specimens

The specimens were manufactured with all dimensions in the ratio of 1:2:3. For an investigation of the size effect, not all dimensions have to be similar, according to Bažant [*Bažant* (1992)]. Note that Eq. 5.1 on page 67 is given also for specimens that are similar in two dimensions only. However, for this study, all three dimensions were kept similar to obtain as accurate results as possible.
The actual sizes of the beams were (length × height × width):

Small: 177.8 mm × 50.8 mm × 25.4 mm (7 inches × 2 inches × 1 inch)

Medium: 355.0 mm × 101.6 mm × 50.8 mm (14 inches × 4 inches × 2 inches)

Large: 533.4 mm × 152.4 mm × 76.2 mm (21 inches × 6 inches × 3 inches)

The relative crack length a/d was held constant at $\mathbf{a/d = 0.375}$.[2]

The Artificial Crack

The specimen has a crack to define the starting point of the fracture. Ideally, the crack is located directly at the interface to initiate an interface fracture. For the specimens used in this study, the crack was created using normal to low viscosity epoxy resin.[3] The resin was applied onto the aggregate surface so that an area with the depth of the desired crack was covered. The hardened epoxy has a very smooth surface and, consequently, no mechanical bond between mortar and epoxy is possible. This has been proven with a scanning electron microscope investigation of the epoxy surface

[2]The dimensions and the crack length for the small sandwiched beam are the same as for the beams Lee used [*Lee* (1993)] so that the results could be compared. In a preliminary test, he arrived at these measures as the most useful ones.

[3]The useful type and brand of epoxy resin was determined during the tests within the first phase of the experimental work.

after testing (Fig. 7-33). Also, Hutchinson has used this method of epoxy coating [*Suo et al.* (1989)]. Although the crack will not be perfectly thin with a blunt crack tip and there may also be irregularities in the alignment of the line of crack tip, this method has proven to produce consistent

results. One might argue that while there may not be mechanical interlock between the mortar and the epoxy resin, there will be adhesion between the two. I believe that this phenomenon is advantageous since it resembles the conditions of a very thin crack with residual cohesive stresses between the crack faces. I do not recommended creating the artificial crack with the cut of a diamond saw because the vibrations during the sawing will most probably create microcracks at the interface and the fracture loads will be much lower, probably making the test not representative of real mortar–aggregate interfaces.

The Compact Sandwiched Beam Specimen

It is important to notice that the beams for the last test series (Phase 4) were compact sandwiched beam specimens. This type of specimen is a modification of the previously used sandwiched beam specimen. The main difference is that the compact specimen is manufactured in two stages: first, only the central portion of the beam incorporating the aggregate slice is cast, and second, just before testing, this central portion is glued to previously manufactured concrete or aluminum beams using epoxy resin, resulting in beams of the same dimensions as reported above. The length of the central portion is equal to the respective beam height for all three sizes (Fig. 4-3 and 6-4).

This change was made to eliminate the effects of shrinkage, thermal stresses, and possible damages due to handling and storage. It has proven successful in this study. The large scatter obtained in the tests on unchanged, or full length, beams was greatly reduced after introducing the compact beams. The two major problems with full length beams were handling and storage. The interface is weakest when the specimens are young, and many specimens did not even "survive" the demolding. The storage proved difficult because a totally flat surface is hard to find; therefore, the aggregate/mortar interface endured stresses over long periods of time, which may

cause the interface to develop microcracks. Additional advantages of the compact beams are that the same molds can be used, which now yield twice the number of specimens, and that less concrete is needed to produce one set of specimens. However, the time required to manufacture one set of specimens from the cutting of the aggregate to the testing of the beams

increased from 3 days to $3\frac{1}{2}$ days due to the gluing.

The thickness h of the aggregate layer was 0.452 cm for the small, 0.464 cm for the medium, and 0.601 cm for the large specimens. The theory presented in Chapter 3 assumes a very thin interlayer. Therefore, as small a thickness of the aggregate as possible should be used. The above values appeared to be a lower limit, considering that buckling must be prevented when the aggregate slices are fixed with small wedges in the molds before the mortar is cast. Also, the granite behaves in a more homogeneous fashion when its thickness is more than about twice the average grain diameter.

Geometry of the Test Set–Ups

For all Mode I tests, a quarter point bending test arrangement was used, as indicated in Figure 4-2. The length of the top loading beam was one half of the beam length. The line of the load coincides with the side of the aggregate that bears the crack.

For all mixed mode tests, a set-up as shown in Figures 4-3, 6-4, 6-5, and 6-6 was used. To determine a useful loading arrangement, the geometry was changed during the tests in Phase 2 of the experimental program (full length specimens) and for the test on compact specimens. Theoretically, the test results are independent of the choice of S_1 and S_2 and depend only on S_0, which determines the loading angle, as described in Section 4.3.

Geometries for Full–Length Specimens

The parameters S_1, S_2, and S_0 for the "old" geometry and a small specimen were as follows:

S_1=4.656 cm, S_2=6.773 cm, S_0=0.846 cm

The so–called new geometry (only for full–length beams) was:

S_1=2.54 cm, S_2=7.62 cm, S_0=0.846 cm

The above choices of S_0 resulted in a loading angle of about 45°. For medium and large beams, the above distances must be doubled or tripled, respectively.

Geometry for Compact Specimens

The loading geometry for compact beams was (for small beams):

Small Beams: S_1=3.81 cm S_2=7.62 cm	
Approx. lading angle $\hat{\psi}^*$ [°]	S_0 [cm]
61.8	0.416
29.2	1.463
*Because of the influence of ω and ϵ, the exact loading angle depends also on the material combination. Here, an offset of ω = 1.23° takes this into account.	

For medium and large beams, the values for S_1, S_2 and S_0 must be doubled or tripled, respectively. To determine the required S_0 for a desired loading angle for the four–point shear test, the following equation may be used: $\phi = \tan^{-1}(f_s d/f_b S_0)$. See Figure 4-5.

6.2.2 Materials for Mortars

For the production of high–strength mortars, the following materials were used: cements Type I and Type III, concrete sand, condensed silica fume (SF), high range water reducer (HRWR), water, and, for some batches, retarder.

The selection of the materials for the mortars was governed by the decision to use "real-life" construction materials, first, because the results should be repeatable with little effort, and, second, because the results from this work should be useful in current high-strength concrete construction practice. Both of these aims would have been harder to fulfill with high-edge products such as laboratory cement, especially ground and graded aggregate, such as silica sand or carborundum, etc., though these materials would have yielded much higher fracture toughnesses and more consistent test results.

Cement

The cements that were used for the tests were Dragon Type I portland cement for 28-day compressive strength and Dragon Type III portland cement for 7-day compressive strength mortar. Both cements were purchased in 90-pound bags directly from a construction supplier.[4] During preliminary testing, this cement has proven useful for the production of HSC. No serious rapid hardening reaction was observed. (See Section 2.7.1.) However, a stiffening occurs after approximately 20 minutes. The cement bags were stored in the laboratory mixing room, wrapped in plastic garbage bags, and placed in large garbage cans to protect the cement from humidity. No cement older than four weeks was used to ensure consistent mortar quality. The cement used to prepare small specimens was passed through a No. 50 sieve to break up the lumps. However, the large amounts of cement needed for medium and large specimens were not sieved,

which reduced the 28-day compressive strength of the "standard" 12,000 psi (83 MPa) mix by about 300 psi (2 MPa).

Sand

It is important to use a strong, sound, and well-graded sand in order to achieve a high and consistent mortar compressive strength. Five different types of sand from

[4]Waldo Bros. & Co., 202 Southampton Road, Roxbury, MA 02119, Tel. (617) 445-3000

various suppliers in the Boston area were tested during preliminary testing. Most of the sands had too fine a grading. Sand as it is used for ready–mix concrete production by Boston Sand & Gravel Co.[5] was found sufficient. It has a fineness modulus of 2.65. The grading of the sand is shown in Table 6.1. The washed sand was taken directly

Boston Sand&Gravel Concrete Sand					
Sieve No.	Opening [mm]	Opening [inch]	Weight ret. [g]	Passing [%]	Retained [cum.%]
8	2.36	0.0937	0	22.76	22.76
16	1.18	0.0469	921	39.22	61.98
30	0.60	0.0234	1587	23.01	84.99
50	0.30	0.0117	931	10.77	95.76
100	0.15	0.0059	436	4.22	—
Pan	—	—	171	—	—
Σ			4046	99.98	265
Fineness Modulus: (=cum.%ret./100)					**2.65**

Table 6.1: Grading of the concrete sand from Boston Sand&Gravel

from a pile at the concrete plant, dried (to ensure a constant water content of the mortar) at 105°C for 6 hours, cooled, and passed through a No. 8 sieve (opening 2.36 mm or 0.0937 inch). It may be noted, however, that the mortars used by Lee [*Lee* (1993)] were produced with a brick mortar sand that is sold by Waldo Bros.[1] in 40–lb bags. This sand has a fineness modulus of 2.21. Such a sand is not recommended for the following reasons. A sand with a low fineness modulus contains larger amounts of fine particles, which absorb more water and result in lower workability of the fresh mortar. Thus, water or water reducer must be added, which, in turn, might entrain air into the mix. A high fineness modulus indicates a greater portion of larger particles. Such a sand lacks the "lubricating" effect of small particles. Therefore, a mortar made with a very coarse sand is of inferior workability or needs more water or plasticizer. In Neville [*Neville* (1973)] the optimal value of the fineness modulus for concrete sand is reported to lie within 2.6–3.0. From preliminary tests, I found the optimum value

[5]Boston Sand&Gravel Co., 169 Portland Road, Boston, MA 02108, Tel. (617) 227-9000

of the fineness modulus of the sand for both, strength and workability of the mortar, to lie between 2.4 and 2.9. For one test, a sand with a fineness modulus of 2.81 was compared to one with 2.65. Both sands were used with the same mix proportions of Mix No. 3 in Table 6.2 on page 103. The mortar containing the sand with the higher fineness modulus (2.81) yielded a compressive strength about 3.6 MPa higher than the mortar containing the sand with a fineness modulus of 2.65, whose 28-day compressive strength was 83.5 MPa, but had an unsatisfactory workability.

Silica Fume

The only mineral admixture used was condensed silica fume in slurry form. The brand name of the product is Force 10,000. It is produced by W. R. Grace & Co.[6] "Force 10,000" is a microsilica containing 48% silica fume (i.e. SiO_2) along with 2% foreign particles and 50% water by weight. The slurry is dark gray and viscous. It is important to take its water contents into account for the mix design. The containers holding 5 Gallons (20 l) were stirred using a power stirrer before use. See Section 6.2.3.

Admixtures

An important admixture for the production of high strength concrete is high range water reducer (HRWR), also called superplasticizer. The brand name of the HRWR used is WRDA-19 (ASTM C-494 Type A & F) produced by W. R. Grace. WRDA-19 is an aqueous solution of a modified naphthalene sulfonate, has a low viscosity, and contains no chloride. Naphtalene sulfonate is one of the few superplastizisers that do not entrain much air even in higher dosages. However, an increase in the air volume of 1-2% must be expected. From my experience with the preliminary tests, a superplasticizer content of more than 4% of the cement weight should be avoided.

Also used for preliminary tests was a retarding agent from the same company, DARATARD-17, in an attempt to reduce shrinkage effects. However, all retarding

[6] W. R. Grace & Co., 62 Whittemore Avenue, Cambridge, MA 02140, Tel. (617)-876-1400

admixtures can delay only the initial set of the concrete or mortar but not the duration of the hydration reaction and, therefore, not the amount of hydration energy released per unit time. The high–strength mortars produced with retarder had a compressive strength of about 5.5 MPa (800 psi) higher than the same standard 83 MPa (12,000 psi) (Mix No. 3 in Table 6.2 on page 103) mix without retarder. This increase is due to the longer available time to activate the reactants before the hydration reaction starts. Thus, retarder cannot reduce shrinkage problems but can improve the strength of the mortar or concrete. This strengthening effect is often used for the production of high strength concrete. However, retarder was not used to produce the mortars for the tests on sandwiched beams.

6.2.3 Mix Proportions

Although only two different mortar strengths were used for the tests, I have reported the mix proportions and the resulting compressive strengths from all batches, including the preliminary ones. Note that the mix proportions are reported referring to the true silica fume content of the mineral admixture. When silica fume slurry is used, its water content must be taken into consideration. In that case, the water/cementitious constituents ratio is calculated as

$$\frac{W}{(C+SF)} = \frac{(W+W_{SF})}{(C+SF_{SF})} \tag{6.1}$$

where W is the water content, W_{SF} is the water content of the silica fume slurry, SF_{SF} is the silica fume content of the slurry, SF is the true silica fume content of the mix, and C is the cement content of the mix.

Workability is usually measured with slump. However, for mortars and concretes containing large amounts of superplasticizer, values for the slump are misleading. The mix appears usually stiff but becomes viscous when compacted, especially when vibrated. In Table 6.2, a somewhat subjective measure is reported. This measure is based on observations of the consistency of the mix. Excellent workability means that the mix flows well when vibrated, good workability means that the mix flows

but needs further compacting with a rod to remove trapped air, and fair workability means that the mix can only be compacted using a rod.

Note that mix No. 8 in Table 6.2 yields almost the same compressive strength after 7 days as mix No. 3 after 28 days. These two mix proportions were used for the tests on sandwiched beams.

6.2.4 Testing of Mortars

Preparation of Specimens

For each batch of mortar, three cylinders (3 inch diameter by 6 inch height (7.62 cm × 15.24cm)) were cast according to ASTM-C192-90a. The mortar was placed in the PVC–molds in three layers, each layer compacted with a 5 mm (0.2 inch) rod, and tapped 10 times. When the mold was completely filled, it was externally vibrated for 1 minute. The cylinders were covered with plastic, demolded 24 hours later, and stored in lime–saturated water until testing 7 or 28 days after preparation.

Testing of Mortar Cylinders

The mortar cylinders were capped with high–strength gypsum (*Hydrostone*) according to ASTM-C617-87 to ensure flat and properly aligned ends.

Compression

Compression testing was conducted in compliance with ASTM-C39-86. The machine used was a 200-kip (100 t) Baldwin machine.[7] The loading rate was 0.05 inch/min (1.3 mm/min) in a displacement controlled test. The peak load was recorded by the data acquisition system. The specimens failed in an explosive manner and the types of failure were for all high–strength concrete specimens either 'Cone' or 'Cone and Split'.[8] The resulting compressive strengths of the mortars are reported in Table 6.2 on page 103.

[7]Described closer in Section 6.3.1.
[8]ASTM C-39-86, Fig. 2.

Young's Modulus

Because the elastic properties of the materials are needed to compute the interfacial fracture data, tests for Young's modulus were necessary. The tests were performed according to ASTM-C469-87a on a 60-kip open–loop hydraulic Baldwin machine. A yoke with two diametrically attached LVDT's[9] was fixed on the specimen at midheight as shown in Fig. 6-1. Each specimen was loaded three times, with data recorded by the acquisition system only from the last two loadings. The loading rate was 35 psi/s (241 kPa/s) and the data log rate was 1 second. The Young's modulus was calculated from the data according to

$$E = \frac{(S_2 - S_1)}{(\epsilon_2 - 0.00005)} \tag{6.2}$$

where E is Young's modulus, S_2 is the stress at 40% of the failure load, ϵ_2 is the corresponding strain, and S_1 is the stress at a strain of 50 millionth, i.e., 0.00005. Hence, the reported Young's moduli in Table 7.1 on page 119 are secant—moduli.

6.2.5 Rocks

The proper selection of the rocks to be used as aggregate in high strength concrete (HSC) is very important to achieve high compressive strength and good durability. The cheapest possible aggregate, high quality gravel, is not everywhere available. Therefore, crushed rock is often used to produce HSC. Quartzite, andesite, porphyrite, granite, traprock, basalt, limestone, sandstone, hornfels, gneiss, and rhyolite are considered good aggregates for HSC. Compressive strength is the most important property of the rock to look for. A good rock to be used as aggregate for high–strength concrete should have a compressive strength of 150 MPa (22,000 psi) or more. The tests for interface fracture properties focused on granite only because granite is one of the most widely used aggregates for high–strength concrete. The granite for this study was obtained from Fletcher Granite Co.[10]

[9] See Section 6.3.1 on page 99

[10] Fletcher Granite Company Inc., Groton Road, West Chelmsford, MA 01863, Tel. (508)-251-4031, Fax (508) 251-8773

Correction of Previous Work

Lee [*Lee* (1993)] used three different aggregate types to establish interface fracture data for a variety of mortar/aggregate combinations. Apart from granite, he used what he thought was quartzite and limestone. However, geologically these rocks were marble and rhyolite, respectively. This is a significant difference, since marble is much softer than quartzite. In addition, rhyolite has a very high ratio of Young's modulus to compressive strength, while for limestone, this ratio is low.

Description of Rocks

Six different rocks were considered: marble, rhyolite, "Old" Chelmsford granite, Chelmsford granite, Mason granite, and Deer Isle granite.

Chelmsford	A granite with fine grains, mostly gray with some white grains and few shiny dark mica particles.
"Old" Chelmsford	To distinguish it from the Chelmsford used for the tests in this study. It originates from the same quarry in Chelmsford, MA, and was used by Lee [*Lee* (1993)]. It has smaller grains than Chelmsford and has developed some clay at grain boundaries due to long exposure to air.[11]
Mason	Very small grains, mainly rose, white, and dark gray grains.
Deer Isle	Large grains, mainly gray and gray-brown plagioclase particles with some white quartzite.
Marble	Plain, white, and soft stone, no visible grains
Rhyolite	May be mistaken for sandstone. Small crystals become visible only under a magnifying glass. Rhyolite is an igneous rock.

[11] Included only to compare the test results.

Two of these rocks, namely Chelmsford and Mason, were selected to be used in the later phases of testing for interface fracture properties because they represent one of the strongest and one of the weakest granites, respectively.

Testing of Rocks

Five rocks were tested: Chelmsford granite, "Old" Chelmsford granite[12], Deer Isle granite, Mason granite, and marble[13].

For each type of rock, two cylinders of 1.5 inch (3.81 cm) diameter were cored, cut to 3 inch (7.62 cm) length. The ends were ground smooth and parallel. The cylinders were tested uncapped[14] for compressive strength and Young's modulus. Two Instron extensometers were attached diametrically at midheight to measure the undisturbed longitudinal strain needed to calculate the Young's Modulus (see Fig. 6-2). The exact gage length, about 1 inch (2.54 cm) for the extensometers, was recorded for each test. Load and strain data were recorded by a Hewlett–Packard data acquisition system.[15] The equipment used was an open–loop hydraulic 6 0-kip (30 t) Baldwin machine. Each core was loaded three times until the load reached about 60% of the ultimate load, with data recorded from the second and third loop. A fourth loop without the extensometers attached was run until failure. The loading rate was 35 psi/sec (241 kPa/s). Except for the marble, whose fracture mode was 'Shear,' all specimens fractured explosively as 'Cones' (See Fig. 6-3. Curves for Young's modulus as functions of strain and stress were established from the test data.

The results of four test loops were averaged for each rock and are shown in Table 6.3. Since the Young's modulus is not a constant for geomaterials, values for E at different strain and stress levels must be reported. (Table 6.3.) The term $E^{t}_{50\%}$ refers to the Young's modulus at a stress level of 50% of the material's compressive strength measured as a tangent modulus. $E^{s}_{50\%}$ refers to the Young's modulus at a

[12]Stored in the stock room of MIT

[13]The marble and the "Old" Chelmsford were included for comparison only

[14]Capping with hydrostone is not recommended, because the lower stiffness of the capping material causes the specimen to be torn apart horizontally under tension.

[15]The load sensor of the machine was calibrated before the tests. The known calibration factors of the extensometers were verified using well defined aluminum cylinders, giving an error of 1.5%

stress level of 50% of the material's compressive strength taken as a secant modulus, and $E^t_{0.001}$ refers to the tangent Young's modulus at a strain of 0.001%.

Although "Old" Chelmsford and Chelmsford originate from the same quarry, their properties are slightly different for two reasons: First, the Old Chelmsford has a smaller grain size than the Chelmsford and was quarried many years ago. Over the years, granite forms clay at the grain boundaries, which, in turn, causes a loss of strength. Second, to ensure exact results, cylinders of geomaterials must be taken from three perpendicular directions, since these materials are highly anisotropic. Due to the limited amount of granite available, only one direction was tested. The properties of the granites as reported by Fletcher Granite Co., Inc. are given in Table 6.4 on page 104.

The large differences in the reported properties from the test results of up to 10,000 psi (69 MPa) can be explained by (1) too small a number of specimens tested, (2) an unrepresentative direction chosen for the cores, (3) flaws that might have been present in the relatively small specimens, and (4) not absolutely flat ends of the cores. However, the tests results compare well with those tests Lee performed [*Lee* (1993)] on "Old" Chelmsford and marble. Since the test data represents a lower boundary and the stress–strain behavior is not influenced by the absolute strength of the specimen, using the test data for Young's modulus is justified.

The critical energy release rate for Chelmsford in Mode I was determined as 17.5 J/m^2 [*Lee* (1993)].

After this investigation of different granites, Chelmsford and Mason granite were chosen to be used in tests on sandwiched beams. Although the granites represent a strong and a weak granite, respectively, no significant differences in the interface properties could be detected using full length sandwiched beams. Therefore, only Mason granite was used for the tests on compact sandwiched beams (Phase 4).

6.2.6 Preparation of Sandwiched Specimens

A step–by–step procedure follows for the manufacturing of sandwiched beam specimens. The procedure is the same for full-length and for compact sandwiched beam

specimens, with the only exceptions that the latter were made of Type III cement for 7-day strength and stored in a moist room at 90% humidity, while the full-length beams were made with Type I cement for 28-day strength and submerged in water for 28 days of curing. See Section 6.2.1.

Procedure

1. Cut aggregate slices 2 inches × 1 inches × 0.178 inches (5.08 cm × 2.54 cm × 0.452 cm) for small, 4 inches × 2 inches × 0.183 inches (10.16 cm × 5.08 cm × 0.464 cm) for medium, and 6 inches × 3 inches × 0.236 inches (15.24 cm × 7.62 cm × 0.601 cm) for large beams.[16]

2. Prepare the desired surface roughness: for smooth surfaces, the cuts made by the diamond saw are left as they are. For sandblasted surfaces, blast the specimen with glass bead blast medium at a pressure of 100 psi (670 kPa) until maximum roughness is achieved.[17] Sandblasting is also recommended for all specimens on the side of the aggregate layers that does not bear the epoxy. The flamed surface is taken as it is produced by Leamar Industries.[18] The different roughnesses shown in Figures 6-10 to 6-13 are photographed from the SEM.

3. Create artificial cracks with a/d=0.375: apply low viscosity epoxy resin (for a sharper crack tip) onto the aggregate surface and let it harden.

---

[16]See Section 6.2.1.

[17]About 60 seconds for a medium sized piece (5.08 cm × 10.16 cm) of Mason granite. The roughness achieved with sandblasting depends on the material. For Mason granite, a depth of approximately 0.5 mm and a wavelength equal to the grain size (3 mm) is accomplished. Quartzite crystals are harder than feldspar. Therefore, the composition, grain structure, and grain size determine the effect of sandblasting.

[18]Leamar Industries, 896 B Boston Post Road, Marlborough, MA, Tel. (508)-481-6844. By using a high temperature torch, spalling of the surf

ace occurs and a roughness with about 2 mm depth and 3 mm wavelength is produced.

4. Assemble acryl molds with spacers for "compact" sandwiched beams and without spacers for "full-length" beams.[19] See Figures 6-14 and 6-15. Insert the aggregate slices centered into the partitions of the mold. Mark the location of the crack.[20] Make sure the aggregate slices fit tightly so they will not move during the compacting of the concrete. [21]

5. Choose a concrete strength and its mix proportions from Section 6.2.3. Weigh cement, sieve and weigh dried sand, and measure silica fume and admixtures. For a set of "full-length" beams and four cylinders, 45 kg mortar are needed, whereas only 25 kg are necessary for a set of "compact" beams and cylinders. It is practical to mix the water with the silica fume, the superplasticizer, and other possible admixtures. Mix the mortar according to ASTM-C192-90a. Place the sand in the mixing bowl, then add the cement all at once. Mix for 60 seconds. Then gradually add the liquid. After all the liquid is added, mix it for 3 minutes. Stop at intervals to scrape the mortar from the bottom and the wall. Mix for another 2 minutes.[22]

6. In the meantime, the molds must be greased. It is important to do this just prior to pouring the mortar to prevent oil from getting onto the aggregate surfaces. Apply the grease [23] sparingly, leaving a 1 cm strip on each side of the aggregate slices free of grease.

7. Pour the mortar into one partition at a time. Rub the mortar onto the surfaces using a rubber glove and then immediately fill up the mold. Thoroughly compact the mortar with a steel rod (5 mm diam-

[19]With spacers, twice the amount of specimen was produced at a time: 8 small, 4 medium, and 4 large.

[20]This is important for the later testing.

[21]Each aggregate slice was fitted individually to its place in the mold using a diamond saw. In addition, exopy resin was applied at the faces that are in contact with the mold. With gradually grinding off that epoxy resin, each slice could be fitted perfectly tight.

[22]The mixer was of the type with a fixed mixing bowl and a vertical, off-center mixing paddle which rotates about the vertical axes of both itself and the mixing bowl.

[23]For example, Formshield.

eter). When all partitions are filled, vibrate the mold for 1 minute while making sure that the aggregate slices do not move. A set of small specimens is shown in Figure 6-16. Immediately cover the mold with plastic as tight as possible to reduce the loss of water through evaporation. Store the molds where no vibrations may reach them.

8. I recommend demolding only after 36 hours have passed. The demolding process is crucial for proper test results. Any shocks that may not actually fracture the interface might still create microcracks which in turn will negatively influence the test result.[24] Full-length beams were submerged in lime–saturated water for 28 days, whereas compact beams were stored in a moist–room at 95% humidity for 7 days. Storage in a moist–room is preferable. Be sure that each specimen is marked properly with date, aggregate, mix, and location of the crack within the specimen. A comparison of all three sizes of compact specimens is shown in Figure 6-17.

6.3 Testing of Sandwiched Specimens

The use of the so–called compact sandwiched beam specimens, or simply compact specimens, is recommended (see Section 6.2.1). A total of 91 full–length sandwiched beams in three different sizes was tested in either pure Mode I (opening mode) or mixed mode with a loading angle of about 45 degrees. For the last test series (Phase 4), a total of 140 compact sandwiched specimens were tested in three sizes, three different aggregate roughnesses (smooth, sandblasted, and flamed) and three loading angles (0, 30, and 60 degrees). See Section 7.1. It should be noted that only the fracture load of the specimens need to be recorded. No displacements were measured.

[24] To reduce this risk, the compact sandwiched beam specimen was developed.

6.3.1 Testing Equipment

Machines

For the testing of small compact beams in pure opening mode and mixed mode with $\psi = 30°$, a 1 kip (5 kN) Instron machine was used. (Fig. 6-7.) The machine is of the screw–type and can be load, deflection, or strain controlled. Other feedback can be specified.

For all other beam testing, a 60 kip (30 t) Baldwin machine was used (Figure 6-8). This machine is hydraulic and of the open loop type. Three different load ranges can be set, 6000 lb., 30,000 lb., and 60,000 lb. Tests were performed with the lowest setting of 6,000 lb. (27 kN). The loading rate is controlled manually by means of sensitive needle valves. This machine was also used to test the rock cylinders for Young's modulus and compressive strength and to test the mortar cylinders for Young's modulus.

A 200 kip (890 kN) Baldwin machine was used to test the mortar cylinders for compressive strength as described in Section 6.2.4 on page 91. This machine is also hydraulic but has closed loop control by means of an IBM-Computer.

Accessories

To measure the undisturbed longitudinal strain of the rock cylinders, two Instron extensometers with 1 inch (2.54 cm) gage length were used. The extensometers are shown in Fig. 6-2 on page 105. The calibration constants were verified using an aluminum cylinder of known Young's modulus with an error of 1%.

Linear Variable Differential Transformers (LVDT) were used to measure the longitudinal strain of mortar cylinders. LVDTs are small, cylindrical devices with a diameter of 9.5 mm (3/8 inch) and a length of 25.4 mm (1 inch). The voltage range is ± 5 Volts. When the magnetic core is displaced inside the LVDT, a change in voltage is produced that is linearly proportional to that displacement. Therefore, it is possible to find a unique calibration factor for each LVDT. This was done prior to each test series using a micrometer and fitting the readings with a least square analysis.

The slope of the regression line is the calibration constant. It is usually a number in mm/(V V) and gives the displacement between two positions when multiplied with the difference of the two voltage readings at these positions and the driving voltage of the LVDTs, usually 5 Volts or less.

Data Acquisition System

A Hewlett–Packard data acquisition system that is linked to a Hyundai computer was used to record the data from the load sensors, the displacement transducers, or the LVDTs for tests of Young's modulus of the materials. With this setup, 40 channels are available. However, no more than 5 were in use for the test described in Section 6.3 with the 60 kip (30 t) BALDWIN–Machine: two channels for the driving voltages of the pressure sensor and the LVDTs, one channel for the pressure reading, and two channels for the LVDTs or extensometers. The data recording rate was 1 second.

Scanning Electron Microscope

A scanning electron microscope (SEM) called "Strereoscan 240," manufactured by Cambridge Instruments, Ltd., Cambridge, Great Britain, was used to investigate the microstructure of the materials and the fractured surfaces. This microscope features secondary electron, backscattered electron, and X–ray diffraction analysis techniques, as used for Figures 7-40 to 7-42.

6.3.2 Experimental Parameters

The factors that influence the properties of the aggregate/mortar interface include:

- Properties of the mortar (porosity, bleeding, Young's modulus, silica fume)
- Properties of the aggregate (type, Young's modulus, adsorption, brittleness)
- Overall size of the specimen, the loading angle (shear vs. opening)
- Aggregate surface roughness
- Loading rate

- Relative crack length and type of the artificial crack (sharp vs. blunt)
- Testing machine (stiffness, data recording rate, sensitivity)
- Environmental conditions (temperature, humidity)
- Age of the specimens
- Curing of the specimens.

For the tests reported in this study, all parameters were held constant except the following:

1. **Size of the specimens in a range of 1:3**
2. **Loading angle (shear vs. opening)**
3. **Roughness of interface**
4. **Type of aggregate interlayer**

6.3.3 Procedure for Testing of Sandwiched Beams

This section gives a step–by-step procedure for the testing of full–length Sandwiched Beams and Compact Sandwiched Beams.

1. Carefully remove the specimens from the storage. Prevent the interfacial region from drying out (by using, for instance, plastic wrap).
2. For compact specimens, aluminum or concrete beams [25] need to be glued to the specimen so that beams of full length are obtained. Carefully prepare the surfaces. Sandblasting is recommended. Make sure that the surfaces are dry before the epoxy resin is applied. I recommend to use moisture insensitive, low viscosity epoxy resin with high ultimate strength. Ensure proper alignment of the sandwiched section with the attached pieces. Allow sufficient time for the epoxy

[25] I used previously tested full-length beams. They were precisely cut with a diamond saw to ensure proper alignment. Specifically cast HSC beams of specimen dimensions can also be used.

to harden (approximately 8 hours). Figure 6-18 shows glued compact beams.

3. Mark the specimen with the locations of the bearings and the top loading arrangement. Measure all distances from the face of the crack. Test the specimen so that in mixed mode the crack can kink into the mortar without having to fracture the aggregate, hence, the crack is on the left side of the aggregate slice when the setup shown in Fig. 6-4 is used.

4. Prepare the test–setup as shown in Fig. 6-4. Carefully align the specimen on the bearings on the loading machine table. Put the four–point bending arrangement on top of the specimen, exactly at the marked locations. Make sure that the line of the load meets with the marked line. Any errors will have a significant influence on the test result.

5. Set the loading rate for the small beams in a deflection controlled test to 0.0762 mm/min (0.003 in/min). It should then take about five minutes until failure. In a load controlled test set the loading speed for the medium and large beams so that they also fracture after 5 minutes, about 0.18 mm/min for medium and 0.3 mm/min for large specimens. Record the loading rate, the time until failure, the peak load, the weight of the top loading arrangement, the weight of the beam, and the failure mode. Note that no deflections need to be measured.

6. Tests for which the onset of crack propagation was at the artificial crack tip are valid. For mixed mode fracture, the crack usually travels along the interface and eventually kinks into the mortar. It is important to observe the same failure mode for all specimens of different size.

Mix Proportions and Compressive Strengths for Mortars								
No.	W/(C+SF)	S/C	Type	SF/C [%]	HRWR/C [%]	Work-ability	7-day [MPa]	28-day [MPa]
1	0.500	2.0	I	0.0	0.0	good	—	42.5
2	0.350	2.0	I	5.0	1.0	good	—	58.5
3	**0.280**	**2.0**	**I**	**10.0**	**2.0**	**good**	**67.6**	**83.5**
4	0.220	2.0	I	20.0	3.0	fair	78.5	96.5
5	0.400	2.0	III	20.0	1.0	excel.	62.4	—
6	0.350	2.0	III	10.0	1.0	fair	69.8	—
7	0.280	2.0	III	10.0	2.0	fair	82.6	—
8	**0.283**	**2.0**	**III**	**10.4**	**2.2**	**excel.**	**81.1**	—
Mixes No. 3 and 8 were used to produce the 28-day and 7-day mortar for sandwiched beams, respectively.								

Table 6.2: Mix proportions and compressive strengths of high-strength mortars

Material	Compression		$E^t_{50\%}$		$E^s_{50\%}$		$E^t_{0.001}$	
	MPa	psi	GPa	10^6psi	GPa	10^6psi	GPa	10^6psi
Marble	61.9	8980	56.2	8.15	55.5	8.05	56.8	8.25
Old Chelmsford	149.9	21,735	58.0	8.41	46.4	6.73	47.7	6.92
Chelmsford	166.8	24,185	55.5	8.05	44.5	6.45	48.2	6.99
Mason	123.4	17,898	42.2	6.12	27.8	4.04	26.4	3.83
Deer Isle	153.0	22,193	62.8	9.12	53.5	7.76	60.7	8.80

Table 6.3: Compressive strengths and Young's moduli of different rocks

Material*	Compression		Mod. of Rupture		Adsorption	Abrasion
	ASTM C170-50		ASTM C99-52		ASTM C97-47	ASTM C241-51
	MPa	psi	MPa	psi	%	
Chelmsford	259.5	37,633	16.2	2,355	0.325	86.0
Mason	193.7	28,090	14.2	2,059	0.300	69.3
*No data was available for Deer Isle granite						

Table 6.4: Properties of granites as reported by Fletcher Granite Co., Inc.

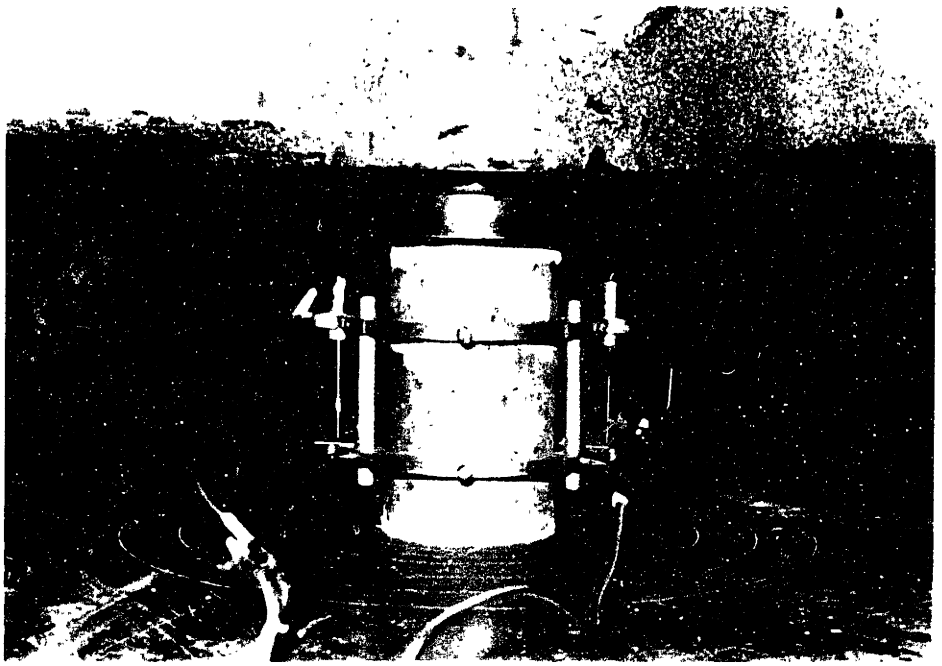

Figure 6-1. Setup for determination of Young's modulus of mortar cylinders using a yoke and two diametrically attached LVDTs

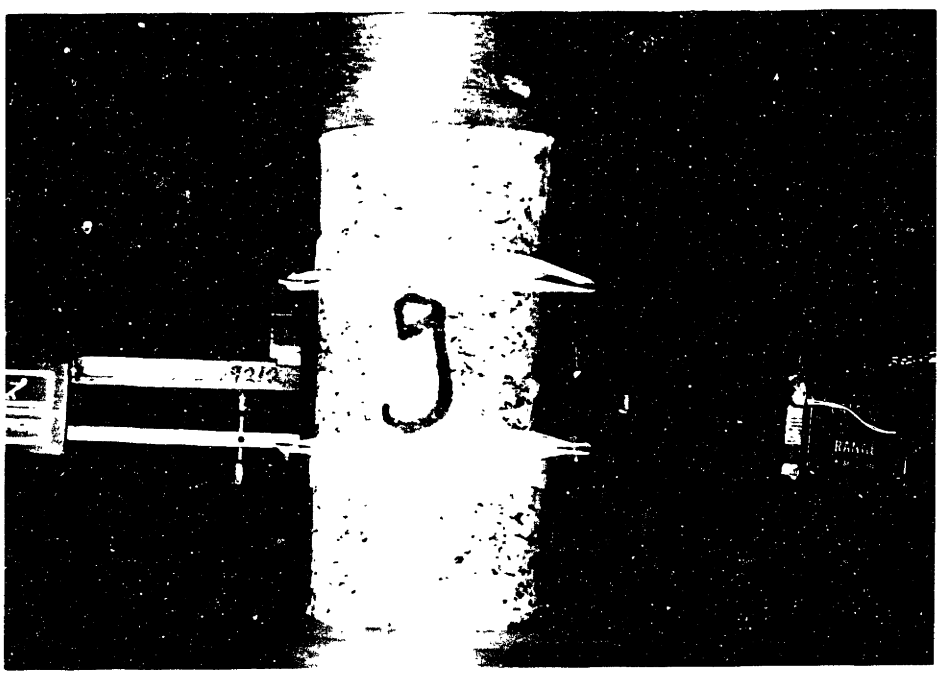

Figure 6-2. Setup for determination of Young's modulus of rock cylinders using two diametrically attached extensometers

Figure 6-3: Typical cones and pulverized remains after explosive failure of a granite cylinder (Mason granite)

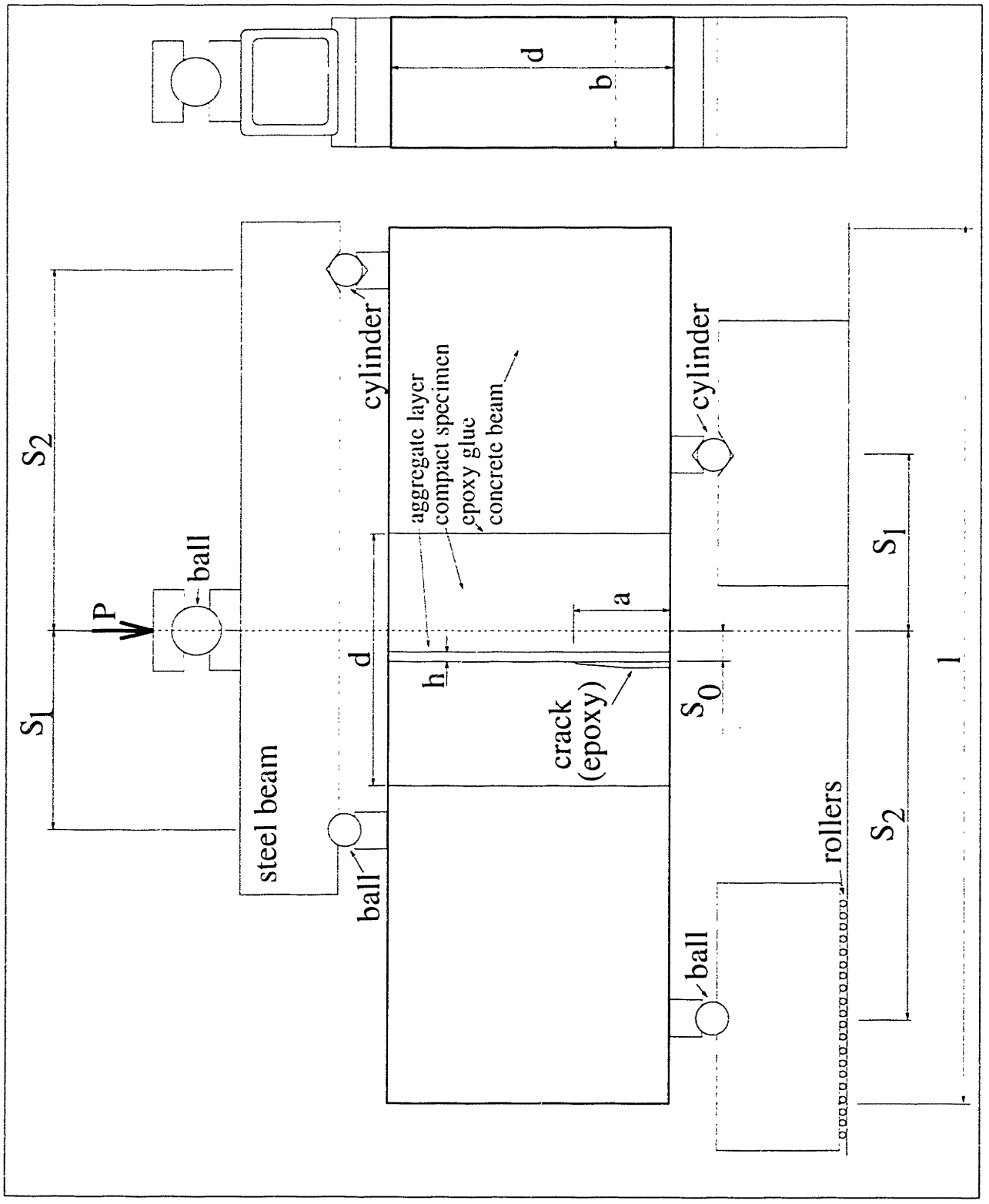

Figure 6-4: Setup for four-point bending test

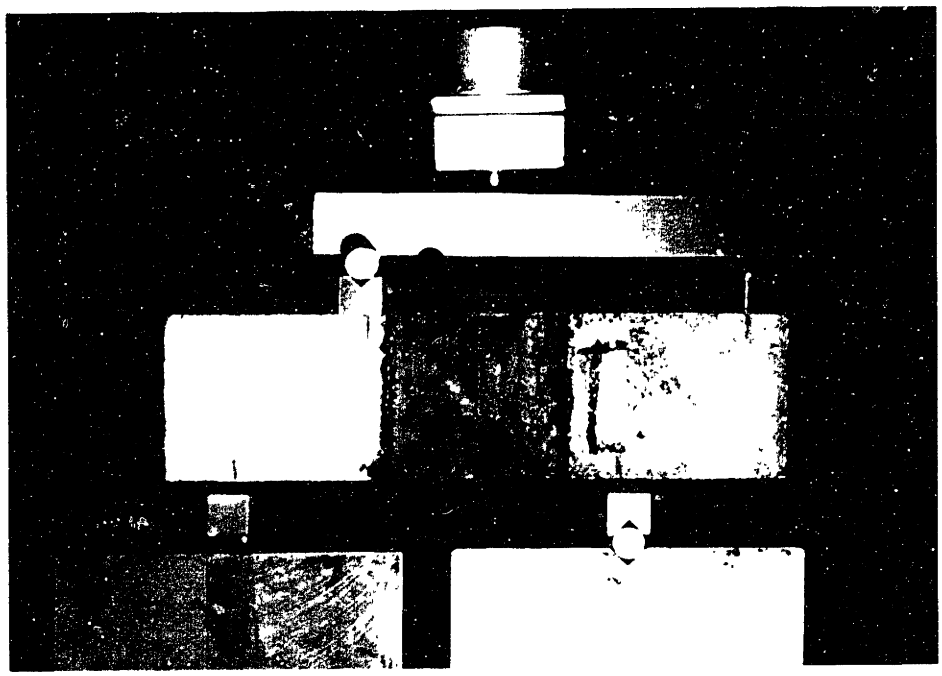

Figure 6-5 Test set up for a small compact sandwiched beam specimen in mixed mode ($\psi = 63^\circ$)

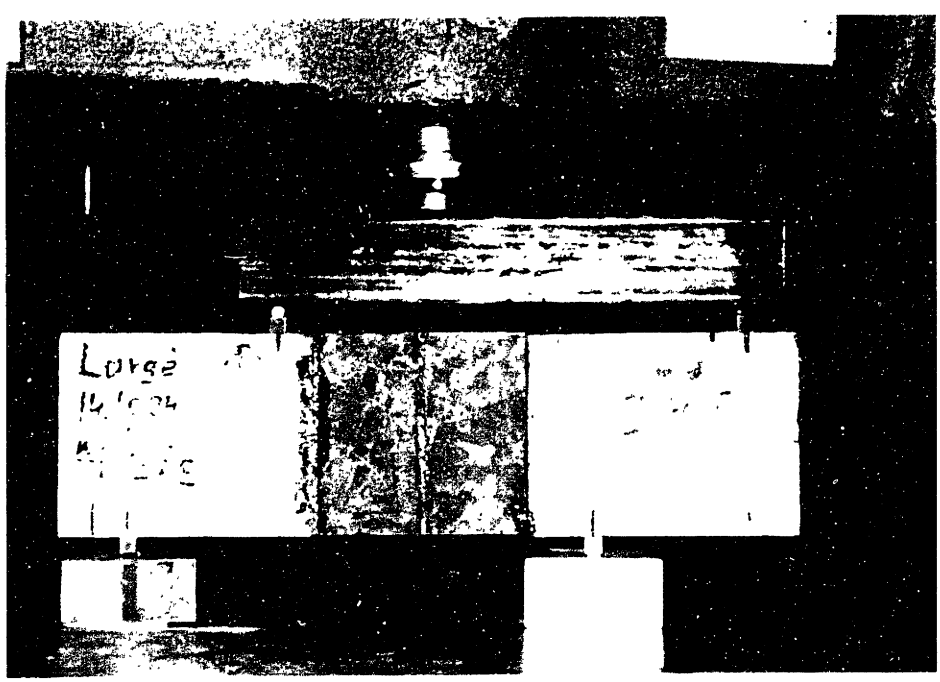

Figure 6-6 Test set up for a large compact sandwiched beam specimen in mixed mode ($\psi = 63^\circ$)

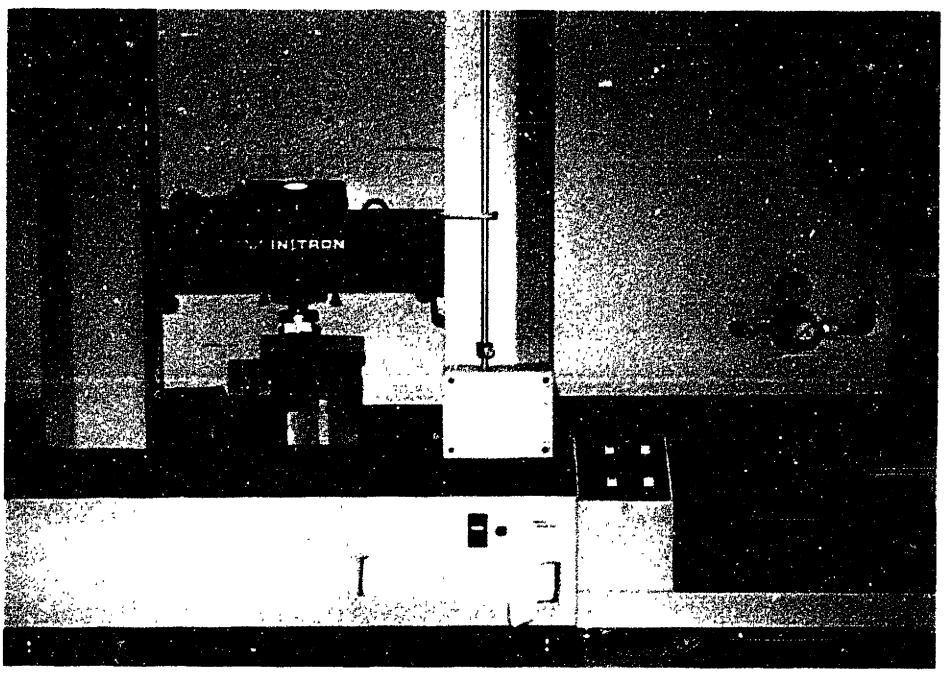

Figure 6-7: 5 kN Instron machine and control panel

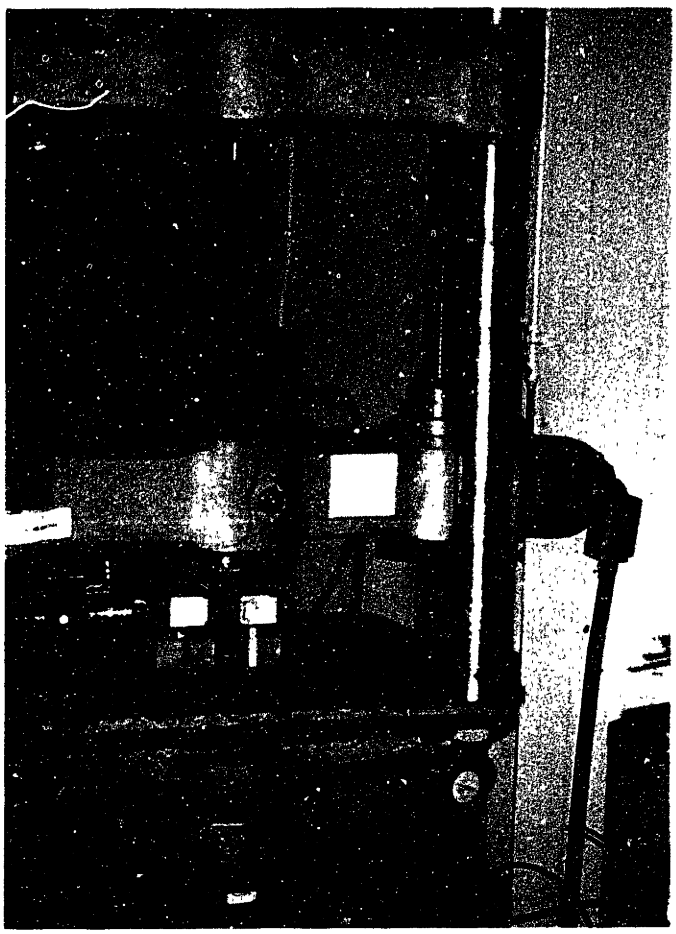

Figure 6-8: 27 kN Baldwin machine

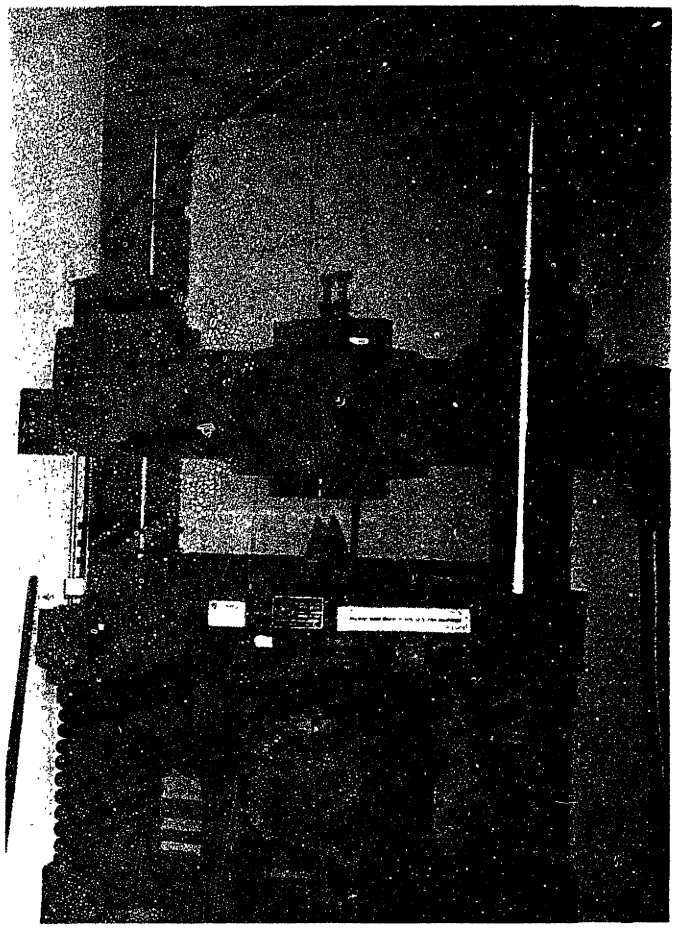

Figure 6-9: 800 kN Baldwin machine

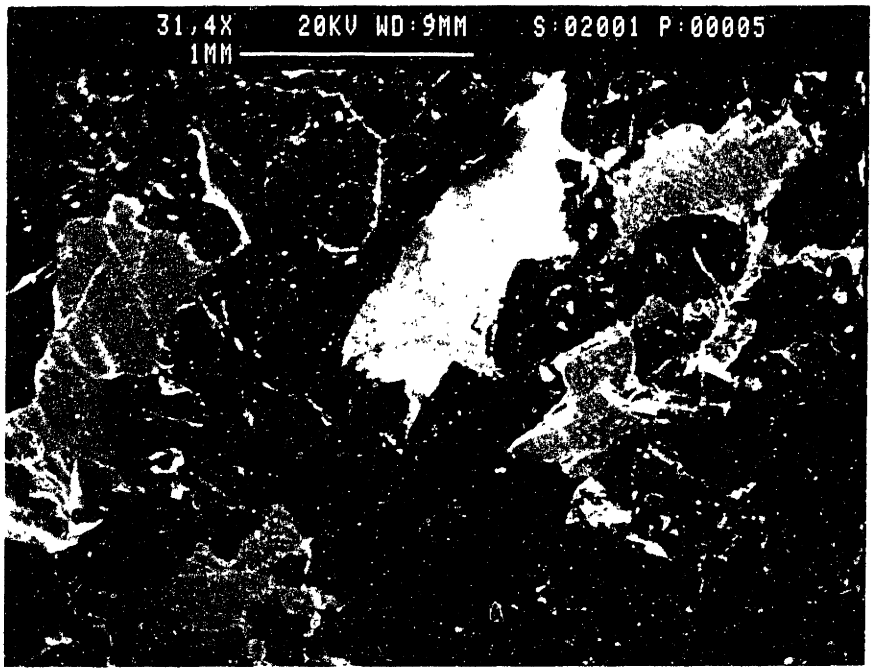

Figure 6-10: Polished sample of Mason granite. The crystal structure can easily be seen.

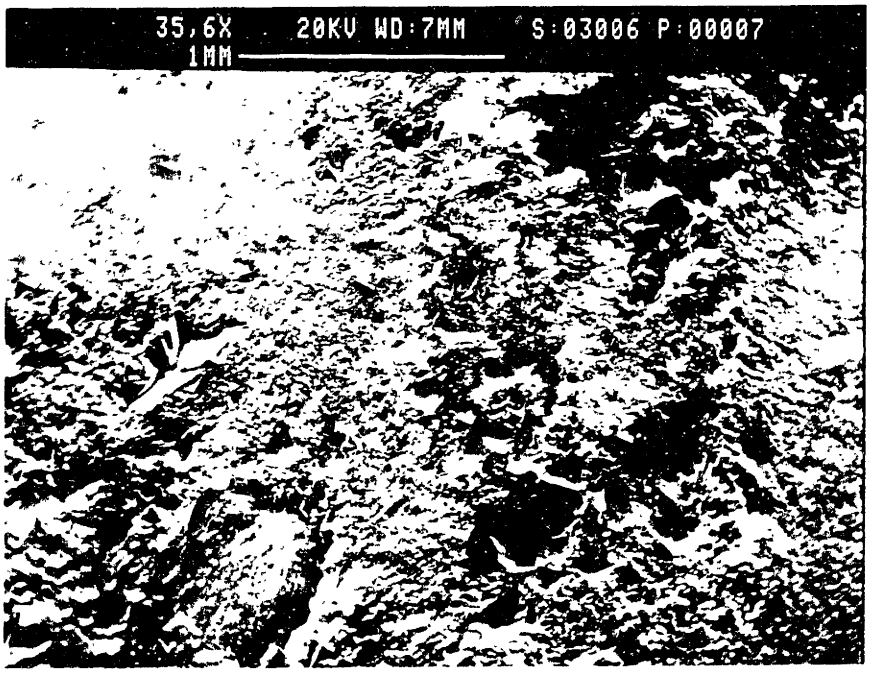

Figure 6-11: Smooth sample of Mason granite as produced by the cut of a diamond saw

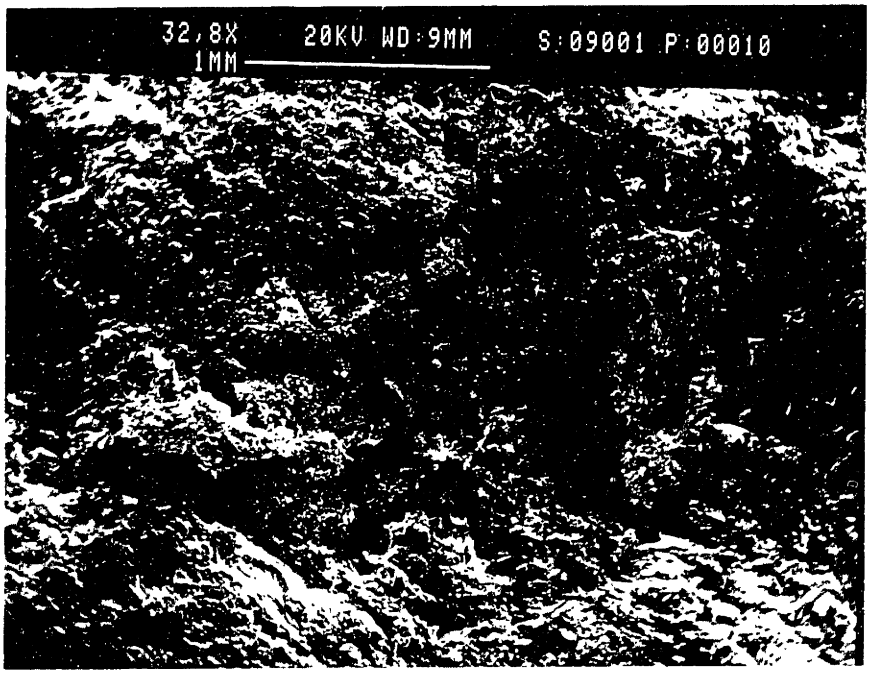

Figure 6-12: Sandblasted sample of Mason granite

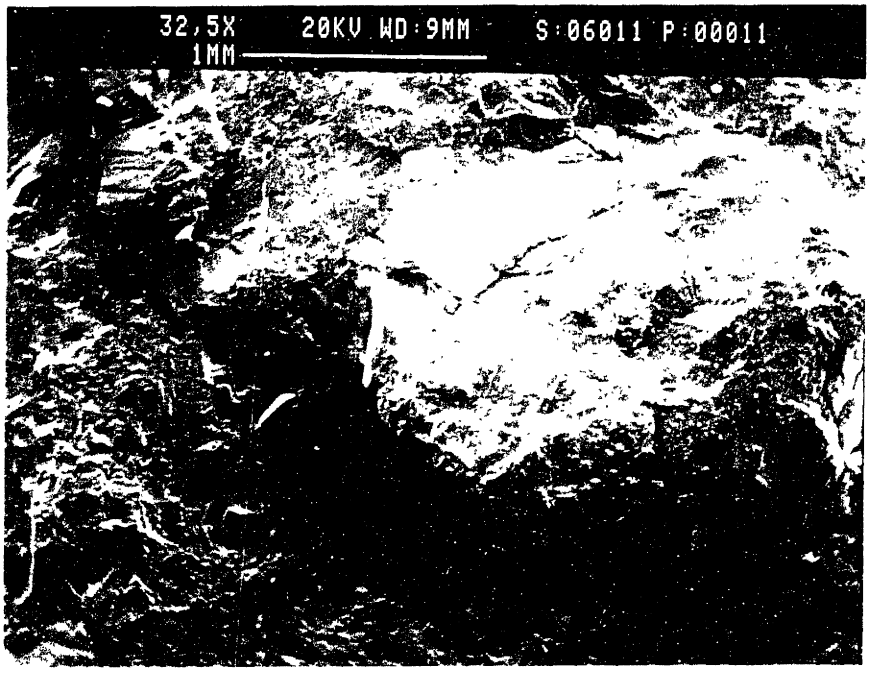

Figure 6-13: Flamed sample of Mason granite as produced by Leamar Industries (Sec. 2)

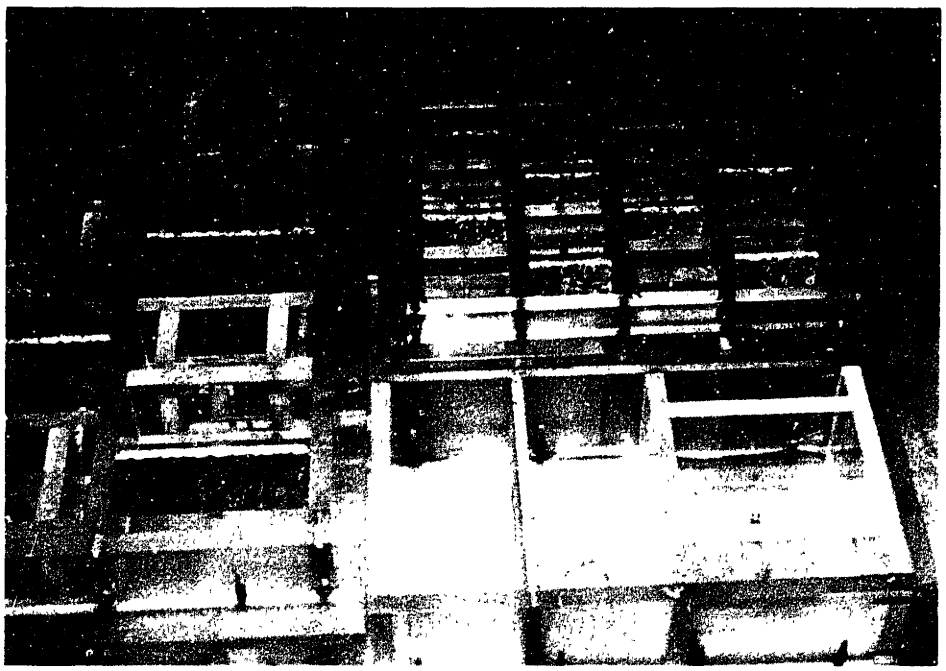

Figure 6-14. All three molds for the different sizes of compact specimens: large mold at the bottom, small mold right on top, medium mold left at top. The slices of Mason granite bearing the epoxy as an artificial crack have been inserted

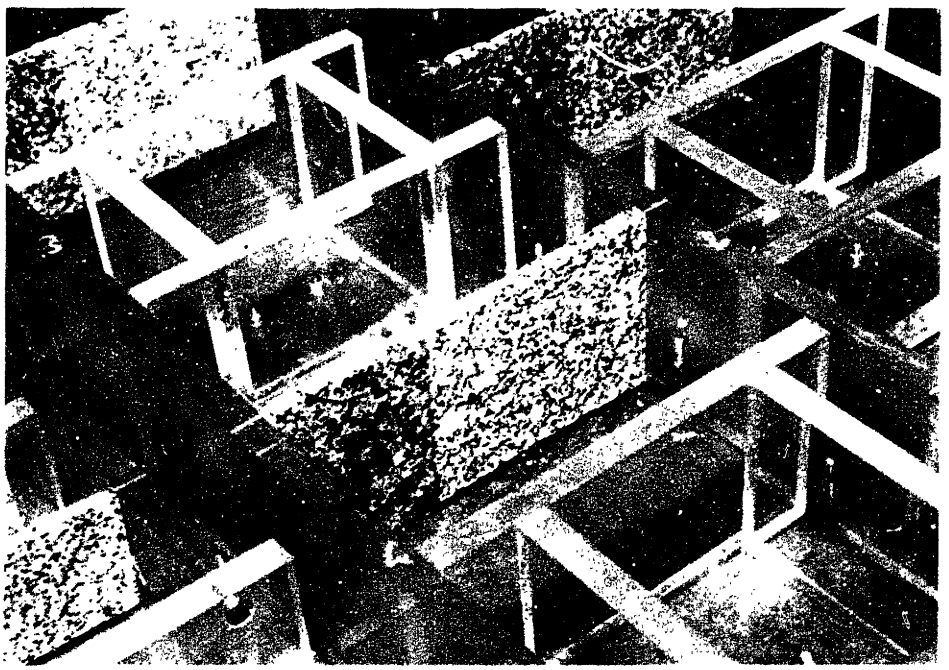

Figure 6-15: Detail of acryl mold for large specimen showing the aggregate slice (Mason granite) bearing the epoxy and the acryl spacers to adjacent specimens. Note that the arrangement reduces the influence of heat of hydration.

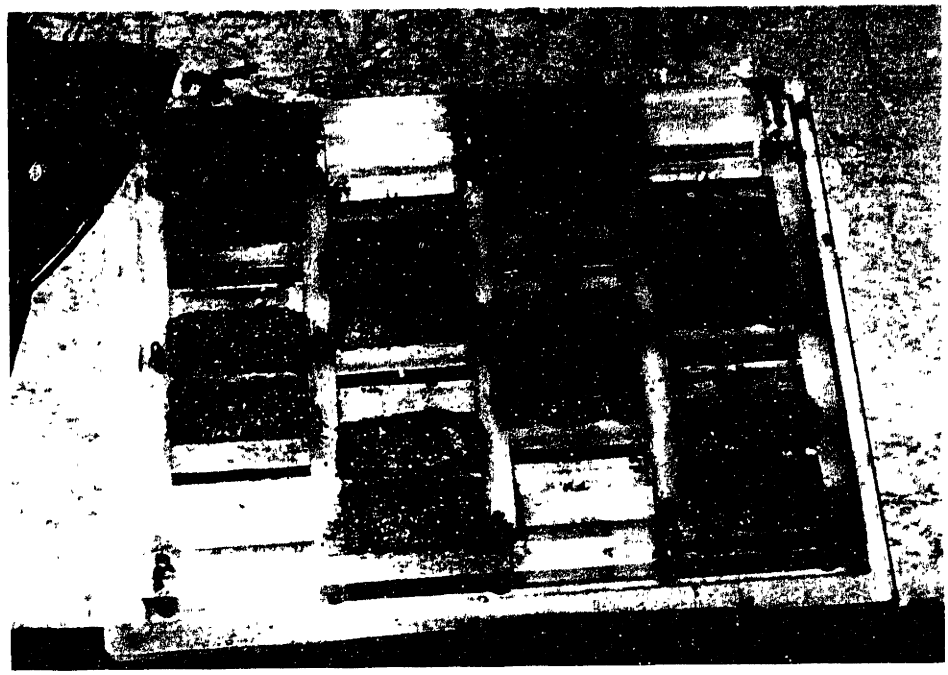

Figure 6-16. A full set of small compact specimens after casting.

Figure 6-17. Comparision of all three sizes of compact beam specimens before being glued to mortar beams. The large specimen measures 15.24 cm in height and width. The bright residue on the mortar is lime which was contained in the curing water inside the plastic cover.

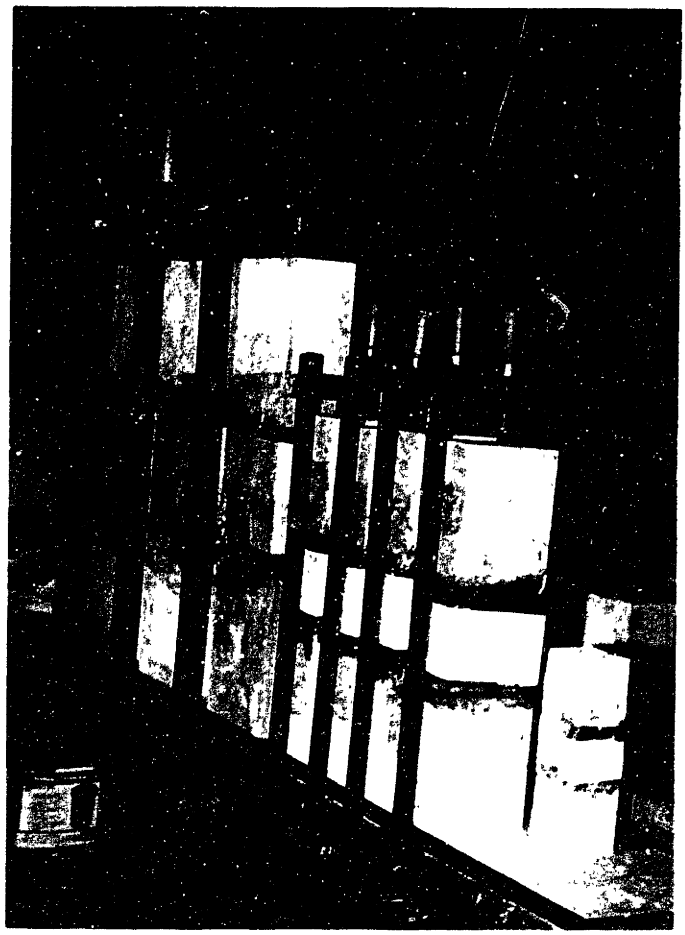

Figure 6-18: Large, medium, and two small specimens after they had been glued to previously cast high-strength mortar beams, kept moist and wrapped and wrapped in plastic

Chapter 7

Results of Sandwiched Beam Testing

This chapter gives the procedures for the calculation of fracture and size effect data. It summarizes the test data from tests on full–length sandwiched beam specimens and compact sandwiched specimens.

In the first part, the test results are presented separately for interface fracture parameters and size effect. The data obtained from compact sandwiched specimens are the most valuable. The conclusions presented in Chapter 8 and the analysis of the size effect, which is presented in part two of this chapter, are based on the tests in the final test series (Phase 4), which exclusively used compact sandwich specimens.

A discussion of the test results is presented in the third part of this chapter, followed by an examination of the problems involved in the measurement of interface properties. In the last two parts, the results of the microscopical investigation of the materials and interfaces and recommendations for the material design of high strength concrete are presented.

7.1 Overview of the Performed Tests

Phase	Specimen	Sizes	Loading Angles	Roughnesses	Total
1	full–length	1	0°	4	25
2	full–length	3	0°, 45°	2	66
4	compact	3	0°, 30°, 60°	3	140
The results of the last test series are the most useful ones. The size effect data was derived from those tests only.					

7.2 Interface Fracture Parameters

7.2.1 Procedure for Calculation of Interface Fracture Properties

This section presents a procedure for the calculation of the interface fracture properties, such as fracture toughness $K_{1,2}$ and fracture energy release rate G_f. The procedure is reported for the four–point bending mixed mode test. For the four–point Mode I specimen and the three–point mixed mode specimen, the process works similarly. (See Chapter 5 for reference.)

Input Data

1. Peak load P [1]
2. Geometry of loading arrangement: S_1, S_2, and S_0 [2]
3. Geometry of specimen: width b, and height d [3]
4. Stress intensity coefficients $f_b(a/d)$ and $f_s(a/d)$ [4]

[1] Computed from the measured load, the equivalent load from the beam's own weight, and the weight of the top loading arrangement. However, the weight of the top loading arrangement and the beam itself has less than 1% influence on the peak load in Mode I and was, therefore, neglected in higher loading angles.

[2] See Section 6.2.1 on page 84 and Section 6.2.1 on page 83.

[3] See Section 6.2.1 on page 83.

[4] from Table 4.2 on page 62. $f_b(a/d) = 7.835$ and $f_s(a/d) = 1.1985$ for $(a/d) = 0.375$ (interpolated).

Parameters of Material Combinations											
Mat. 1	Mat. 2	E_1 [GPa]	E_2 [GPa]	ν_1 —	ν_2 —	μ_1 [GPa]	μ_2 [GPa]	α —	β —	ϵ —	ω °
M(3)–28	Mason	35.2	42.2	0.2	0.16	14.6	18.2	-0.08	-0.02	0.005	0.70
M(3)–28	Chelm	35.2	55.5	0.2	0.16	14.6	23.9	-0.24	-0.11	0.005	2.27
M(8)–7	Mason	33.3	42.2	0.2	0.16	13.9	18.2	-0.11	-0.03	0.008	1.23
M(3)-28 refers to Mortar Mix No. 3 in Table 6.2 on page 103 M(8)-7 refers to Mortar Mix No. 8 in Table 6.2 on page 103 See also Chapter 4 for reference											

Table 7.1: Characteristics of the materials combinations used in the tests

5. Young's modulus of mortar E_1 [5]
6. Young's modulus of aggregate E_2 [6]
7. Poisson's ratios for mortar and rock [7]
8. Characteristic length $\hat{L}$ [8]
9. Thickness of aggregate layer h [9]

Procedure

Table 7.2 summarizes the procedure for the calculation of interface fracture data from the four–point bending mixed mode specimen.[10] The procedure can conveniently be used with a spreadsheet program, for example Xess. See also Chapter 3 for reference.

[5]Preferably according to ASTM-C469-87a. See Section 6.2.4 on page 91.
[6]Here, the 50% stress–level tangent modulus was used. See Section 6.2.5 on page 94.
[7]These values were estimated. See Table 7.1 on page 119.
[8]See Section 3.1.1. Generally unimportant, since $\epsilon = 0$ for the calculations. Can be set equal to aggregate layer thickness.
[9]See Section 6.2.6 on page 96. Again, h is unimportant if $\epsilon = 0$.
[10]See Section 4.3 on page 61

Procedure of Calculations of Fracture Data				
Step	**Description**	**Equation**	**Unit**	**Ex.**
1	Peak load in lb.	P	lb	2400
2	Peak load in N	P=P[lb]*4.448	N	10675
3	Support reaction	$P_1 = P * S_2/(S_1 + S_2)$	N	8006
4	Support reaction	$P_2 = P * S_1/(S_1 + S_2)$	N	2669
5	Shear force	$Q = P_1 - P_2$	N	5337
6	Moment	$M = P_2(S_2 - S_0) - P_1(S_1 - S_0)$	Nm	90.38
7	App. frac. toughn.	$K_I = M/(BW^{3/2}) * f_b(a/W)$	MPa$\sqrt{\text{m}}$	0.43
8	App. frac. toughn.	$K_{II} = Q/(BW^{1/2}) * f_s(a/W)$	MPa$\sqrt{\text{m}}$	0.39
9	Part o. phase ang.	$\phi = \tan^{-1}(K_{II}/K_I)$	°	42.54
10	Eff. mort. E mod.	$\bar{E}_1 = E_1/(1 - \nu_1^2)$	GPa	34.73
11	Eff. rock E mod.	$\bar{E}_2 = E_2/(1 - \nu_2^2)$	GPa	43.31
12	Dundurs' par.	$\alpha = (\bar{E}_1 - \bar{E}_2)/(\bar{E}_1 + \bar{E}_2)$	—	-0.109
13	Shear modulus 1	$\mu_1 = E_1/(2(1 + \nu_1))$	GPa	13.89
14	Shear modulus 2	$\mu_2 = E_2/(2(1 + \nu_2))$	GPa	18.19
15	Dundurs' par.*	β see Eqn. 3.1 on page 51	—	-0.027
16	Oscillation ind.	$\epsilon = 1/(2\pi)\ln((1 - \beta)/(1 + \beta))$	—	0.008
17	Shift	ω from Table 4.1 on page 59	°	1.238
18	Phase angle	$\hat{\psi} = \phi + \omega + \epsilon \ln(\hat{L}/h)$	°	43.78
19	Stress Int.	$\mathrm{K}_1 = \sqrt{1 - \alpha}(\mathrm{K_I}\cos\omega - \mathrm{K_{II}}\sin\omega)$	MPa$\sqrt{\text{m}}$	0.44
20	Stress Int.	$\mathrm{K}_2 = \sqrt{1 - \alpha}(\mathrm{K_{II}}\cos\omega - \mathrm{K_I}\sin\omega)$	MPa$\sqrt{\text{m}}$	0.40
21	Energy rel. rate	$G = (K_I^2 + K_{II}^2)/\bar{E}_1$	J/m^2	9.82
*Note that β and,therefore ϵ are considered 0 for the calculation of $\hat{\psi}$, K_1, and K_2				

Table 7.2: Procedure for calculation of interfacial parameters for four–point shear specimen

7.2.2 Results of First Test Series

These first tests were performed to show the reproducibility of the tests performed by Lee [*Lee* (1993)] and to get an idea of the influence of aggregate surface roughness on interface fracture parameters. The specimen used was the full length sandwiched beam specimen. The tests were performed in pure Mode I.

Table 7.3 shows the results of these tests. For the procedure of the calculations, see Section 7.2.1 on page 119. The smooth, sandblasted and flamed surfaces were prepared as described in Section 1 on page 96. The roughness of the wire cut is somewhere between that of sandblasted and flamed surfaces and is produced by the wire saw in the quarry of Fletcher Granite & Co. The results are discussed in Section 7.4.

Rock	**Surface**	$\mathbf{K_{IC}}$ [MPa $\sqrt{\text{m}}$]
Chelmsford	Smooth	**0.32**
Chelmsford	Sandblasted	**0.21**
Chelmsford	Wire cut	**0.30**
Chelmsford	Flamed	**0.31**
Mason	Smooth	**0.32**
Mason	Sandblasted	**0.16**
Mason	Wire cut	**0.24**

Table 7.3: Average of results of Mode I Tests on Sandwiched Beams with different surface roughnesses, 28–day 83MPa mortar

7.2.3 Results of Second Test Series

The second test series was performed on full–length sandwiched specimens of three different sizes and includes, for this specimen, all tests in mixed mode and all tests in Mode I except for those done in the first test series. The results show a large scatter, which could be reduced only in the final test series by utilizing the specifically developed compact sandwiched specimen.

The testing parameters for this test series were specimen size, loading angle, aggregate material, and surface roughness. Additionally, the geometry of the four–point loading arrangement for mixed mode testing was varied once to find a useful geometry for further tests. Therefore, the experiments are reported together with either "old" or "new" geometry, referring to the initial and the improved loading arrangement, respectively. On page 85, the details of both, "old" and "new", geometry are reported.

Mixed mode testing for this series was performed with an approximate loading angle of 45 degrees only. The ratios of the specimen sizes were 1:2:3. (Section 6.2.1 on page 6.2.1.) The aggregates used were Mason granite and Chelmsford granite. The surfaces were either smooth or sandblasted. The artificial crack was created by coating a part of the aggregate layer with epoxy resin. The relative crack length was $a/d = 0.375$.

The results are reported in Tables 7.4 to 7.7. They are marked with either valid or invalid, indicating tests as invalid for which there was concrete failure at the bearings, fracture on the opposite side of the crack face, or the specimen was pre–cracked due to handling, storage, shrinkage or thermal stresses.

Interface Fracture Data of Mode I Four-Point Bend Tests					
Load [N]	K_I [MPa$\sqrt{m}$]	K_1 [MPa$\sqrt{m}$]	$\hat{\psi}$ [°]	G_f [J/m^2]	valid?
Small Beams, Mason, smooth:					
661	0.350	0.368	0.70	3.469	√
175	0.099	0.104	0.70	0.278	no
516	0.275	0.289	0.70	2.146	√
213	0.119	0.125	0.70	0.400	no
75	0.047	0.049	0.70	0.063	no
86	0.053	0.056	0.70	0.079	no
1260	0.660	0.695	0.70	12.30	√
140	0.081	0.085	0.70	0.187	no
242	0.133	0.140	0.70	0.505	no
212	0.118	0.124	0.70	0.395	no
1232	0.645	0.645	0.70	11.768	√
145	0.083	0.087	0.70	0.197	no
Small Beams, Chelmsford, sandblasted:					
338	0.183	0.203	2.27	0.955	√
390	0.210	0.234	2.27	1.248	√
4	0.010	0.011	2.27	0.003	no
118	0.069	0.077	2.27	0.137	no
599	0.318	0.354	2.27	2.868	√
78	0.049	0.054	2.27	0.068	no
Medium Beams, Mason, smooth:					
617	0.123	0.129	0.70	0.410	√
743	0.146	0.154	0.70	0.579	√
Large Beams, Mason, smooth:					
1223	0.127	0.133	0.70	0.495	√
6672	0.669	0.704	0.70	13.694	√

Table 7.4: Test results in Mode I on Full–Length Sandwiched Specimens

Interface Fracture Data of Mixed Mode Four-Point Bend Tests							
Load [N]	K_I [MPa$\sqrt{m}$]	K_{II} [MPa$\sqrt{m}$]	K_1 [MPa$\sqrt{m}$]	K_2 [MPa$\sqrt{m}$]	$\hat{\psi}$ [°]	G_f [J/m^2]	valid?
Small Beams, Mason, smooth: **"Old" Geometry**							
5804	0.245	0.225	0.253	0.231	43.7	3.127	√
3558	0.150	0.138	0.155	0.142	43.7	1.175	no
10230	0.432	0.396	0.446	0.407	43.7	9.716	√
4981	0.210	0.193	0.216	0.198	43.7	2.304	√
8228	0.347	0.319	0.358	0.328	43.7	6.286	√
8451	0.357	0.327	0.368	0.336	43.7	6.630	√
6494	0.274	0.251	0.283	0.258	43.7	3.915	√
8139	0.343	0.315	0.354	0.324	43.7	6.150	√
Medium Beams, Chelmsford, smooth: **"Old" Geometry**							
41722	0.623	0.572	0.668	0.609	44.8	19.555	√
47682	0.712	0.653	0.763	0.695	44.8	25.542	√
29912	0.432	0.396	0.463	0.421	44.8	9.888	√
15390	0.229	0.211	0.245	0.225	44.8	2.802	√
Large Beams, Chelmsford, smooth: **"Old" Geometry**							
37808	0.307	0.282	0.329	0.300	44.8	5.321	√
82288	0.669	0.614	0.717	0.653	44.8	25.204	√
107864	0.876	0.805	0.939	0.857	44.8	43.307	√
103860	0.844	0.775	0.905	0.825	44.8	40.152	√

Table 7.5: Results of mixed mode tests on Full–Length Sandwiched Beams with the "old" geometry of the four–point shear test setup

Interface Fracture Data of Mixed Mode Four-Point Bend Tests							
Load [N]	K_I [MPa$\sqrt{m}$]	K_{II} [MPa$\sqrt{m}$]	K_1 [MPa$\sqrt{m}$]	K_2 [MPa$\sqrt{m}$]	$\hat{\psi}$ [°]	G_f [J/m^2]	valid?
Small Beams, Mason, smooth: **"New" Geometry**							
2090	0.238	0.218	0.246	0.224	43.7	2.957	√
2935	0.334	0.307	0.345	0.316	43.7	5.832	√
2401	0.274	0.251	0.283	0.258	43.7	3.904	√
845	0.096	0.088	0.099	0.090	43.7	0.483	no
Small Beams, Chelmsford, smooth:							
756	0.086	0.079	0.092	0.084	44.8	0.387	no
667	0.076	0.069	0.081	0.073	44.8	0.301	no
978	0.111	0.102	0.119	0.108	44.8	0.648	no
355	0.040	0.037	0.042	0.039	44.8	0.085	no
Small Beams, Chelmsford, sandblasted:							
934	0.106	0.097	0.113	0.103	44.8	0.590	no
2224	0.253	0.232	0.271	0.247	44.8	3.347	√
1334	0.152	0.139	0.163	0.148	44.8	1.205	no
2846	0.324	0.298	0.347	0.317	44.8	5.484	√

Table 7.6: Results of tests in mixed mode on small Full–Length Sandwiched Beams using the new loading geometry

Interface Fracture Data of Mixed Mode Four-Point Bend Tests							
Load [N]	K_I [MPa$\sqrt{m}$]	K_{II} [MPa$\sqrt{m}$]	K_1 [MPa$\sqrt{m}$]	K_2 [MPa$\sqrt{m}$]	$\hat{\psi}$ [°]	G_f [J/m^2]	valid?
Medium Beams, Mason, smooth: **"New" Geometry**							
12543	0.505	0.464	0.521	0.477	43.7	13.568	√
4737	0.191	0.175	0.197	0.180	43.7	1.935	√
Medium Beams, Chelmsford, smooth:							
12232	0.493	0.452	0.528	0.481	44.8	12.903	√
10675	0.430	0.395	0.461	0.420	44.8	9.823	√
4603	0.185	0.170	0.198	0.181	44.8	1.828	no
3469	0.139	0.128	0.149	0.136	44.8	1.038	no
8517	0.343	0.315	0.368	0.335	44.8	6.257	√
2668	0.107	0.099	0.115	0.105	44.8	0.614	no
1779	0.071	0.065	0.076	0.069	44.8	0.273	no
2446	0.098	0.090	0.105	0.096	44.8	0.516	no
Large Beams, Mason, smooth:							
4448	0.097	0.089	0.104	0.095	44.8	0.535	no
2224	0.048	0.045	0.051	0.048	44.8	0.134	no
6583	0.144	0.132	0.154	0.140	44.8	1.174	no
22240	0.487	0.448	0.522	0.477	44.8	13.340	√
4892	0.107	0.098	0.115	0.104	44.8	0.648	no
2668	0.058	0.054	0.062	0.057	44.8	0.193	no

Table 7.7: Results of tests on Full–Length Sandwiched Specimens in mixed mode using the new geometry for the loading arrangement of the four–point shear test

7.2.4 Results of Final Test Series

Tables 7.8 to 7.16 show the results of the final test series. All tests used the loading geometry as described in Section 6.2.1. The aggregate was Mason granite and the mortar was seven day high-strength mortar (Mix No. 8 in Table 6.2 on page 103 with the only exception of the comparative set produced with 28-day mortar.

The results are presented first in form of tables with the results of one set of specimens per table. This is followed by graphs to visualize the test results.

Fracture Test Data For Compact Beams Smooth Surface, Mason Granite				
Load [N]	K_I [MPa$\sqrt{m}$]	K_1 [MPa$\sqrt{m}$]	$\hat{\psi}$ [°]	G_f [J/m^2]
Small Beams:				
734	0.388	0.409	1.23	4.342
645	0.342	0.360	1.23	3.374
600	0.319	0.336	1.23	2.936
667	0.354	0.372	1.23	3.604
712	0.377	0.397	1.23	4.088
645	0.342	0.360	1.23	3.374
645	0.342	0.360	1.23	3.374
534	0.285	0.300	1.23	2.336
Average:				
649	**0.339**	**0.357**	**1.23**	**3.341**
Medium Beams:				
1890	0.356	0.375	1.23	3.648
1668	0.315	0.332	1.23	2.862
1468	0.279	0.293	1.23	2.236†
1357	0.258	0.272	1.23	1.922†
Average:				
1779	**0.334**	**0.352**	**1.23**	**3.224**
Large Beams:				
1696	0.174	0.183	1.23	0.870†
3120	0.315	0.332	1.23	2.866
3742	0.377	0.397	1.23	4.103
3943	0.397	0.418	1.23	4.547
Average:				
3602	**0.364**	**0.383**	**1.23**	**3.852**

†Test not valid

Table 7.8: Results of Mode I tests on Compact Sandwiched Specimens

Interface Fracture Data For Compact Specimen Smooth Surface, Mason Granite						
Load [N]	K_I [MPa$\sqrt{m}$]	K_{II} [MPa$\sqrt{m}$]	K_1 [MPa$\sqrt{m}$]	K_2 [MPa$\sqrt{m}$]	$\hat{\psi}$ [°]	G_f [J/m^2]
Small Beams:						
3012	0.395	0.210	0.411	0.212	29.2	5.776
3528	0.463	0.246	0.482	0.249	29.2	7.924
3129	0.411	0.218	0.427	0.221	29.2	6.233
3387	0.444	0.236	0.463	0.239	29.2	7.303
2621	0.344	0.183	0.358	0.185	29.2	4.374
3203	0.420	0.224	0.438	0.226	29.2	6.531
2957	0.388	0.206	0.404	0.209	29.2	5.567
3259	0.428	0.227	0.445	0.230	29.2	6.762
Average:						
3137	**0.412**	**0.219**	**0.429**	**0.221**	**29.2**	**5.696**
Medium Beams:						
14812	0.687	0.365	0.715	0.369	29.2	17.435†
10230	0.475	0.252	0.494	0.255	29.2	8.318
20906	0.970	0.516	1.010	0.521	29.2	34.733†
10008	0.464	0.247	0.483	0.250	29.2	7.960
Average:						
10119	**0.470**	**0.250**	**0.488**	**0.252**	**29.2**	**8.139**
Large Beams:						
11565	0.292	0.155	0.304	0.157	29.2	3.154
19794	0.500	0.266	0.520	0.269	29.2	9.238
9341	0.236	0.125	0.246	0.127	29.2	2.057
18682	0.472	0.251	0.491	0.254	29.2	8.229
Average:						
14845	**0.375**	**0.199**	**0.390**	**0.202**	**29.2**	**5.670**

†Test not valid. On this memorable day, someone shut down the air compressors at MIT...

Table 7.9: Results of tests on smooth Compact Sandwiched Beams in mixed mode

Interface Fracture Data For Compact Specimens Smooth Surface, Mason Granite						
Load [N]	K_I [MPa$\sqrt{m}$]	K_{II} [MPa$\sqrt{m}$]	K_1 [MPa$\sqrt{m}$]	K_2 [MPa$\sqrt{m}$]	$\hat{\psi}$ [°]	G_f [J/m^2]
Small Beams:						
5339	0.199	0.373	0.202	0.388	63.1	5.148
5116	0.191	0.357	0.193	0.372	63.1	4.728
5060	0.189	0.353	0.191	0.368	63.1	4.625
4848	0.181	0.338	0.183	0.352	63.1	4.245
5100	0.191	0.356	0.193	0.371	63.1	4.698
5150	0.192	0.359	0.195	0.374	63.1	4.791
5800	0.217	0.405	0.219	0.421	63.1	6.076
5560	0.208	0.388	0.210	0.404	63.1	5.584
Average:						
5247	**0.196**	**0.366**	**0.198**	**0.381**	**63.1**	**4.987**
Medium Beams:						
13678	0.181	0.337	0.183	0.351	63.1	4.218
17369	0.229	0.429	0.232	0.446	63.1	6.802
17414	0.230	0.430	0.233	0.447	63.1	6.837
17881	0.236	0.441	0.239	0.459	63.1	7.209
Average:						
16585	**0.219**	**0.409**	**0.221**	**0.426**	**63.1**	**6.266**
Large Beams:						
28645	0.206	0.385	0.208	0.401	63.1	5.489
10675	0.077	0.143	0.078	0.149	63.1	0.762†
27133	0.195	0.364	0.197	0.379	63.1	4.924
46526	0.335	0.625	0.338	0.651	63.1	14.48†
Average:						
27889	**0.200**	**0.374**	**0.202**	**0.390**	**63.1**	**5.207**

†Test not valid

Table 7.10: Results of tests on smooth Compact Sandwiched Beams in mixed mode

Fracture Test Data For Compact Beams sandblasted Surface, Mason Granite				
Load [N]	K_I [MPa$\sqrt{m}$]	K_1 [MPa$\sqrt{m}$]	$\hat{\psi}$ [°]	G_f [J/m^2]
Small Beams:				
795	0.415	0.437	1.23	4.961
612	0.320	0.337	1.23	2.951
746	0.389	0.410	1.23	4.367
1023	0.532	0.561	1.23	8.174
Average:				
794	**0.414**	**0.436**	**1.23**	**5.113**
Medium Beams:				
2376	0.443	0.466	1.23	5.654
2018	0.377	0.398	1.23	4.107
1660	0.312	0.329	1.23	2.807†
2514	0.468	0.493	1.23	6.317
Average:				
2303	**0.429**	**0.452**	**1.23**	**5.359**
Large Beams:				
4121	0.415	0.438	1.23	4.977
3409	0.345	0.363	1.23	3.425
4321	0.435	0.459	1.23	5.465
4565	0.460	0.484	1.23	6.093
Average:				
4104	**0.414**	**0.436**	**1.23**	**4.990**

†Test not valid

Table 7.11: Results of tests on sandblasted Compact Sandwiched Beams in Mode I

Interface Fracture Data For Compact Specimen Sandblasted Surface, Mason Granite						
Load [N]	K_I [MPa$\sqrt{m}$]	K_{II} [MPa$\sqrt{m}$]	K_1 [MPa$\sqrt{m}$]	K_2 [MPa$\sqrt{m}$]	$\hat{\psi}$ [°]	G_f [J/m^2]
Small Beams:						
1639	0.215	0.114	0.224	0.116	29.2	1.710†
2407	0.316	0.168	0.329	0.170	29.2	3.688
3314	0.435	0.231	0.453	0.234	29.2	6.992
2675	0.351	0.187	0.365	0.189	29.2	4.556
3306	0.434	0.231	0.452	0.233	29.2	6.958
2769	0.363	0.193	0.378	0.195	29.2	4.881
Average:						
2894	**0.380**	**0.202**	**0.395**	**0.204**	**29.2**	**5.415**
Medium Beams:						
10764	0.499	0.266	0.520	0.268	29.2	9.208
10275	0.477	0.254	0.496	0.256	29.2	8.390
10297	0.478	0.254	0.497	0.257	29.2	8.426
14790	0.686	0.365	0.714	0.369	29.2	17.383†
Average:						
10445	**0.485**	**0.258**	**0.505**	**0.260**	**29.27**	**8.675**
Large Beams:						
16035	0.405	0.215	0.422	0.218	29.2	6.063
14790	0.373	0.199	0.389	0.201	29.2	5.158
13433	0.339	0.180	0.353	0.182	29.2	4.255
15946	0.403	0.214	0.419	0.216	29.2	5.996
Average:						
15051	**0.380**	**0.202**	**0.396**	**0.204**	**29.2**	**5.368**

†Test not valid

Table 7.12: Results of tests on sandblasted Compact Sandwiched Beams in mixed mode

Interface Fracture Data For Compact Specimen Sandblasted Surface, Mason Granite						
Load [N]	K_I [MPa$\sqrt{m}$]	K_{II} [MPa$\sqrt{m}$]	K_1 [MPa$\sqrt{m}$]	K_2 [MPa$\sqrt{m}$]	$\hat{\psi}$ [°]	G_f [J/m^2]
Small Beams:						
3560	0.133	0.248	0.134	0.259	63.1	2.289†
7162	0.268	0.500	0.271	0.520	63.1	9.266
8675	0.324	0.605	0.328	0.630	63.1	13.59
6673	0.249	0.466	0.252	0.485	63.1	8.043
Average:						
7503	**0.280**	**0.524**	**0.283**	**0.545**	**63.1**	**10.30**
Medium Beams:						
23930	0.316	0.590	0.320	0.615	63.1	12.91
23196	0.306	0.572	0.310	0.596	63.1	12.13
21128	0.279	0.521	0.282	0.543	63.1	10.06
19349	0.256	0.477	0.258	0.497	63.1	8.441
Average:						
21901	**0.289**	**0.540**	**0.292**	**0.563**	**63.1**	**10.88**
Large Beams:						
45992	0.331	0.618	0.334	0.643	63.1	14.15
38876	0.279	0.522	0.283	0.544	63.1	10.110
33894	0.244	0.455	0.246	0.474	63.1	7.685
43146	0.310	0.579	0.314	0.603	63.1	12.45
Average:						
40477	**0.291**	**0.544**	**0.294**	**0.566**	**63.1**	**11.10**

†Test not valid

Table 7.13: Results of tests on sandblasted Compact Sandwiched Beams in mixed mode

Interface Fracture Data For Compact Specimen Smooth Surface, Mason Granite and 28-Day Mortar						
Load [N]	K_I [MPa$\sqrt{m}$]	K_{II} [MPa$\sqrt{m}$]	K_1 [MPa$\sqrt{m}$]	K_2 [MPa$\sqrt{m}$]	$\hat{\psi}$ [°]	G_f [J/m^2]
Small Beams:						
7585	0.283	0.529	0.286	0.551	63.1	10.39
6740	0.252	0.470	0.255	0.490	63.1	8.205
7563	0.283	0.528	0.286	0.550	63.1	10.33
7941	0.297	0.554	0.300	0.577	63.1	11.39
7541	0.282	0.526	0.285	0.548	63.1	10.27
7118	0.266	0.497	0.269	0.517	63.1	9.151
5161	0.193	0.360	0.195	0.375	63.1	4.811†
3893	0.145	0.272	0.147	0.283	63.1	2.738†
Average:						
7415	**0.277**	**0.517**	**0.280**	**0.539**	**63.1**	**9.956**
Medium Beams:						
21640	0.286	0.534	0.289	0.556	63.1	10.56
20461	0.270	0.505	0.273	0.526	63.1	9.439
22863	0.302	0.564	0.305	0.587	63.1	11.78
21172	0.280	0.522	0.283	0.544	63.1	10.11
Average:						
21534	**0.284**	**0.531**	**0.288**	**0.553**	**63.1**	**10.47**
Large Beams:						
44302	0.319	0.595	0.322	0.619	63.1	13.13
35584	0.256	0.478	0.259	0.497	63.1	8.471
22240	0.160	0.299	0.162	0.311	63.1	3.309†
23130	0.166	0.311	0.168	0.323	63.1	3.579†
Average:						
39943	**0.287**	**0.536**	**0.290**	**0.558**	**63.1**	**10.80**

†Test not valid

Table 7.14: Results of tests on compact beams with smooth Mason granite in mixed mode and using 28-day mortar for comparison

Fracture Test Data For Compact Beams Flamed Surface, Mason Granite				
Load [N]	K_I [MPa$\sqrt{m}$]	K_I [MPa$\sqrt{m}$]	$\hat{\psi}$ [°]	G_f [J/m^2]
Small Beams:				
1524	0.791	0.834	1.23	18.057†
1118	0.582	0.613	1.23	9.751
1034	0.538	0.567	1.23	8.349
1023	0.532	0.561	1.23	8.174
928	0.483	0.509	1.23	6.736
1223	0.636	0.670	1.23	11.655
1019	0.530	0.559	1.23	8.110
Average:				
1058	**0.550**	**0.580**	**1.23**	**8.796**
Medium Beams:				
3114	0.578	0.608	1.23	9.620
2891	0.537	0.566	1.23	8.314
3269	0.606	0.638	1.23	10.591
3314	0.614	0.647	1.23	10.877
Average:				
3147	**0.584**	**0.615**	**1.23**	**9.850**
Large Beams:				
7234	0.725	0.764	1.23	15.162
5344	0.537	0.566	1.23	8.318
4899	0.493	0.519	1.23	7.004
Average:				
5826	**0.585**	**0.616**	**1.23**	**10.161**

†Test not valid

Table 7.15: Results of tests on flamed Compact Sandwiched Beams in Mode I

Interface Fracture Data For Compact Specimen Flamed Surface, Mason Granite						
Load [N]	K_I [MPa$\sqrt{m}$]	K_{II} [MPa$\sqrt{m}$]	K_1 [MPa$\sqrt{m}$]	K_2 [MPa$\sqrt{m}$]	$\hat{\psi}$ [°]	G_f [J/m^2]
Small Beams:						
4595	0.172	0.321	0.174	0.334	63.1	3.814†
5784	0.216	0.404	0.218	0.420	63.1	6.042†
5339	0.199	0.373	0.202	0.388	63.1	5.148†
5561	0.208	0.388	0.210	0.404	63.1	5.586†
4227	0.158	0.295	0.160	0.307	63.1	3.227†
5895	0.220	0.411	0.223	0.428	63.1	6.276†
5561	0.208	0.388	0.210	0.404	63.1	5.586†
6006	0.224	0.419	0.227	0.436	63.1	6.515†
Average:						
5691	**0.213**	**0.397**	**0.215**	**0.413**	**63.1**	**5.859**†
Medium Beams:						
16458	0.217	0.406	0.220	0.423	63.1	6.107†
17236	0.228	0.425	0.230	0.443	63.1	6.698†
16680	0.220	0.412	0.223	0.428	63.1	6.273†
16458	0.217	0.406	0.220	0.423	63.1	6.107†
Average:						
16708	**0.221**	**0.412**	**0.223**	**0.429**	**63.1**	**6.296**†
Large Beams:						
52931	0.381	0.711	0.385	0.740	63.1	18.743
44391	0.319	0.596	0.323	0.621	63.1	13.182
48216	0.347	0.648	0.350	0.674	63.1	15.552
52664	0.379	0.707	0.383	0.736	63.1	18.554
Average:						
49551	**0.356**	**0.665**	**0.360**	**0.693**	**63.1**	**16.508**

†Test not valid. It was later found out that a mistake in the test set–up caused the loss of data for small and medium beams.

Table 7.16: Results of tests on flamed Compact Sandwiched Beams in mixed mode

Fracture Toughness Curves

The fracture toughness curve is a property of a particular material combination. It shows the dependence of the fracture energy on the loading angle. Here, all tests (smooth, sandblasted, and flamed) are included in one graph. Each point resembles the average for one specimen size in the respective roughness group. The curve for the sandblasted specimens is a curvefit through the averages of the data points for one loading angle, while the other two curvatures are somewhat arbitrary because of lacking or inferior data for a loading angle of 30°.

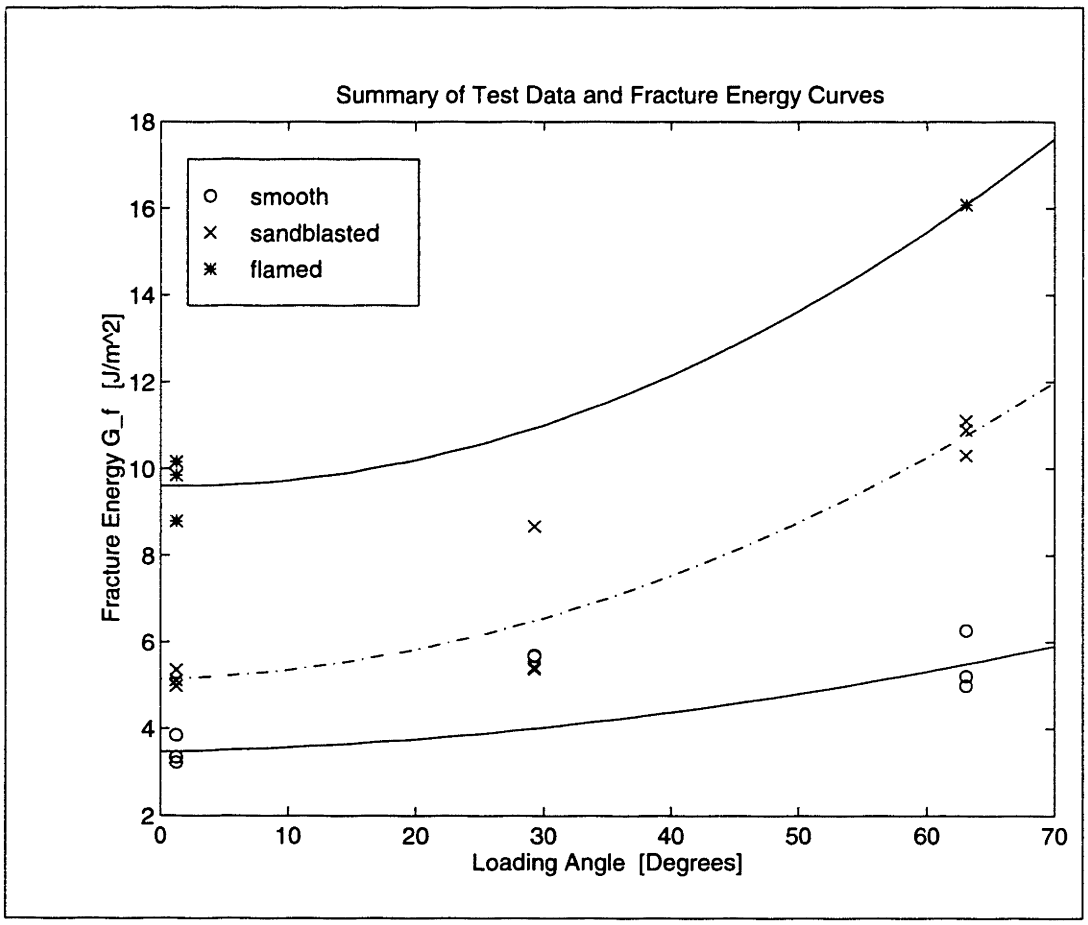

Figure 7-1: Fracture energy release rates of all three sizes and roughnesses vs. loading angle

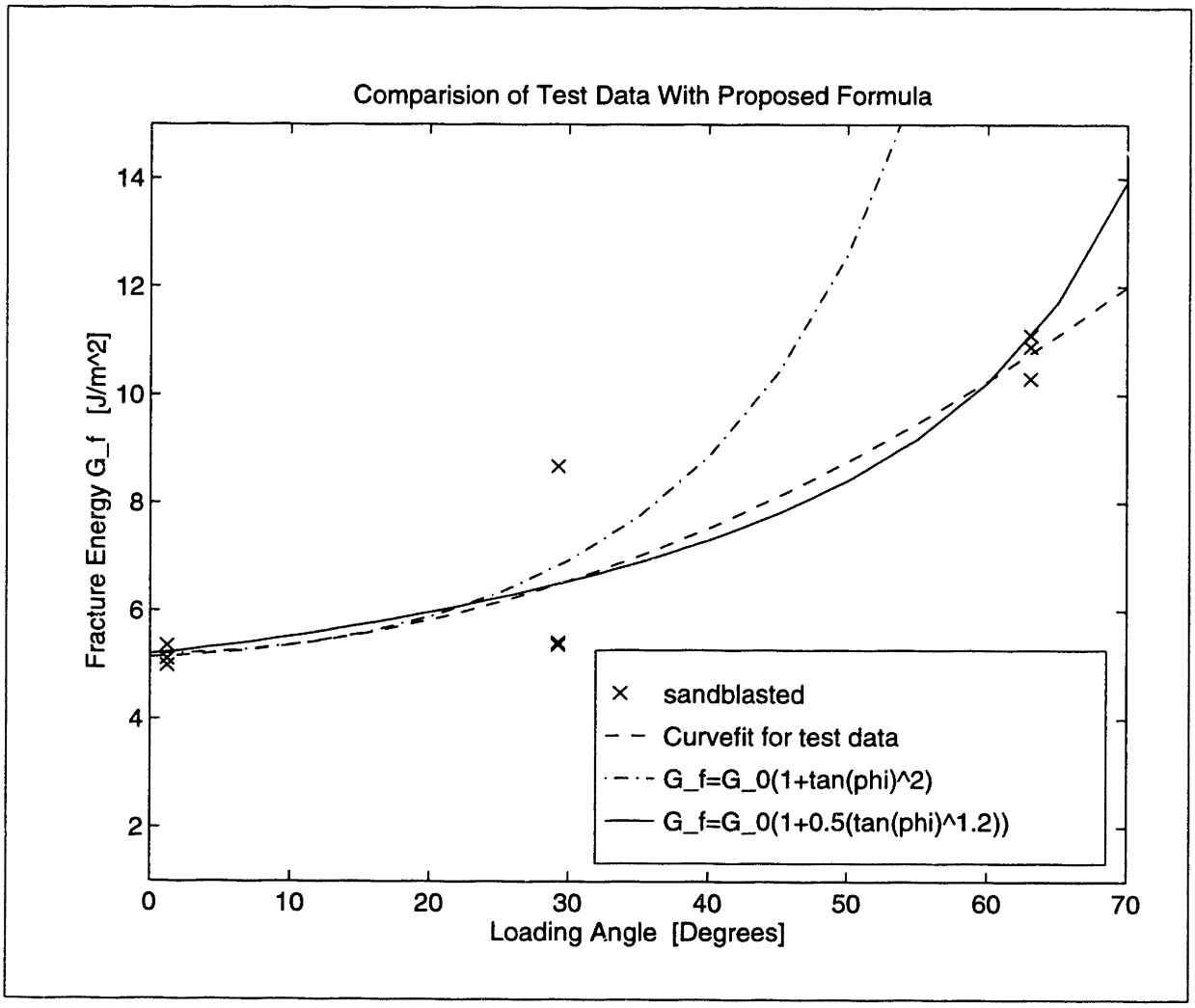

Figure 7-2: Comparison of curvefit of test data with proposed formulas, the first one is from He et al (1989), the second a best fit of this form to the test data, indicating that roughness induced shielding governs over surface forces as cause of the increase of fracture energy with loading angle.

7.3 Size Effect Parameters

7.3.1 Procedure for Calculation of Size Effect Parameters

Procedure of Calculations for Size Effect Data				
Step	**Description**	**Equation**	**Unit**	**Example**
1	Define char. dimensions	d_1, d_2, d_3	mm	50.800
2	Rel. crack length	$\alpha_0 = a/d$	—	0.375
3	Define initial factor	c_n	—	0.564
4	Measure of tensile str.	f'_t	MPa	5.375
5	Nominal Stress	$\sigma_N = c_n * P_u/d_i^2$	MPa	5.880
6	Calculate Y	$Y = (f'_t/\sigma_N)^2$	—	126.675
7	Plot	Y vs. d_i	—	—
8	Regression:$A\&C$	$Y = AX + C$	—	—
9	Calculate B	$B = C^{-1/2}$	—	0.4
10	Calculate d_0	$d_0 = C/A$	—	4.842
11	Calculate β	$\beta_i = d_i/d_0$	—	10.491
12	Plot size effect	$\ln \sigma_N/Bf'_t$ vs. $\ln d_i/d_0$	—	—
13	For comparison, plot the size effect of LEFM and plastic limit analysis			
14	Vary c_n, repeat 3–14 until coincidence			

Table 7.17: Procedure for calculation of size effect parameters from test data. See Chapter 5 for reference.

7.3.2 Results of Size Effect Analysis

Following is a table summarizing the size effect data for all tests performed in the final test series. All these tests used compact specimens.

Specimen	A	C	B	c_n	d_0	β
Smooth, Mode I	2.6348	29.156	0.1852	1.72	11.0659	4.5–14
Smooth,$\hat{\psi}$ =63°	43.3622	29.3277	0.1847	0.0535	0.6763	75–225
Sandblasted, Mode I	11.6530	29.1425	0.1852	0.685	2.5009	20–62
Sandblasted,$\hat{\psi}$ =63°	4.5543	28.9143	0.1860	0.116	6.3488	8–24
Smooth,28–day, $\hat{\psi}$ =63°	8.1178	29.2830	0.1848	0.089	3.6073	14–42
Flamed, Mode I	7.2646	28.8465	0.1862	0.655	3.9709	12–37

Table 7.18: Summary of size effect test data

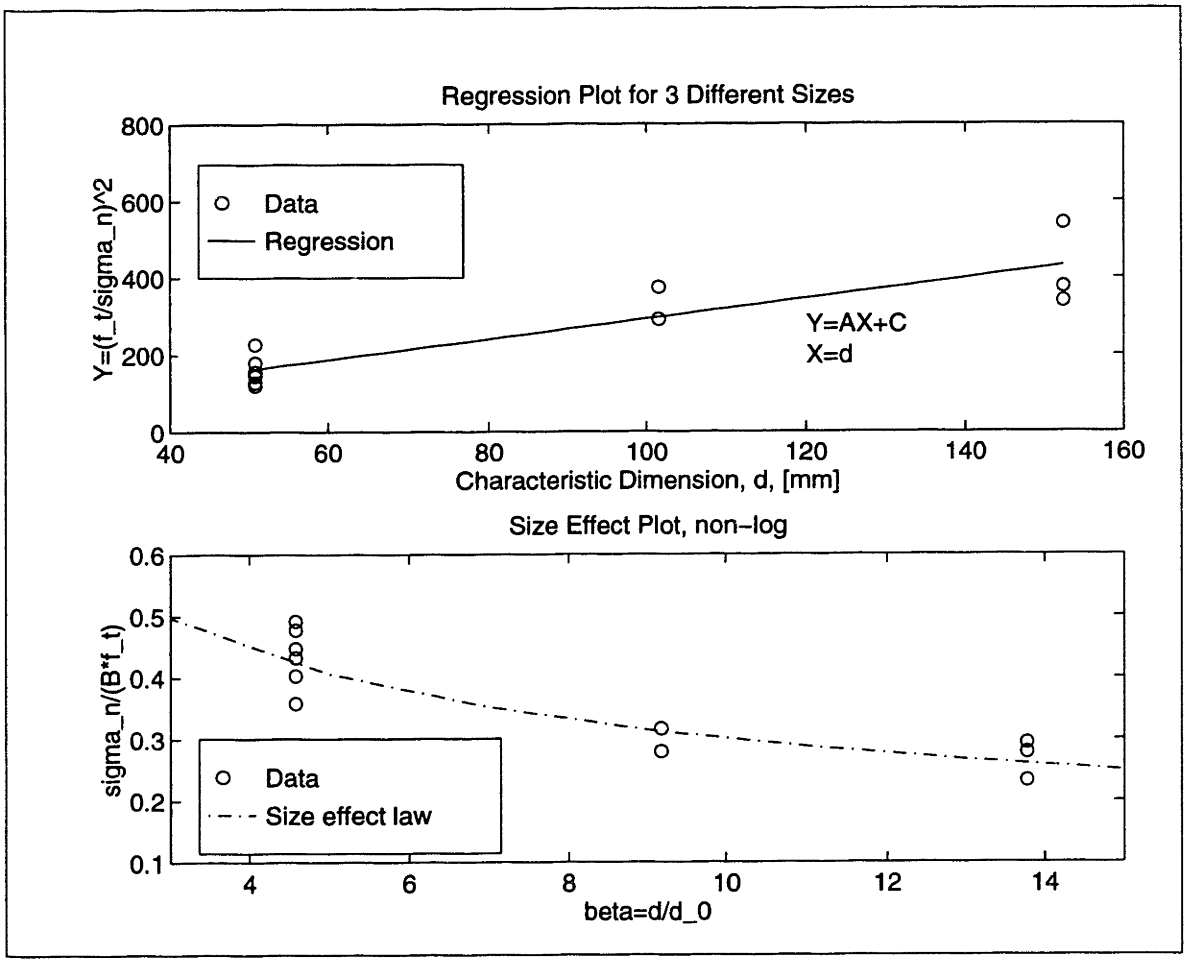

$A = 2.6348$, $C = 29.156$, $B = 0.1852$

$c_n = 1.72$, $f_t = 5.375$ MPa, $d_0 = 11.0659$ mm

Figure 7-3: Size effect plots for 81-MPa mortar/Mason (smooth) interface fracture in Mode I, Part 1

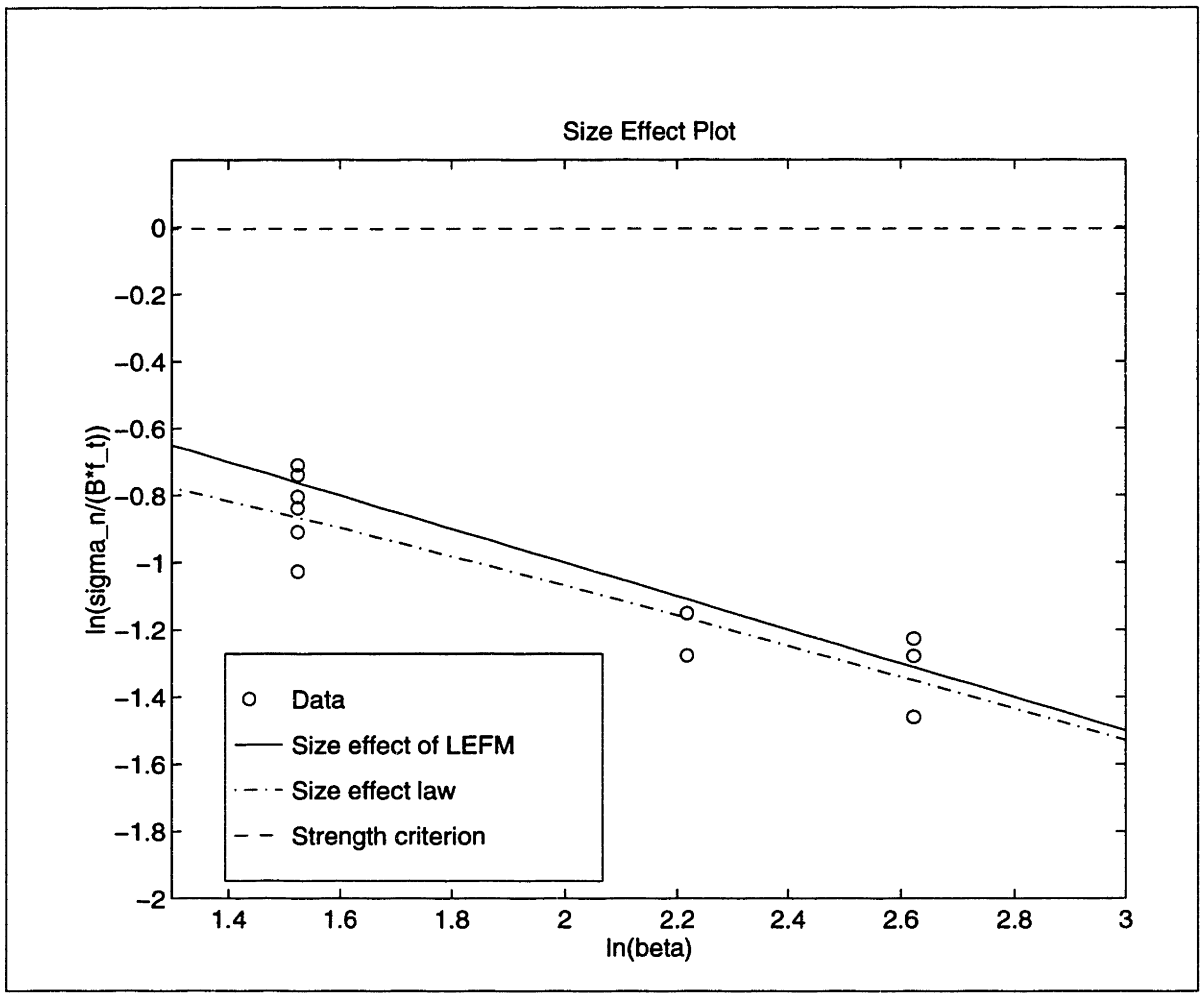

$A = 2.6348$, $C = 29.156$, $B = 0.1852$
$c_n = 1.72$, $f_t = 5.375$ MPa, $d_0 = 11.0659$ mm

Figure 7-4: (contd.) Size effect plots for 81-MPa mortar/Mason (smooth) interface fracture in Mode I, Part 2

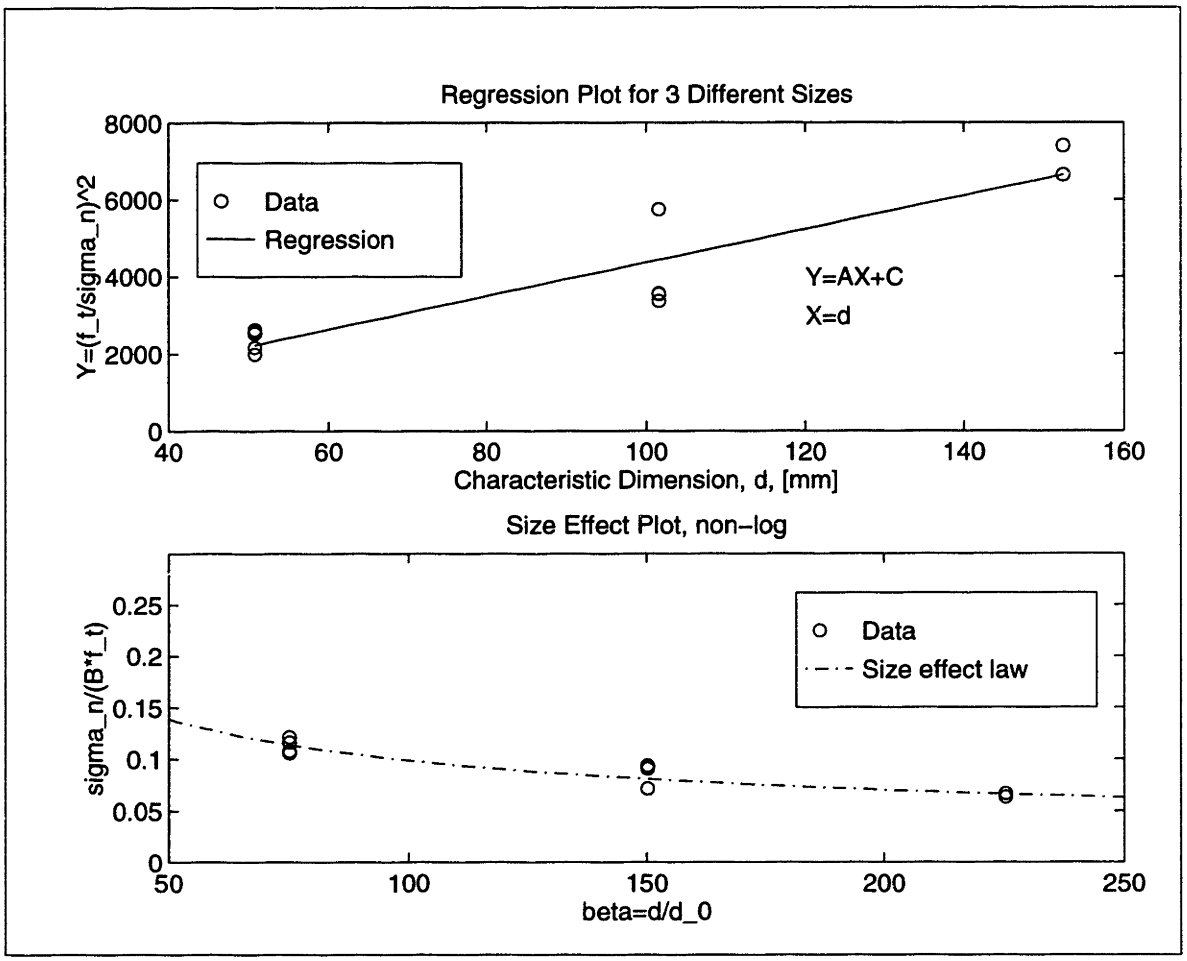

$A = 43.3622$, $C = 29.3277$, $B = 0.1847$
$c_n = 0.0535$, $f_t = 5.375$ MPa, $d_0 = 0.6763$ mm

Figure 7-5: Size effect plots for 81-MPa mortar/Mason (smooth) interface fracture in mixed mode ($\hat{\psi}$ =63°), Part 1

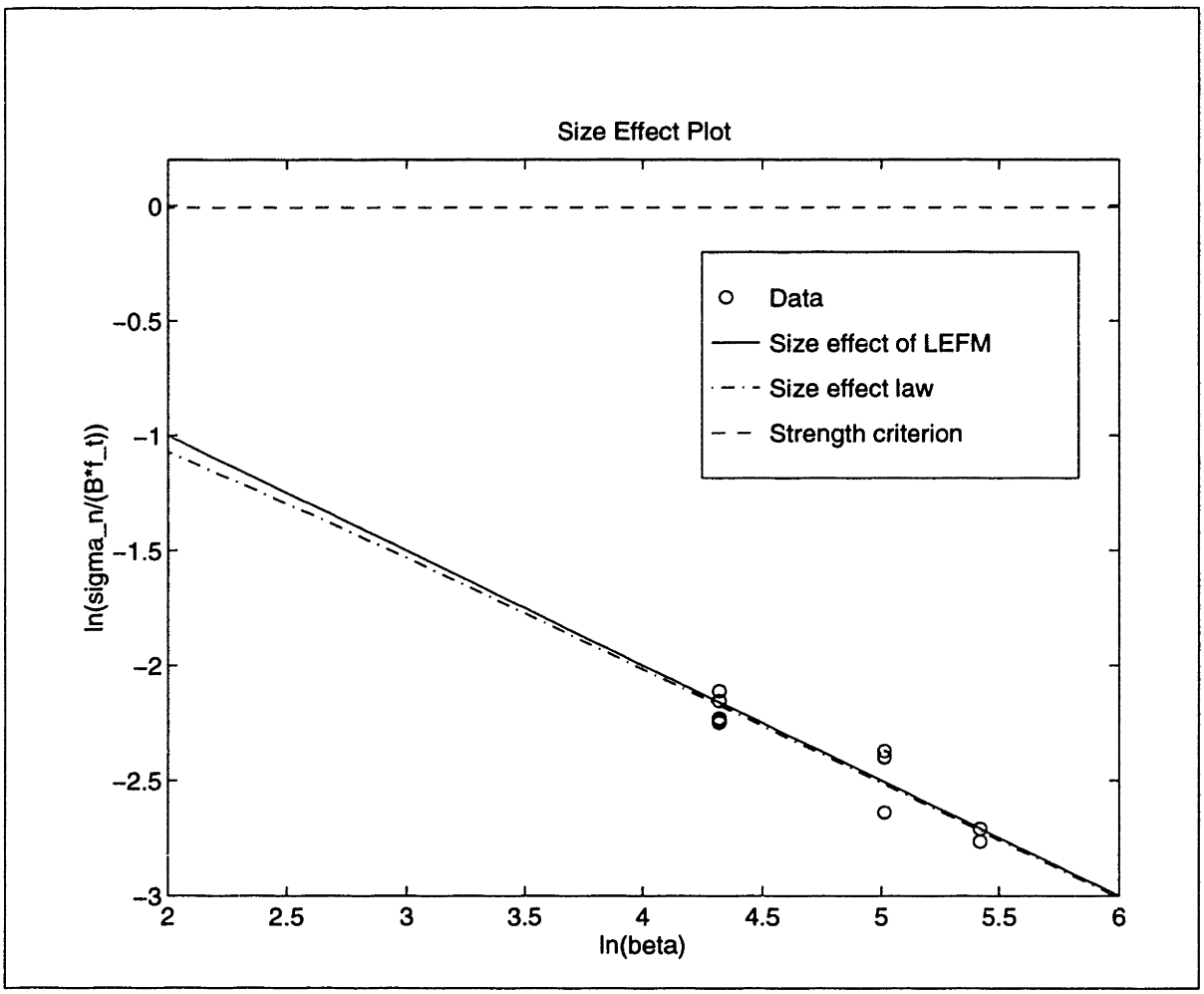

$A = 43.3622$, $C = 29.3277$, $B = 0.1847$
$c_n = 0.0535$, $f_t = 5.375$ MPa, $d_0 = 0.6763$ mm

Figure 7-6: (contd.) Size effect plots for 81-MPa mortar/Mason (smooth) interface fracture in mixed mode ($\hat{\psi}$ =63°), Part 2

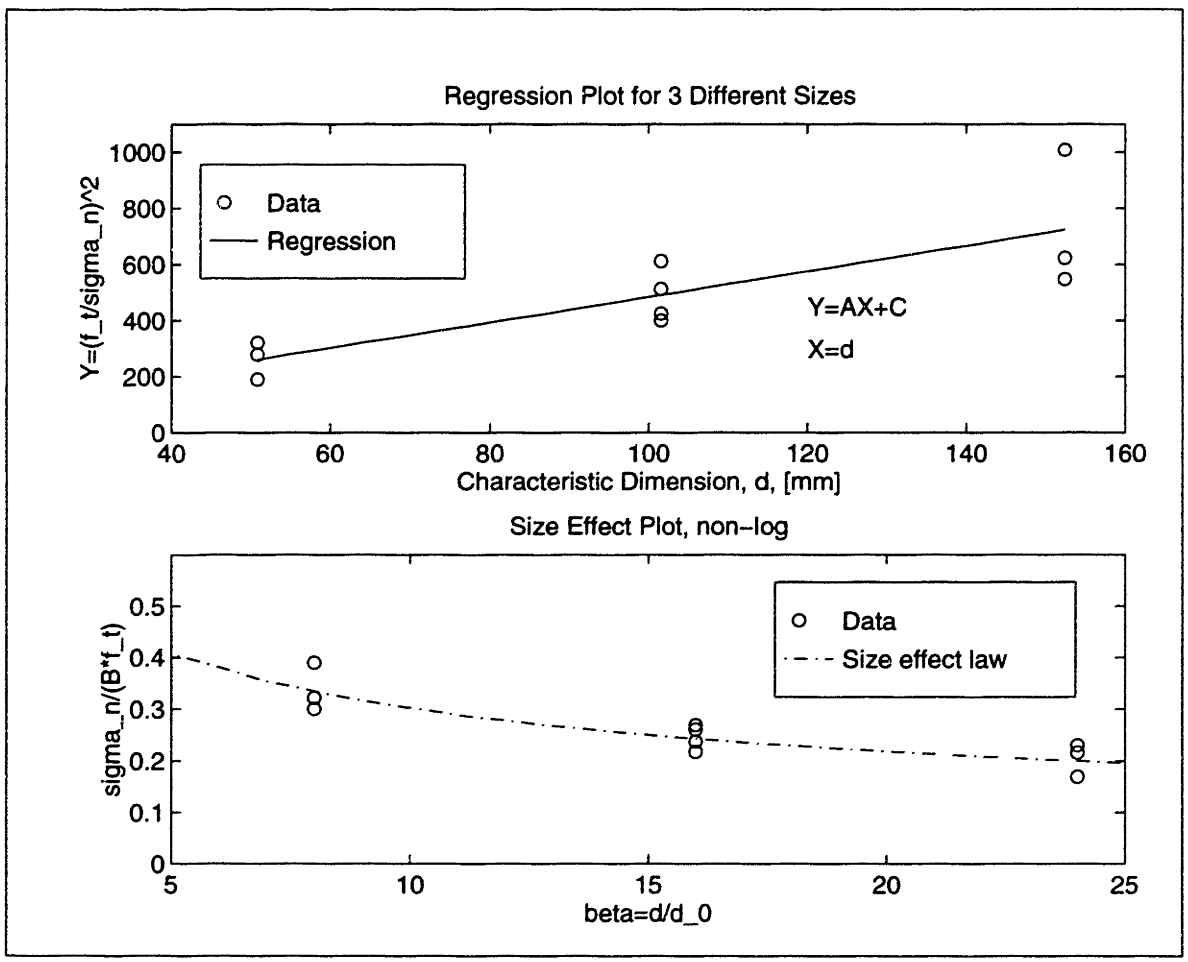

$A = 4.5543$, $C = 28.9143$, $B = 0.1860$
$c_n = 0.116$, $f_t = 5.375$ MPa, $d_0 = 6.3488$ mm

Figure 7-7: Size effect plots for 81-MPa mortar/Mason (sandblasted) interface fracture in mixed mode ($\hat{\psi}$ =63°), Part 1

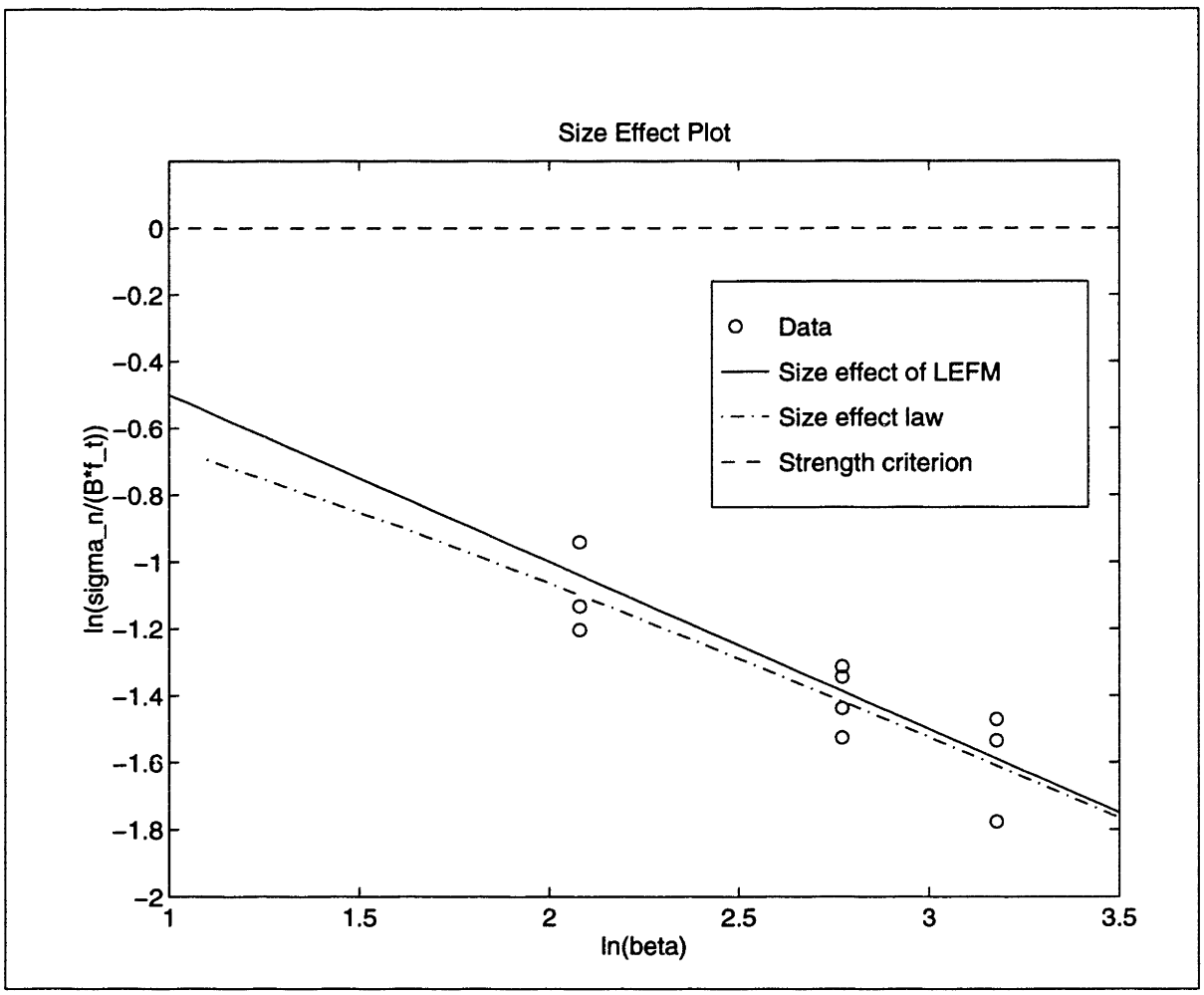

$A = 4.5543$, $C = 28.9143$, $B = 0.1860$
$c_n = 0.116$, $f_t = 5.375$ MPa, $d_0 = 6.3488$ mm

Figure 7-8: (contd.) Size effect plots for 81-MPa mortar/Mason (sandblasted) interface fracture in mixed mode ($\hat{\psi}$ =63°), Part 2

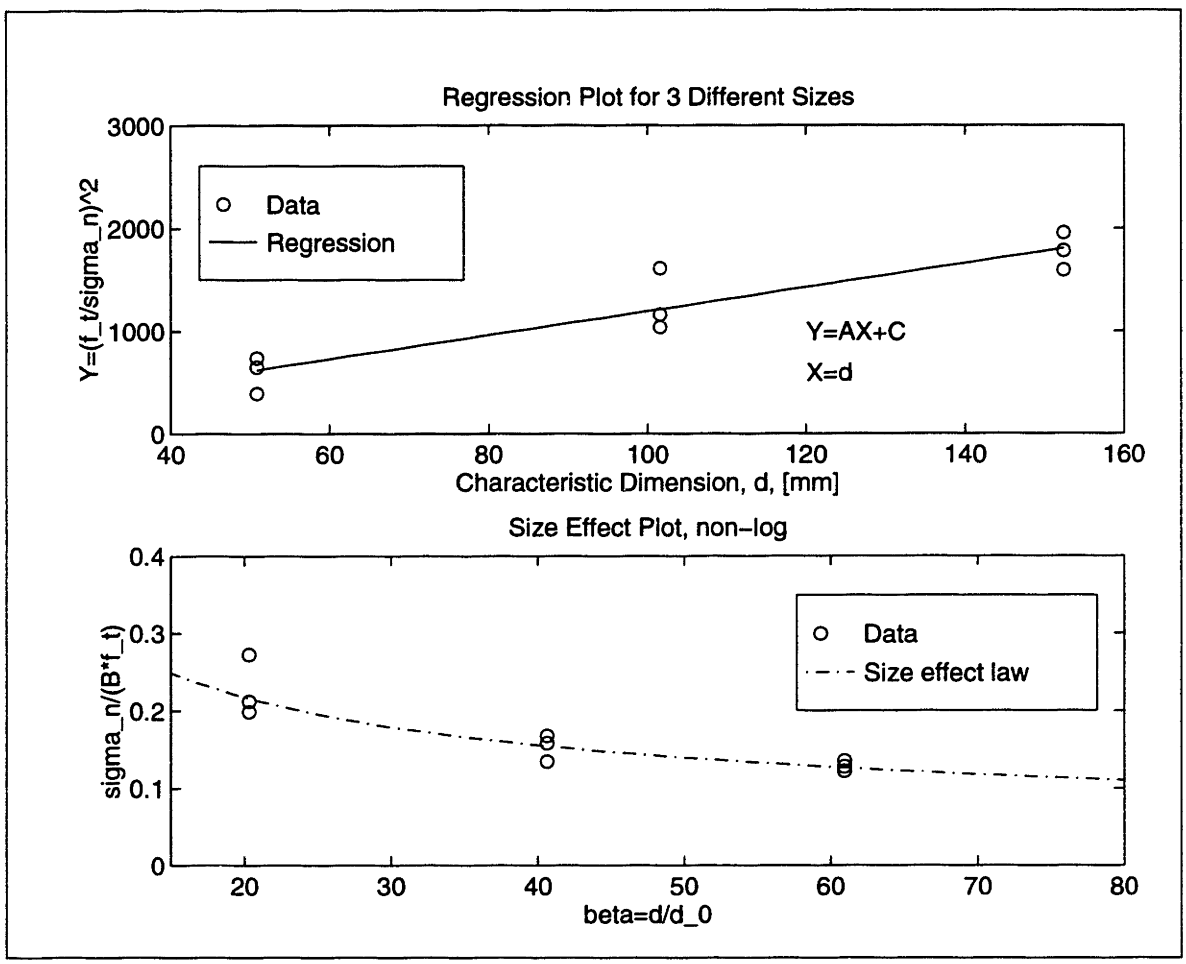

$A = 11.6530$, $C = 29.1425$, $B = 0.1852$
$c_n = 0.685$, $f_t = 5.375$ MPa, $d_0 = 2.5009$ mm

Figure 7-9: Size effect plots for 81-MPa mortar/Mason (sandblasted) interface fracture in Mode I, Part 1

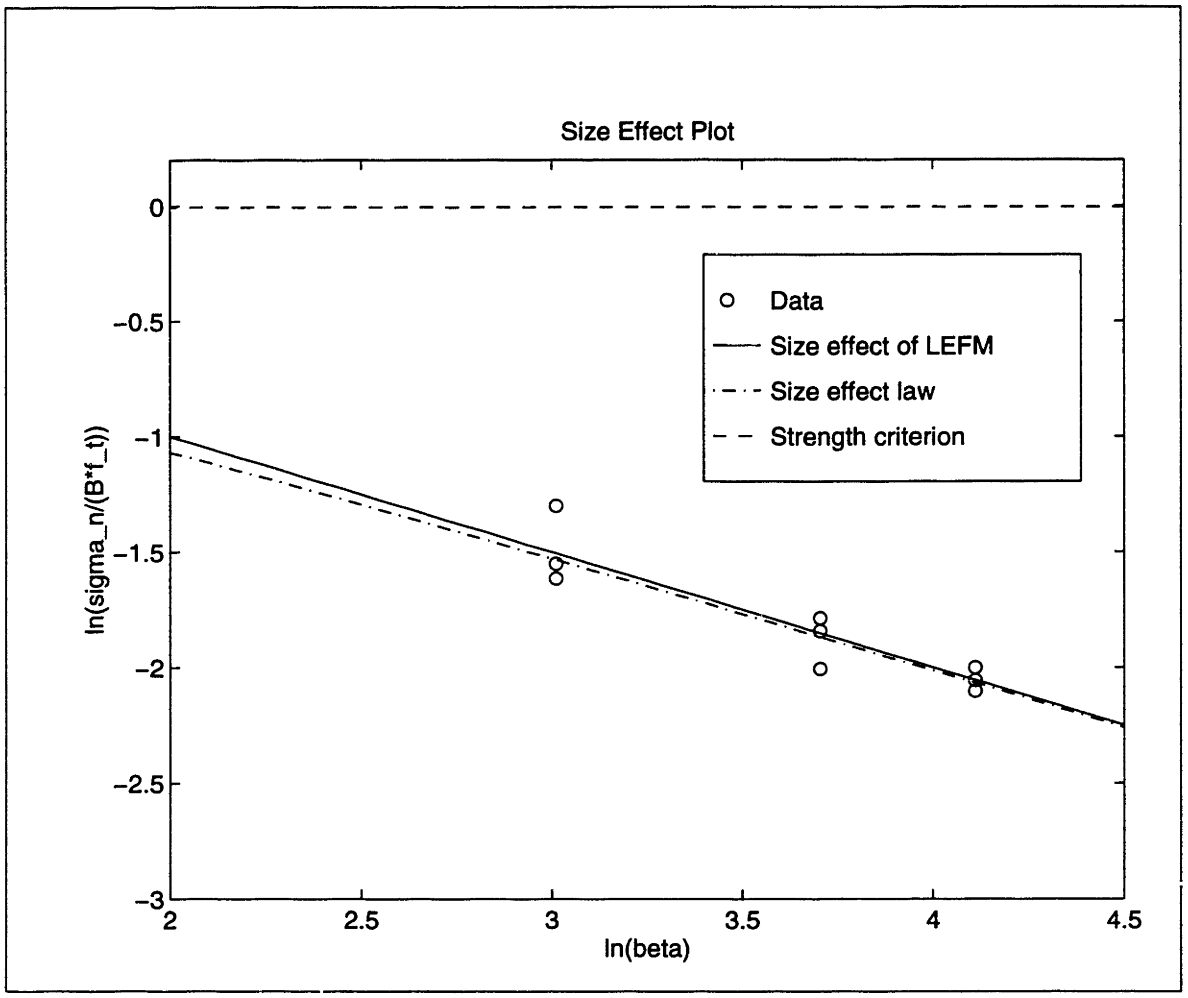

$A = 11.6530$, $C = 29.1425$, $B = 0.1852$
$c_n = 0.685$, $f_t = 5.375$ MPa, $d_0 = 2.5009$ mm

Figure 7-10: (contd.) Size effect plots for 81-MPa mortar/Mason (sandblasted) interface fracture in Mode I, Part 2

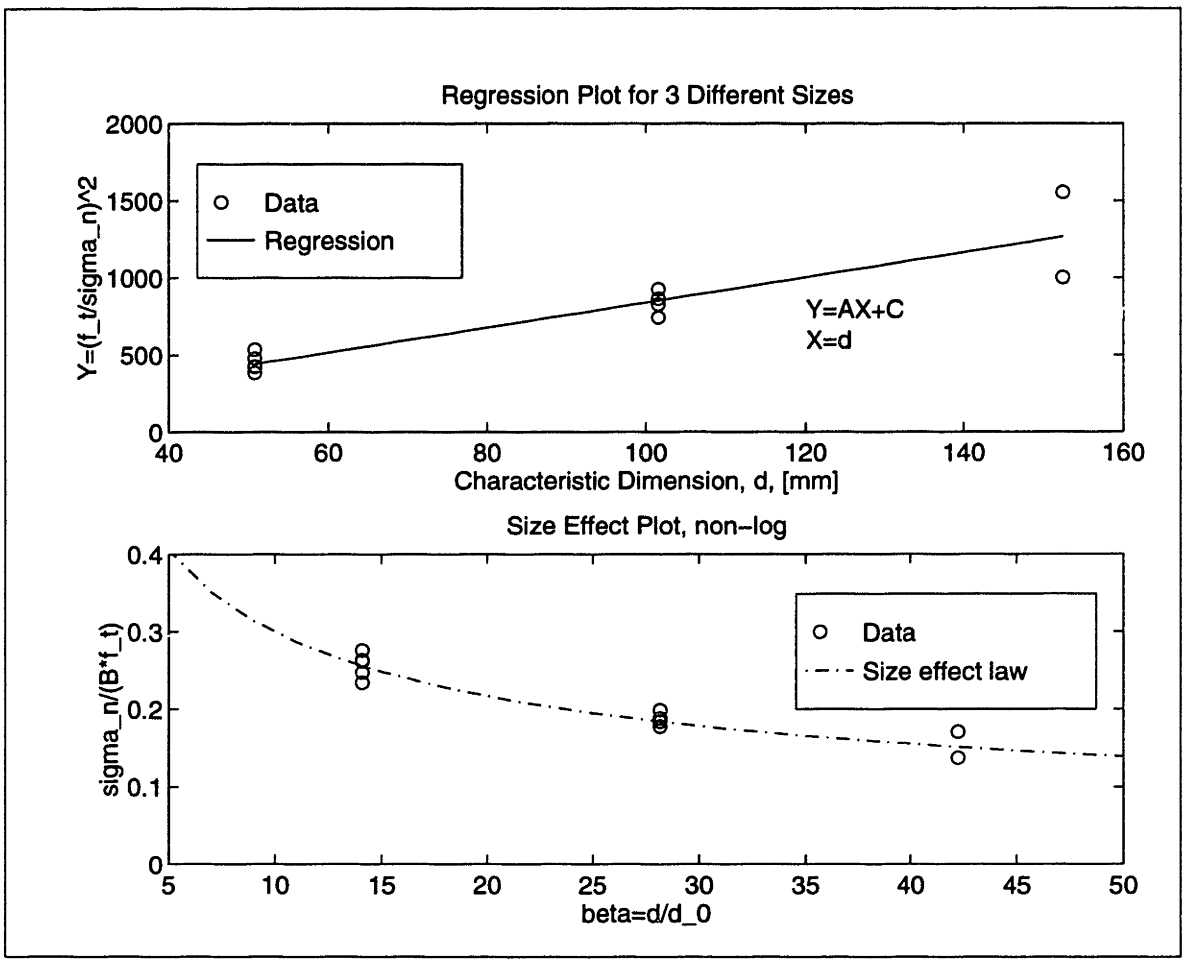

$A = 8.1178$, $C = 29.2830$, $B = 0.1848$
$c_n = 0.089$, $f_t = 5.375$ MPa, $d_0 = 3.6073$ mm

Figure 7-11: Size effect plots for 83-MPa 28-day mortar/Mason (smooth) interface fracture in mixed mode ($\hat{\psi}$ =63°), Part 1

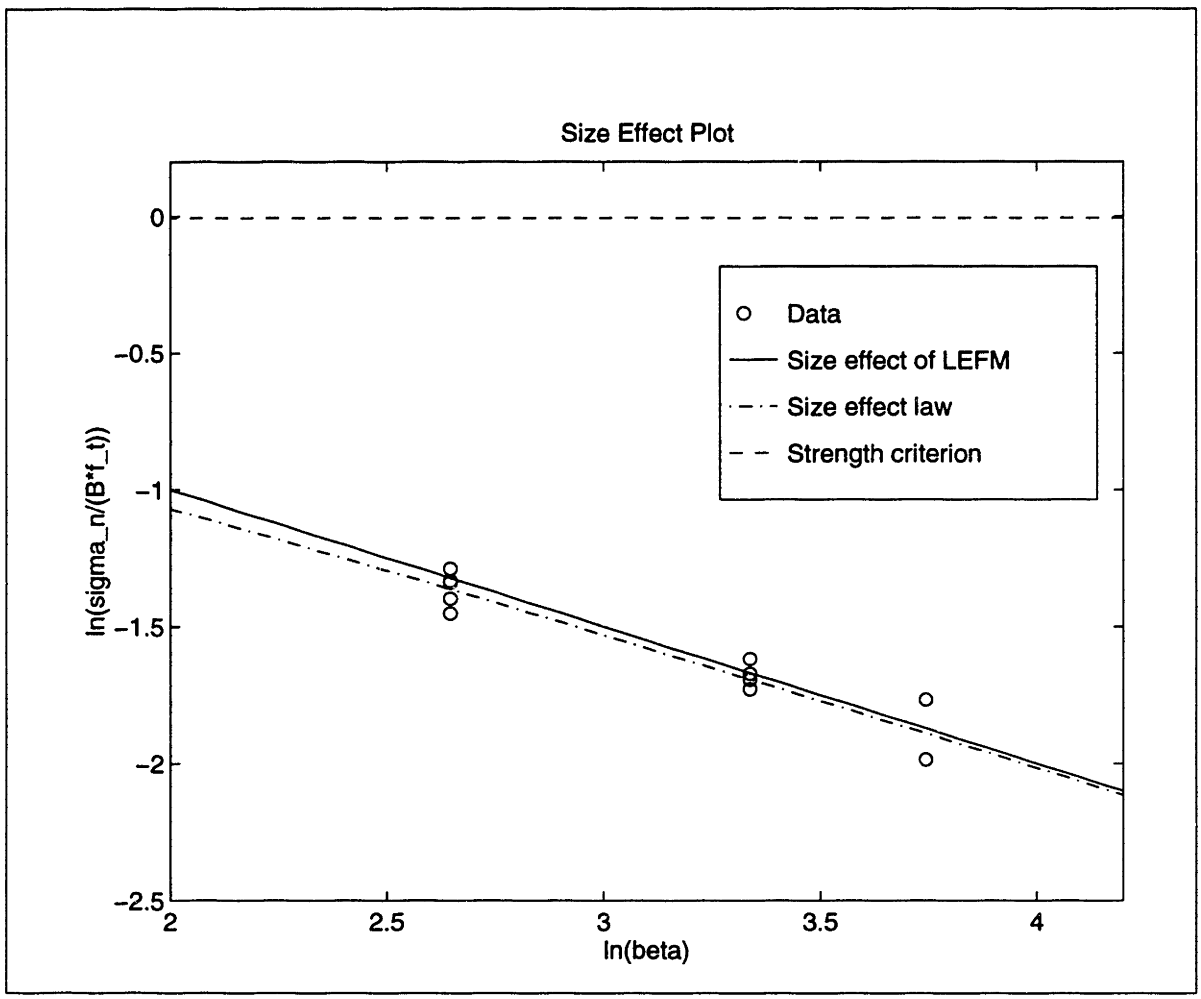

$A = 8.1178$, $C = 29.2830$, $B = 0.1848$
$c_n = 0.089$, $f_t = 5.375$ MPa, $d_0 = 3.6073$ mm

Figure 7-12: (contd.) Size effect plots for 83-MPa 28-day mortar/Mason (smooth) interface fracture in mixed mode ($\hat{\psi}$ =63°), Part 2

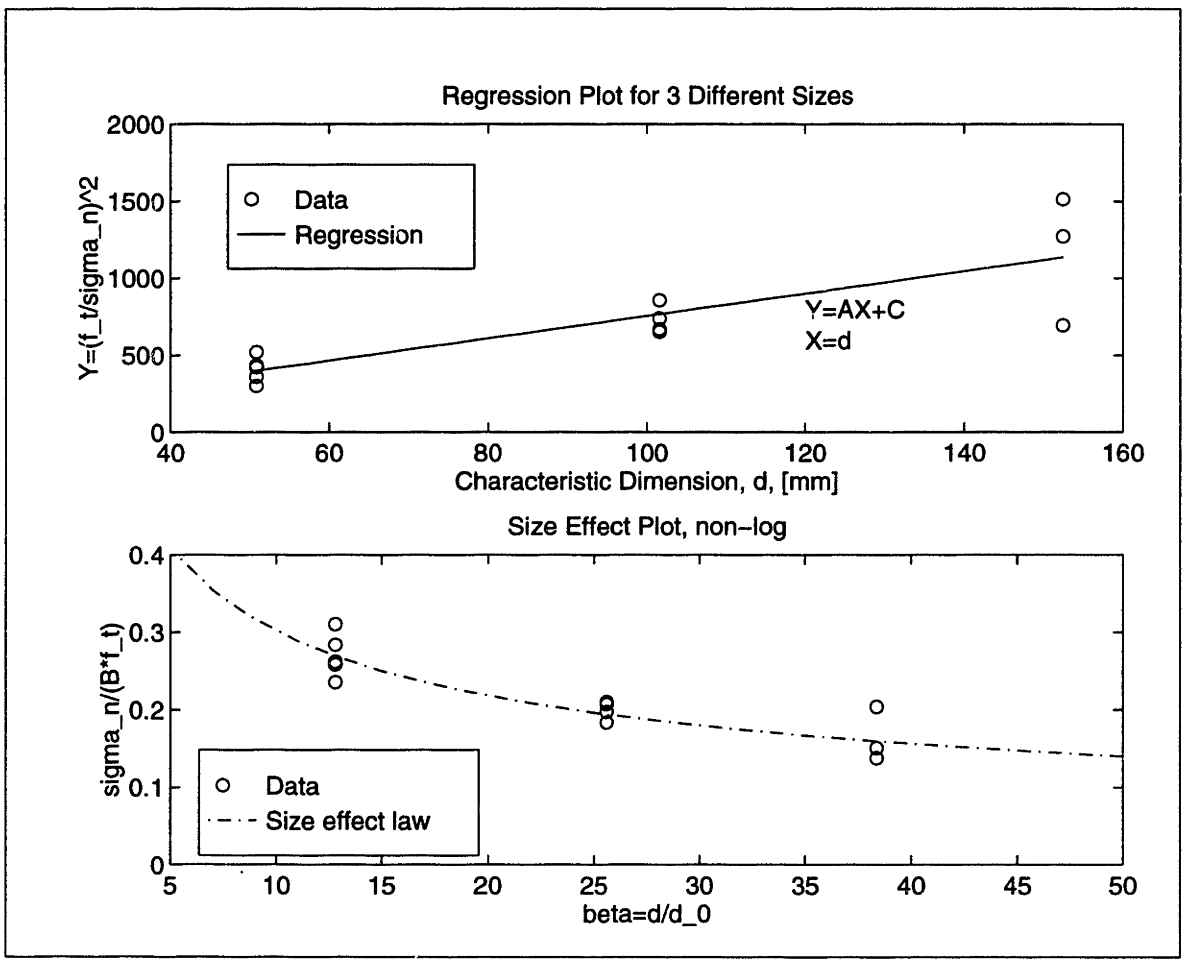

$A = 7.2646$, $C = 28.8465$, $B = 0.1862$
$c_n = 0.655$, $f_t = 5.375$ MPa, $d_0 = 3.9709$ mm

Figure 7-13: Size effect plots for 81-MPa 7-day mortar/Mason (flamed) interface fracture in Mode I, Part 1

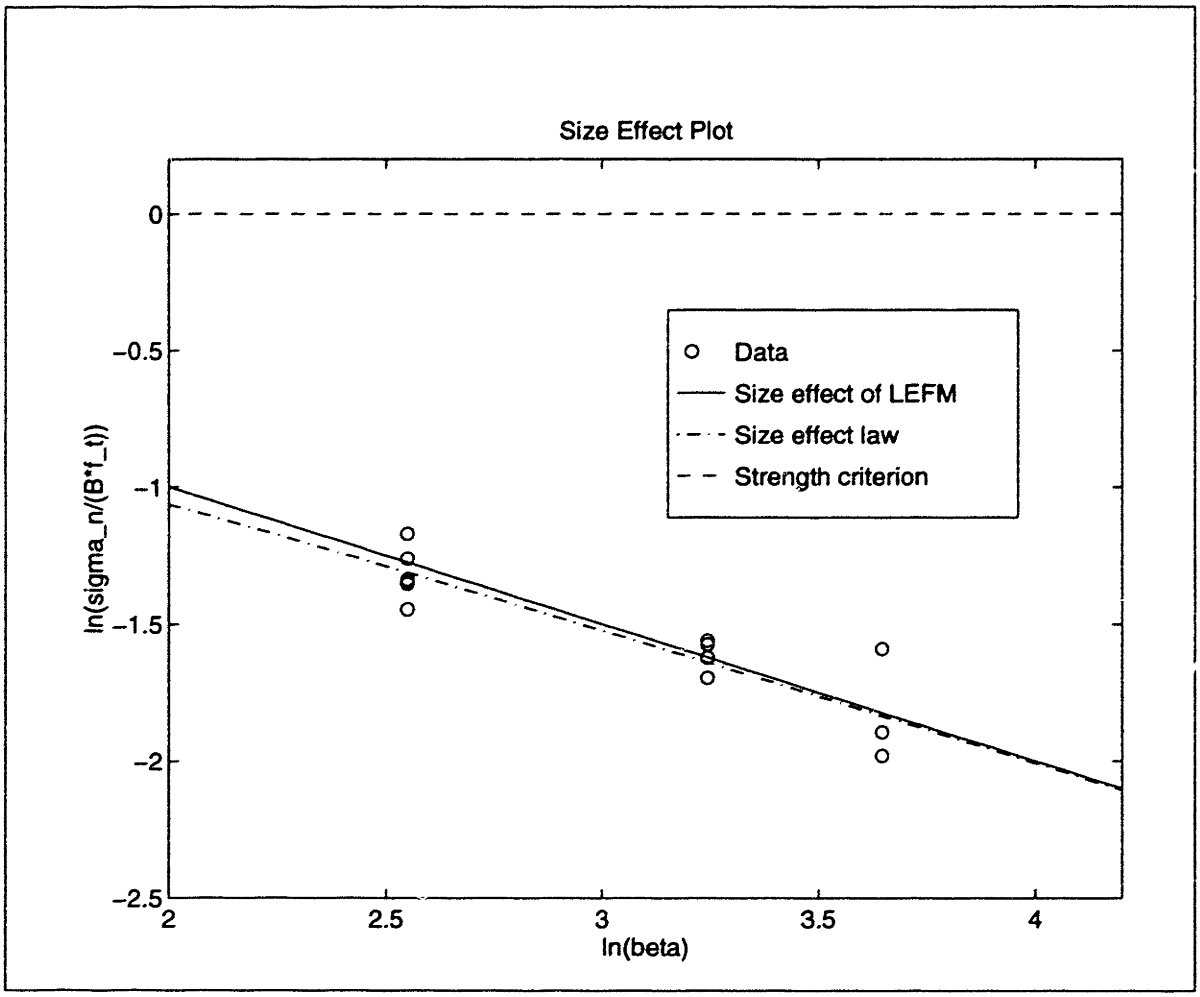

$A = 7.2646$, $C = 28.8465$, $B = 0.1862$
$c_n = 0.655$, $f_t = 5.375$ MPa, $d_0 = 3.9709$ mm

Figure 7-14: (contd.) Size effect plots for 81-MPa 7-day mortar/Mason (flamed) interface fracture in Mode I, Part 2

7.4 Results and Discussion

7.4.1 First Test Series (Phase 1)

- For a smooth Chelmsford/high strength concrete interface (12,000psi - 83 MPa), Lee [*Lee* (1993), p.123] reports a value for the apparent interface fracture toughness of $K_{IC} = 0.365$ MPa $m^{1/2}$. The values $K_{IC} = 0.32$ MPa $m^{1/2}$ obtained from the first test series are smaller but within a reasonable range. With the experience from these tests the manufacturing process of the specimens became more refined and higher values for the apparent interface fracture toughness were achieved. See below.

- The difference between the values for K_{IC} for the two rocks is very small, if detectable at all, although Mason and Chelmsford are two very different granites, with low and high compressive strength and Young's modulus, respectively.

- Increasing roughness lead to smaller or equal fracture toughness. One would expect an increase in the apparent interface fracture toughness K_{IC} with increasing surface roughness, but here the opposite is the case. The reason for this behavior can be found in an increased porosity at the interface. More trapped air voids result in less total bonding area, causing a smaller fracture load. However, the tests performed later on compact beams showed a slight increase in Mode I toughness and a strong increase for higher loading angles.

7.4.2 Second Test Series (Phase 2)

- The results of the tests performed on full–length sandwiched beams show an extremely large scatter. Only 37 out of 66 tests are considered valid because microcracks due to shrinkage, handling, and curing had been present at the interface before testing. Also, some tests are invalid because the crack did not start at the artificial crack tip. For example, the specimen broke on the wrong side of the aggregate or concrete failure occurred at the bearing.

- Because of the inferior quality of the test data, they were not used for further analysis. Only the data from the compact specimens was used to derive size effect data.

- The "new", or improved, loading geometry for the four–point mixed mode test appears to be much better. The changes have three main advantages: First, the failure loads required to fracture the interfaces are smaller, which results in more stable data. Second, possible concrete failure at the bearings due to the high loads is eliminated; and third, the greater distance of the main load[11] to the interface allows for a more uniform stress field at the interface and therefore results in more uniform test data. In addition, the kinking crack in high loading angles ends usually at the bearing of the main load, which calls for a large distance to let such a crack develop (see Figure 7-17).

- The differences in the fracture properties of the two aggregates Mason and Chelmsford granite are not detectable. Therefore, one granite was chosen to be used in the final test series (Phase 4): Mason granite. This granite represents a lower bound of granites in terms of compressive strength and Young's modulus.[12]

7.4.3 Final Test Series (Phase 4)

- The compact sandwiched specimen has proven useful for the determination of interface fracture properties in different loading angles. The data obtained from these tests is much more consistent, thus indicating that handling, curing, and thermal cracking problems had a strong influence on the results obtained from full–length beams.

- The tests show a strong size effect[13] for interface fracture of high–strength mortar/granite composites, independent of the aggregate roughness and loading

[11] The bearing of the loading arrangement closer to the interface. See Figure 6-4.
[12] See Table 6.3.
[13] With respect to the fracture loads

angle used.

- Increasing aggregate roughness leads to higher interface fracture energy. However, it appears that there is a trade–off among higher total surface area, trapped air voids, and roughness induced shielding in higher modes. While by going from smooth surfaces to sandblasted one the interface fracture energy values were about doubled in all loading angles, the fracture energy curve was shifted almost parallel by going from sandblasted surfaces to flamed ones, indicating a lower relative gain in higher loading angles (see Figure 7-1).

- Compared to the results obtained by Lee (1993) using the Brazilian disk specimen in mixed mode and the sandwiched four–point shear specimen in Mode I and 28–day mortars, the values for interface fracture energy in Mode I in this study (7–day mortar) are higher, while for higher loading angles, smaller values were obtained, resulting in a less steep fracture toughness curve. I believe that the data presented in this thesis is more valuable, since it uses the same specimen for all loading angles and is based on extensive testing.

- Using the concept of the brittleness number it can be justified to use linear elastic fracture mechanics instead of non–linear elastic fracture mechanics for the investigation of high–strength concrete interfaces.

- I expected no see trends in the brittleness number with increasing loading angle. However, as the results in Table 7.18 show, no consistent trend can be identified.

- Comparing interfaces made of 7–day and 28–day mortar of the about the same compressive strength, an increase of interface fracture energy of roughly 40% was observed. This leads to the conclusion that in early age high–strength mortar the strength is mainly provided by the cement paste, while in older mortar the strength is provided by the composite via stronger interfacial bonds.

- True interfacial fracture was obtained only for pure Mode I testing. The values for interfacial toughness and fracture energy reported for higher loading angles

can be considered lower bounds for the true interfacial properties because kinking of the crack occurred. For loading angles of $\phi = 30°$, the crack traveled along the interface until about midheight, where it kinked back into the mortar (see Figures 7-15 and 7-16). For loading angles of $\phi = 60°$, the crack traveled along the interface for a few millimeters before kinking back into the mortar (see Figure 7-17). The kinking always ended at the bearing of the main load, hence the kinking angle is determined by the loading geometry. Therefore, the standard criterion for crack kinking out of an interface cannot be used to predict the kinking angle [*Büyüköztürk et al.* (1992a)].

- The compact specimen yielded similar failure modes within each set of specimens, as can be seen in Figure 7-19.

- Similar failure modes were observed with all three sizes, which is required for the application of the size effect law, thus proving the compact shear beam specimen useful (see Figure 7-18).

- Although kinking occurs in higher loading angles, the interface usually fractures also. A typical interface with the triangular block of mortar taken off the aggregate slice is shown in Figure 7-20, indicating that only little mortar bonds strongly to the granite.

- In pure Mode I, very little or no mortar remains on the fractured interface.

- An increase in mortar porosity was observed with increasing aggregate roughness, as shown in Figure 7-22. This can be attributed to trapped air voids at the interface that cannot be removed with tapping or vibrating of the fresh mortar. This observation leads to the conclusion that the influence of increasing aggregate roughness on interfacial strength is a tradeoff among available surface area, increasing porosity, and roughness induced shielding. Details of the porosity of mortars bonded to sandblasted and flamed Mason granite are shown in Figures 7-23 and 7-24, respectively.

- In Figure 7-25, a fractured sample of high–strength mortar is shown. Transgranular fracture (through sand particles) indicates a strong mortar/sand interface.

7.5 Results of the Microscopical Investigation

Using a scanning electron microscope, samples of previously tested beams were investigated. Figures 7-27 to 7-29 show a polished granite/high–strength mortar interface in increasing magnification. The granite/mortar interface appears not well defined in high magnifications. Shrinkage and thermal cracks are highly visible. Figure 7-26 shows a macrocrack traveling through aggregate and mortar. A detail of mortar previously bonded to epoxy and granite is shown in Figure 7-30. The mortar cast against the epoxy is very smooth, showing no indication of bond to the epoxy. In Figure 7-31, a detail of mortar bonded to granite is shown. Note the cracks originating at the macropore. A crack kinked back into the rock (in a test with switched sides, see Fig. 6-6) is shown in Figure 7-32. Note the mortar cast against epoxy at the top, also in Figure 7-33, which shows the difference in the appearance of mortar at the crack tip. Note the cracks, which were causes by the fracture of the interface but propagate away from the interface. Figure 7-34 shows a detail of a mortar interface to which granite was bonded. Some granite particles can be seen left on the mortar after fracture. Also, a typical pore diameter is indicated as 692 μm. A crack propagating along a granite/mortar interface and eventually kinking back into the mortar is shown in Figure 7-35. Note the secondary cracks in the granite and mortar. Shrinkage cracks between sand particles and mortar can be seen in Figure 7-36. The cracks in Figure 7-37 are secondary cracks caused by near fracture. They propagate along a sand particle and eventually continue to propagate in the mortar (top left). The bridging of two approaching microcracks by mortar is shown in Figure 7-38. Such bridging is important for a material's ductility. In Figure 7-39, the disturbed interfacial zone with a higher porosity between granite and mortar is shown. The approximate width is 90 μm.

7.5.1 X–Ray Diffraction Analysis of Interfacial Zone

It is difficult to obtain reliable data regarding the width of the interfacial zone from microscopical examination of specimens. A more thorough investigation of the transitional nature of the interfacial zone is possible using X–ray diffraction techniques. In Figures 7-40 to 7-42, the results of an X–ray analysis is shown. The analysis was made using the X-ray analysis of backscattered electrons, a feature of the above described scanning electron microscope (Sec. 6.3.1). The analysis was performed at a distance of 1 μm, 20 μm, and 45 μm from a 60 day old interface between a high–strength silica fume mortar and a sand particle. The analyzed area was a square of approximately 1 μm width. With increasing distance from the interface the relative amounts of silica and potassium decrease while the relative amounts of aluminum, calcium, and iron increase. It was observed that a relative sharp drop of the silica content occurred at a distance of about 20μm, thus indicating the width of the interfacial zone. Note that the amount of gold can be taken as a reference value, since the specimens were gold coated to enhance image quality. The X–ray analysis confirms results obtained by other researchers investigating the interfacial zone [*Maso* (1992), *Alexander et al.* (1992b), *Mehta et al.* (1990)]

7.6 Problems in the Measurement of Interface Fracture Parameters

It is difficult to obtain reliable data for interface fracture. The results depend on a large number of parameters. Since there is no generally accepted test for interface fracture properties, researchers will arrive at different results with different specimens and test procedures. It should be noted that there is a strong dependence of interfacial data on the width of the specimens. On the specimens used in this study, a different appearance of the zones that were closer to the outside of an interface was observed. A strip of about 2 mm at each of the long sides of the rectangular aggregate slice showed signs of less good bond to the mortar. It was also observed that the width

of these zones was approximately constant with increasing specimen size. Therefore, the size effect was rather underestimated than overestimated. The zones are believed to result from higher mortar porosity as a result of low compaction at the top of the mold and grease and segregation at the bottom of the mold, respectively. Specime

ns of equal width for different sizes would probably exhibit an even stronger size effect. There is also a dependence of the interface fracture results on the relative crack length a/d. Investigations by Lee [*Lee* (1993),] indicate that the fracture toughness increases with decreasing relative notch depth. Also, the loading rate has an effect on the results.

The large scatter observed on full–length beam specimens was greatly reduced to a scatter of about 30% at maximum.[14] However, such a scatter requires a large amount of tests to ensure proper results. Consequently, the investigation of interface fracture is generally more elaborate than other fracture studies.

Other problems include bleeding, which is essentially unavoidable, and shrinkage, which caused microcracks that can be partially filled by autogeneous healing. However, these microcracks (shown below in micrographs) significantly affect the interfacial properties, and consequently, consistent preparation procedures are essential. Finally, one must ask how well the used interface specimens resemble interfaces in real concrete, where even more factors such as segregation, composition, heat of hydration influence the interface. Therefore, the results for interfacial properties will always depend on the details of the specimen and its preparation.

[14]Extremes not included.

Figure 7-15: Typical failure of a specimen with a loading angle of $\phi = 30°$ (large compact specimen)

Figure 7-16: Characteristic appearance of fractured interface of the specimen above

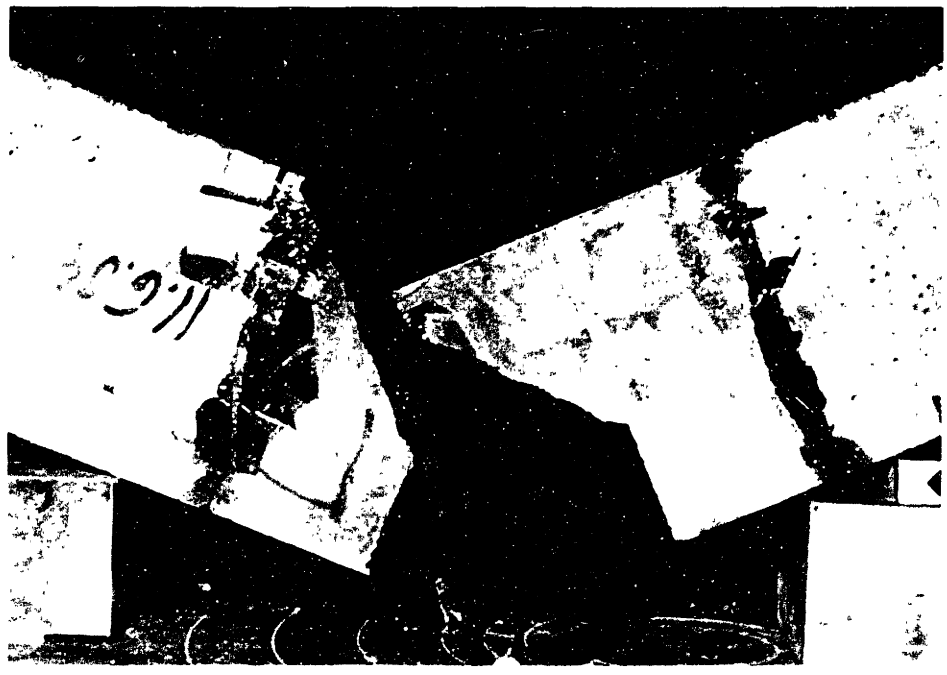

Figure 7-17: Typical failure of a specimen with a loading angle of $\phi = 60^{\circ}$ (medium compact specimen)

Figure 7-18: Example for the similarity of the failure modes of specimens of all three sizes

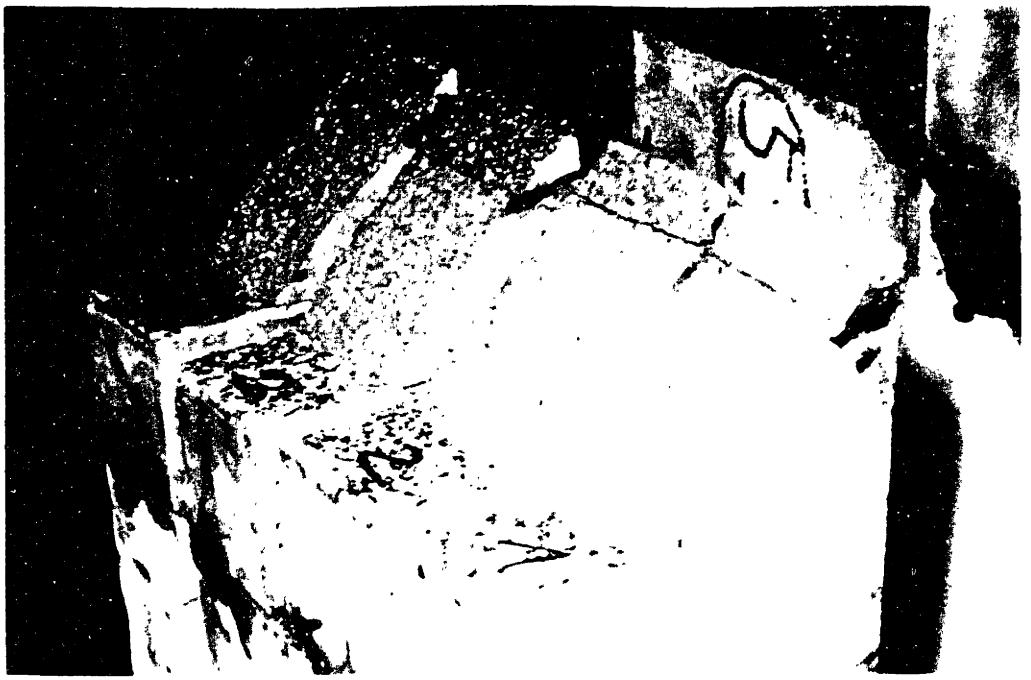

Figure 7-19: Similarity of failure of specimens within one size (medium beams with $\phi = 60°$). Note that the kinking crack traveled across the epoxy joint to the location of the main load

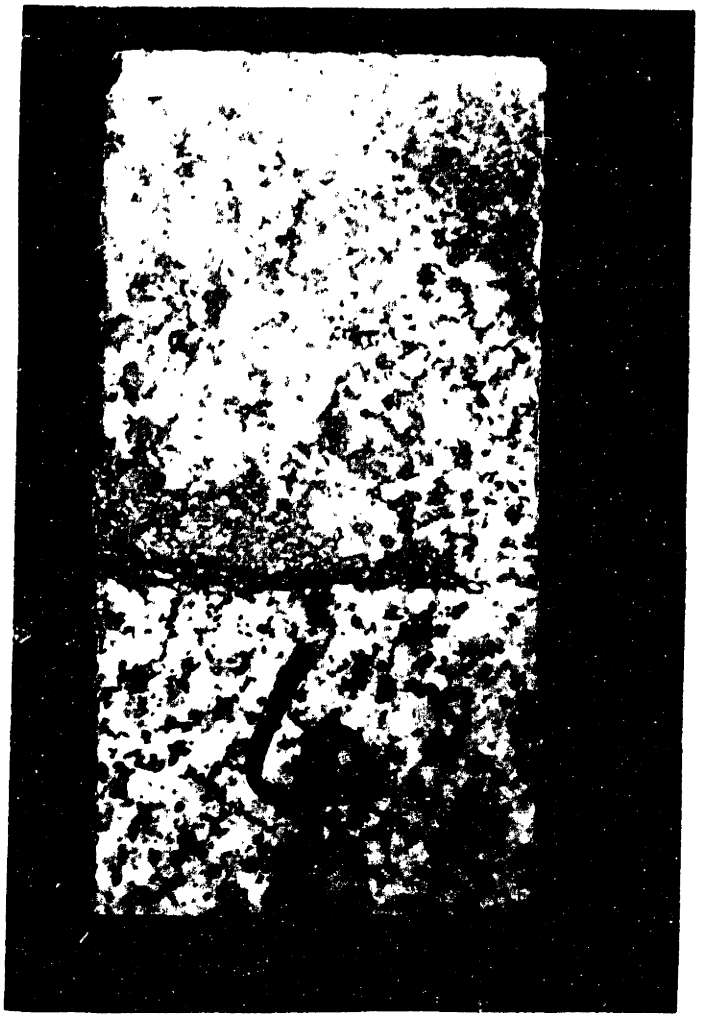

Figure 7-20: Typical interface of a fractured compact specimen in higher loading angles (same specimen No. 4 as in the above Figure)

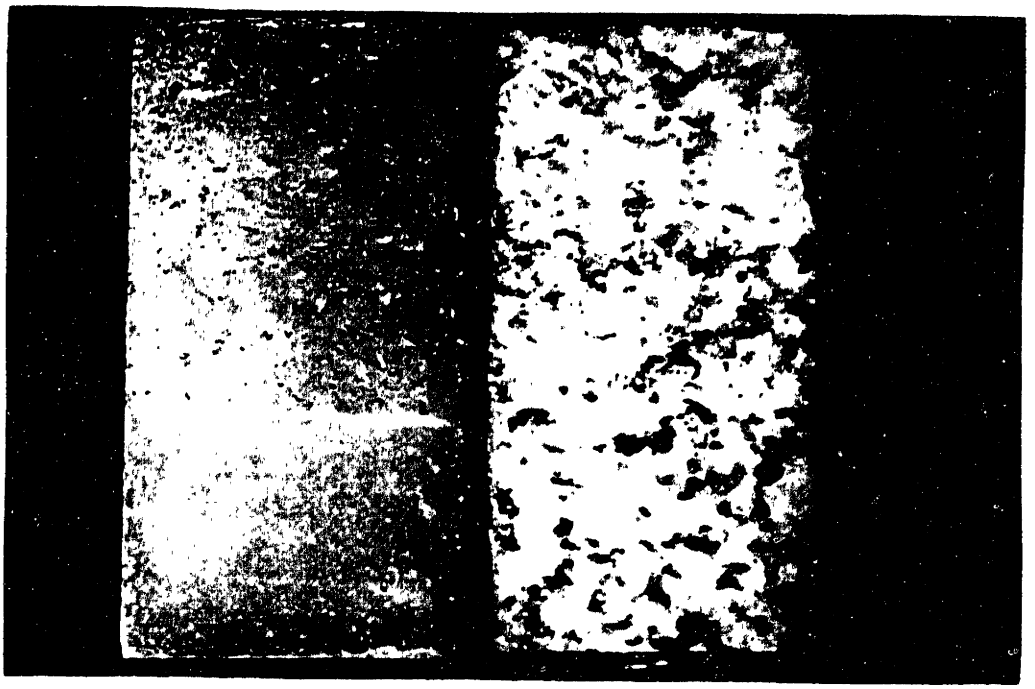

Figure 7-21: Typical appearance of interface after pure Mode I fracture (small specimen, sandblasted Mason granite)

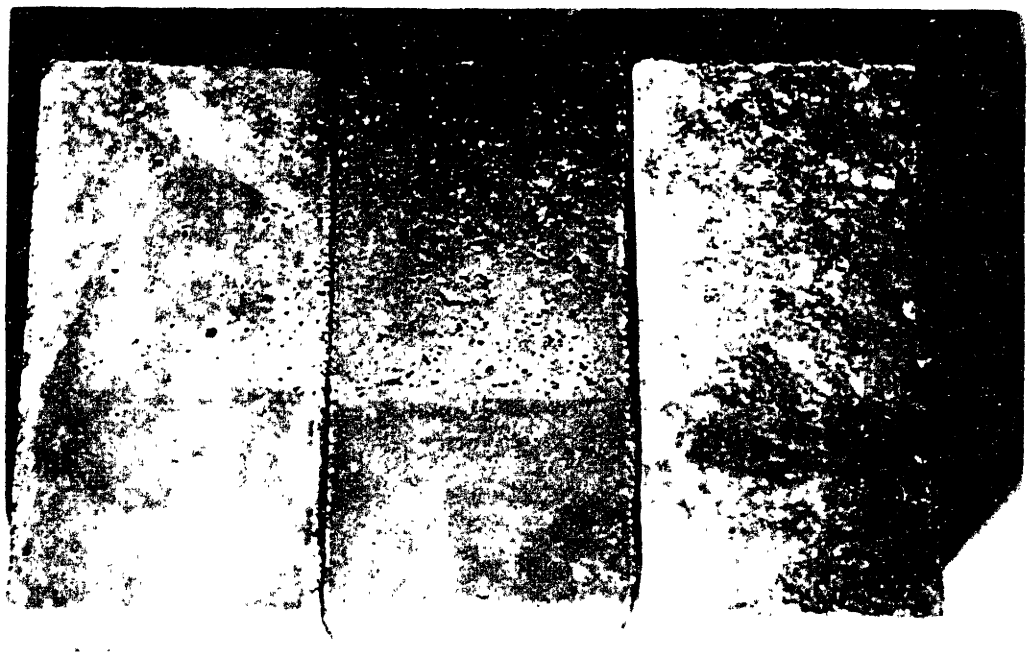

Figure 7-22: Comparison of mortar surfaces previously bonded to Mason granite of different roughness (from left to right: smooth, sandblasted, flamed, large specimens). Note the flakes of granite bonded to the mortar of the specimen on the right.

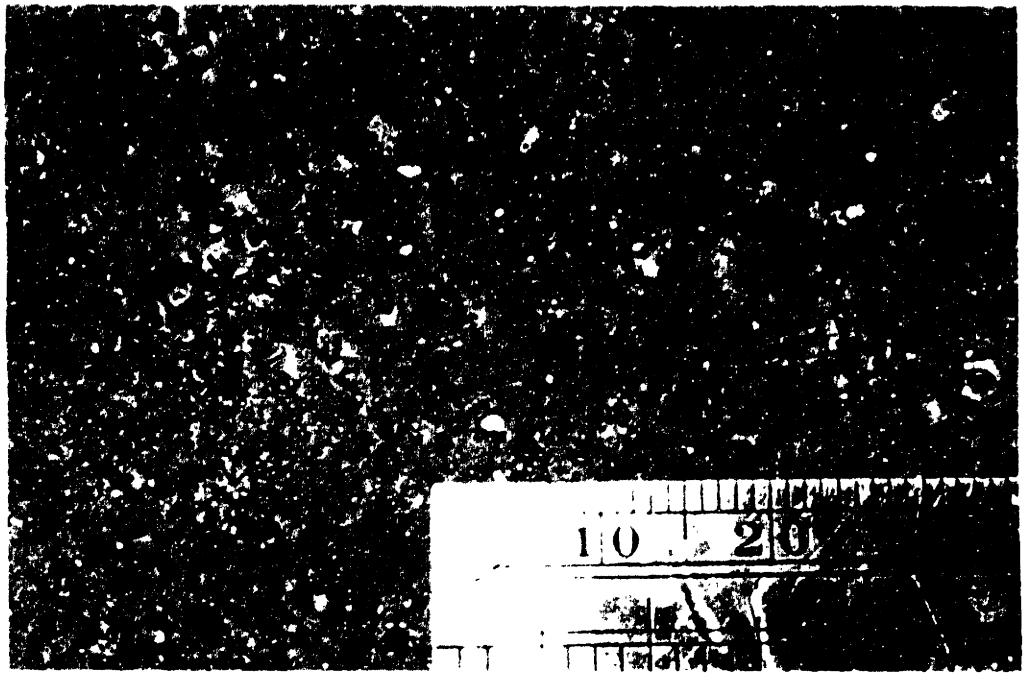

Figure 7-23: Detail of mortar previously bonded to a sandblasted surface of Mason granite

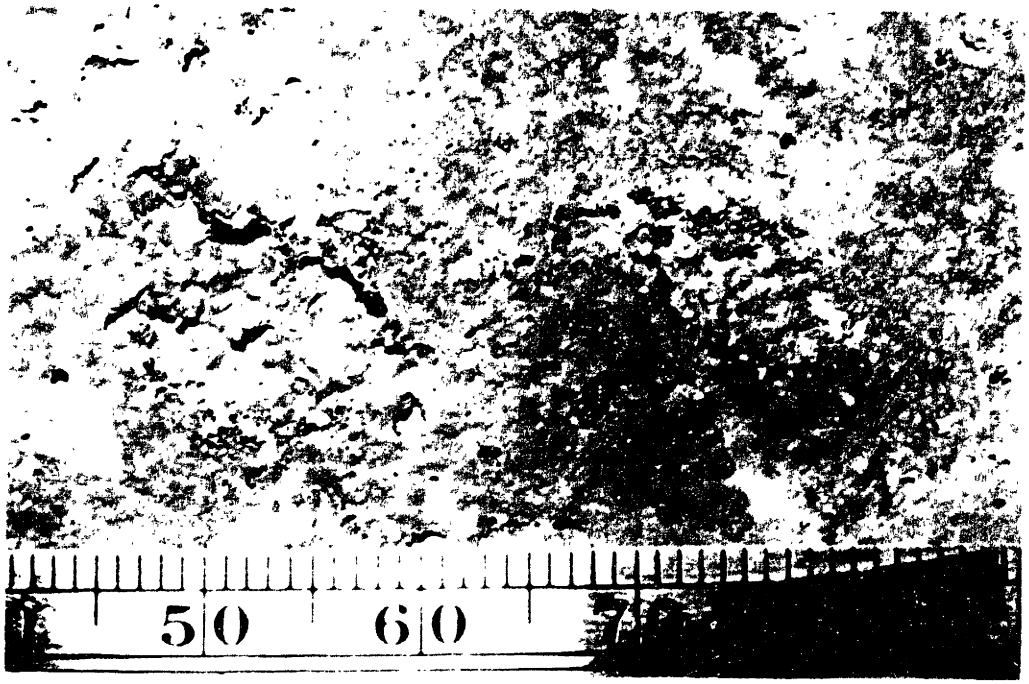

Figure 7-24: Detail of mortar previously bonded to a flamed surface of Mason granite

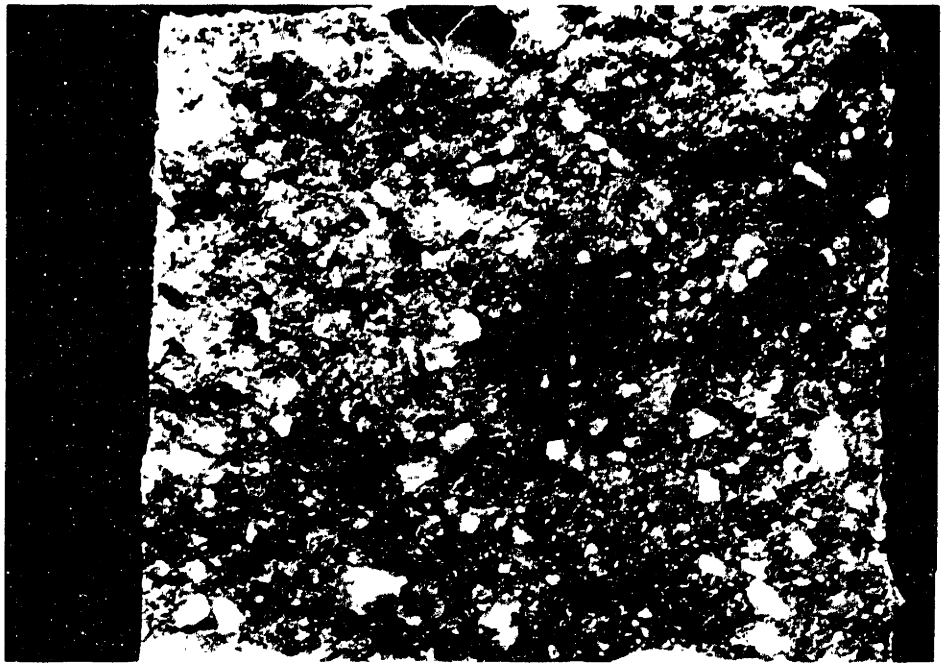

Figure 7-25: Fractured high strength mortar, showing the crack propagating through sand particles and pores of various sizes (width of sample 2.54 cm).

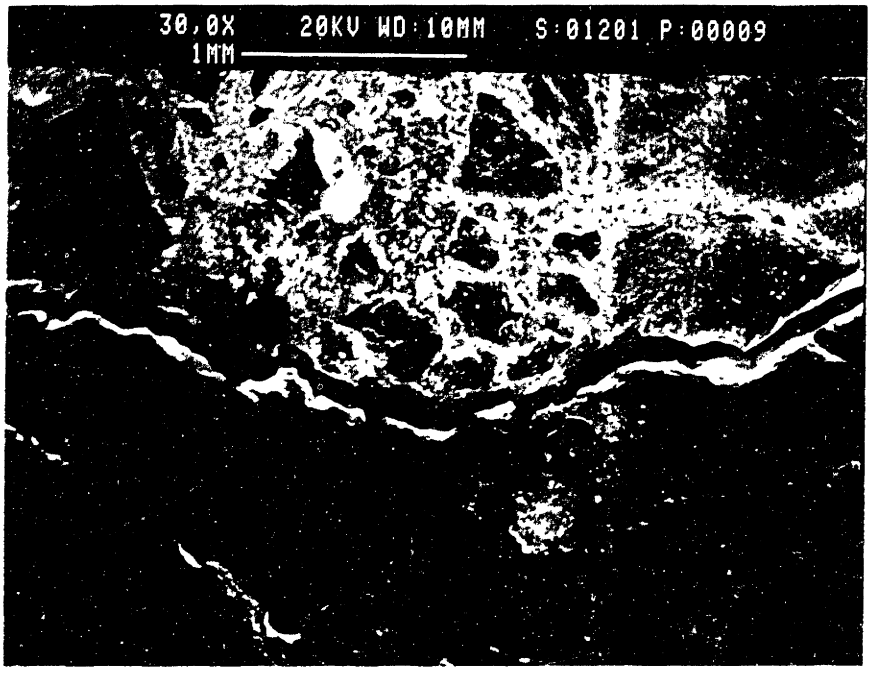

Figure 7-26. Macrocrack through aggregate (right) and mortar (left). Note the smaller cracks branching away from the main crack.

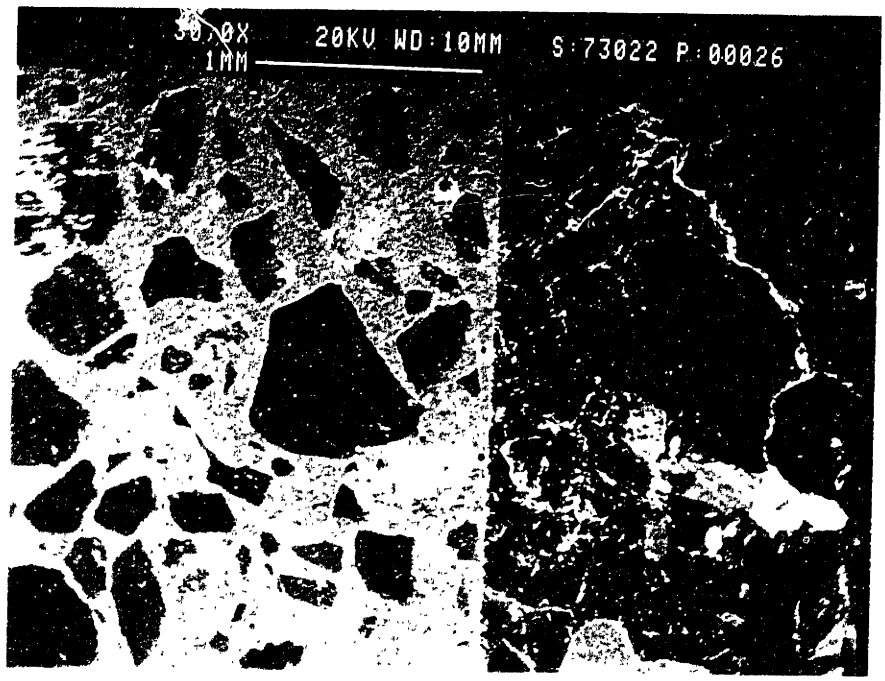

Figure 7-27: (1) Mortar/granite interface at low magnification. Note the pores in the mortar at left and the crystal structure in the granite at right.

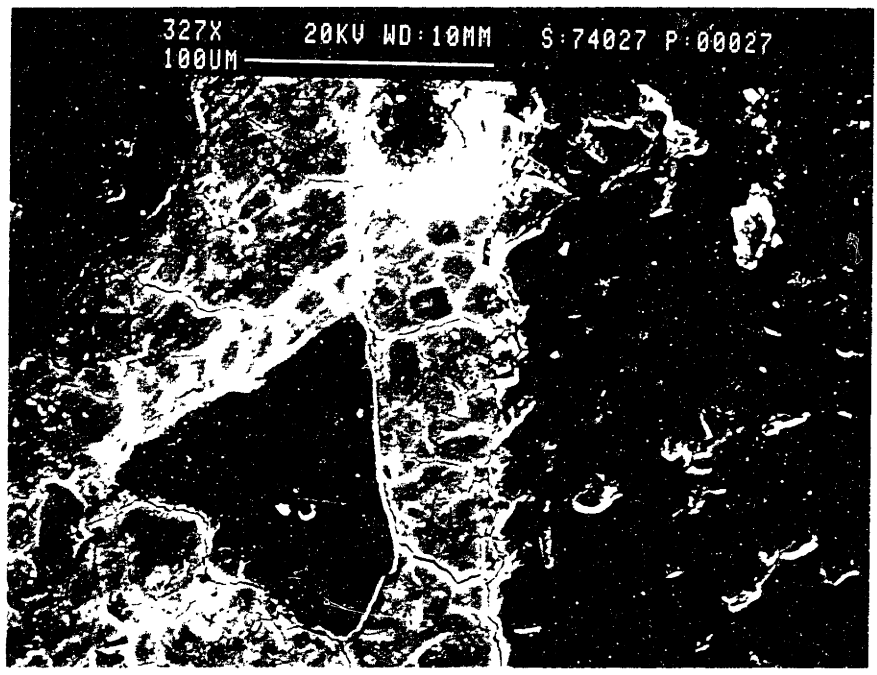

Figure 7-28: (2) Mortar/granite interface at medium magnification. Note the shrinkage cracks in the mortar at left and the rough interface to the granite at right.

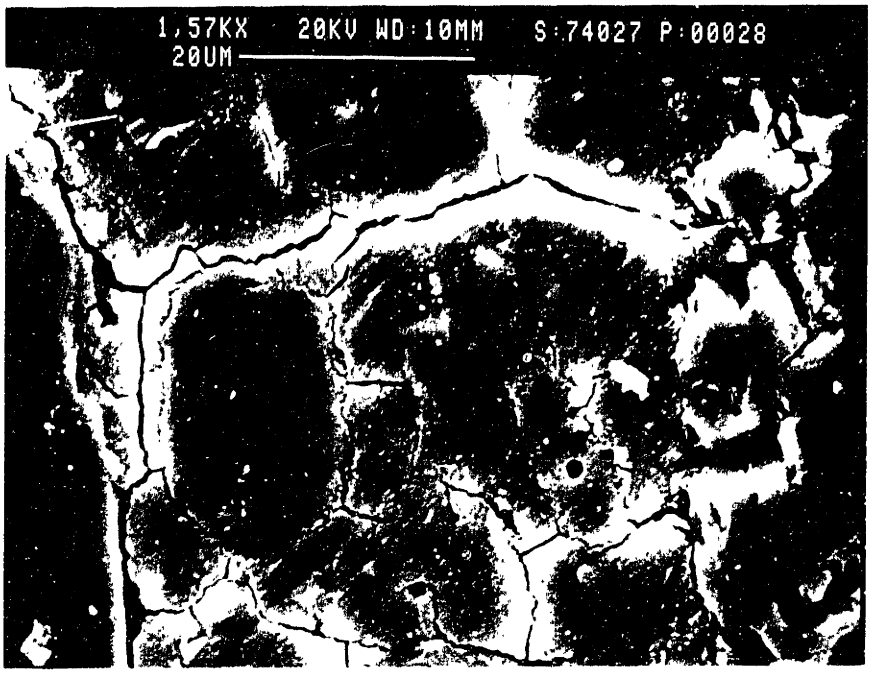

Figure 7-29: (3) Mortar/granite interface at high magnification. Shrinkage cracks are clearly visible. Also note the appearance of the interface to the granite (right).

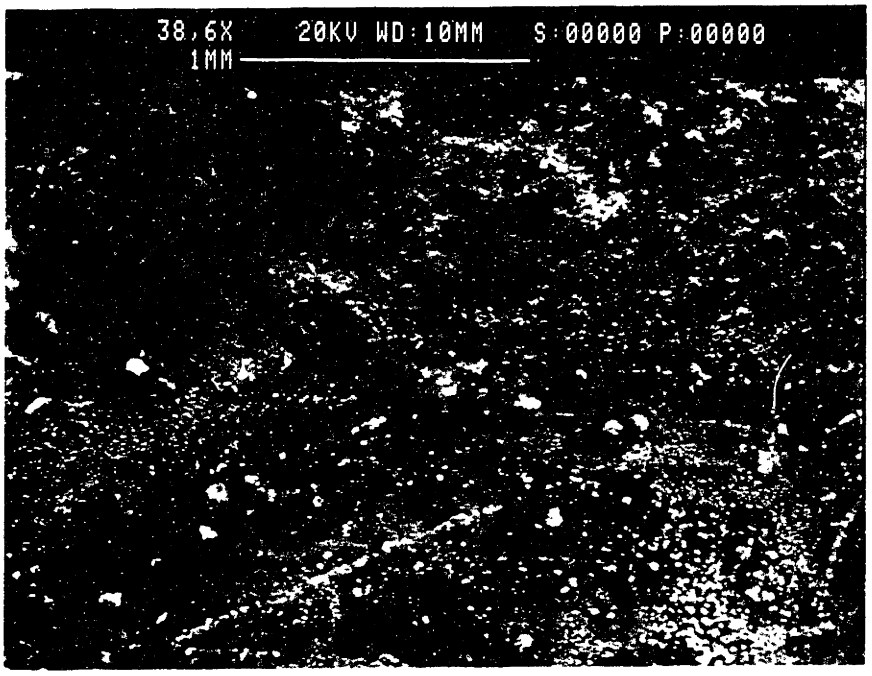

Figure 7-30: Detail of mortar that was cast against epoxy (bottom) and granite (top)

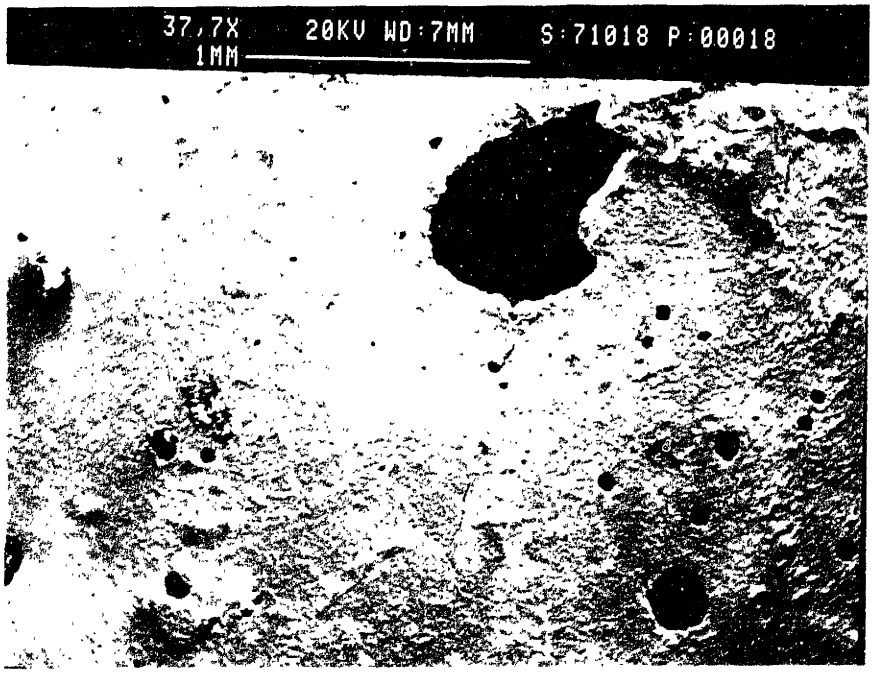

Figure 7-31: Detail of mortar previously bonded to smooth granite. Note the cracks originating at the pore.

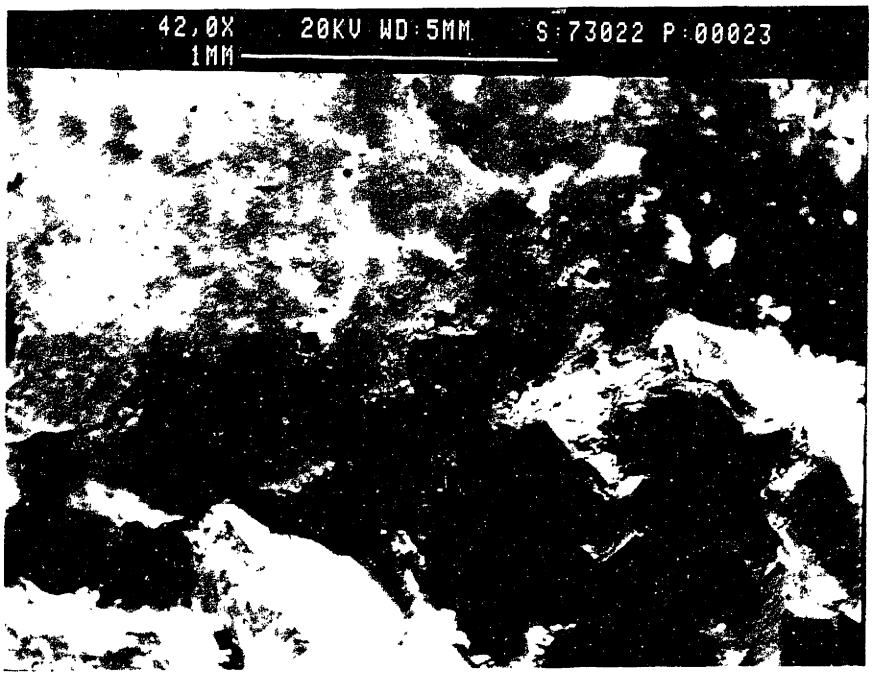

Figure 7-32: Mortar interface (top) and crack kinked back into the granite (bottom)

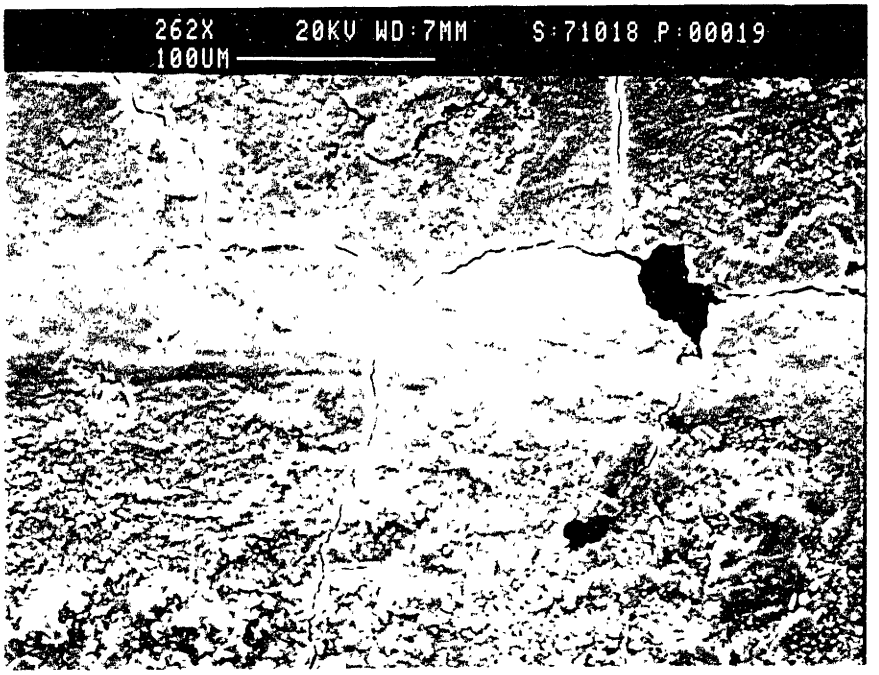

Figure 7-33: Mortar in the vicinity of the epoxy crack tip (midheight, epoxy was at the top)

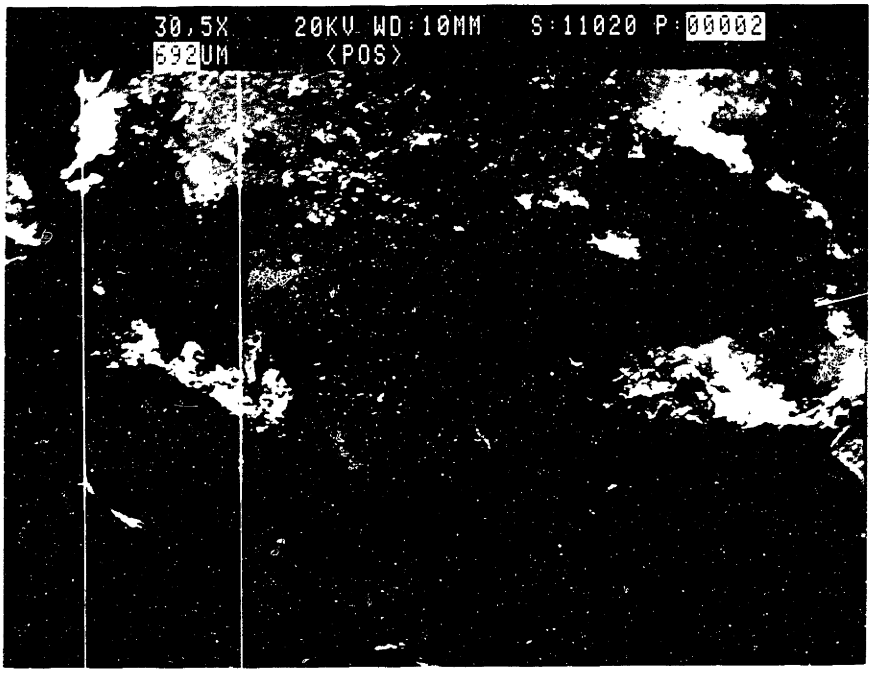

Figure 7-34: Mortar surface showing granite particles bonded to it after fracture

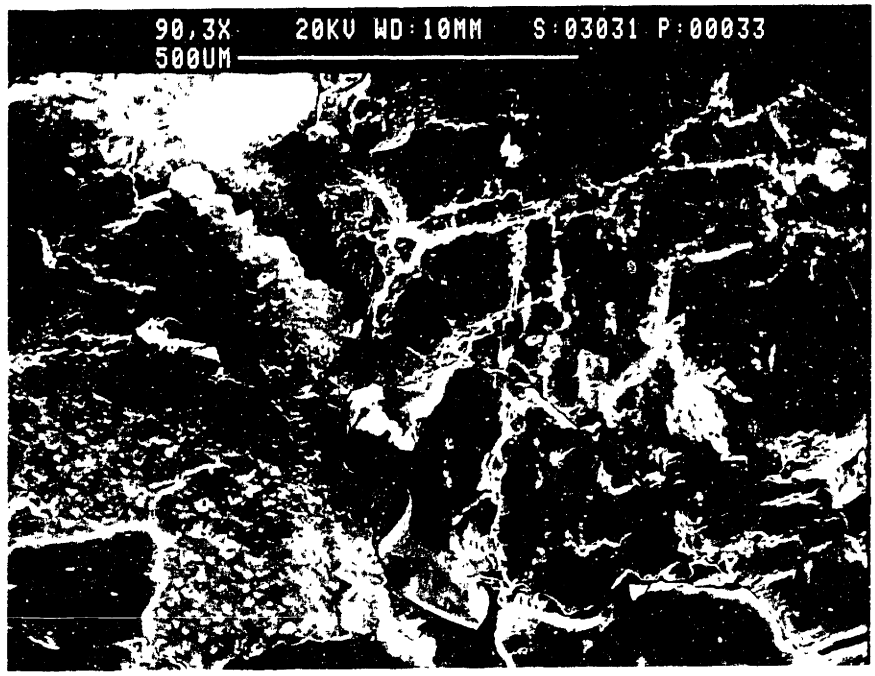

Figure 7-35: Polished granite/mortar interface, showing a crack propagating along the interface and then kinking back into the mortar. Also, note the many secondary cracks in the mortar and granite.

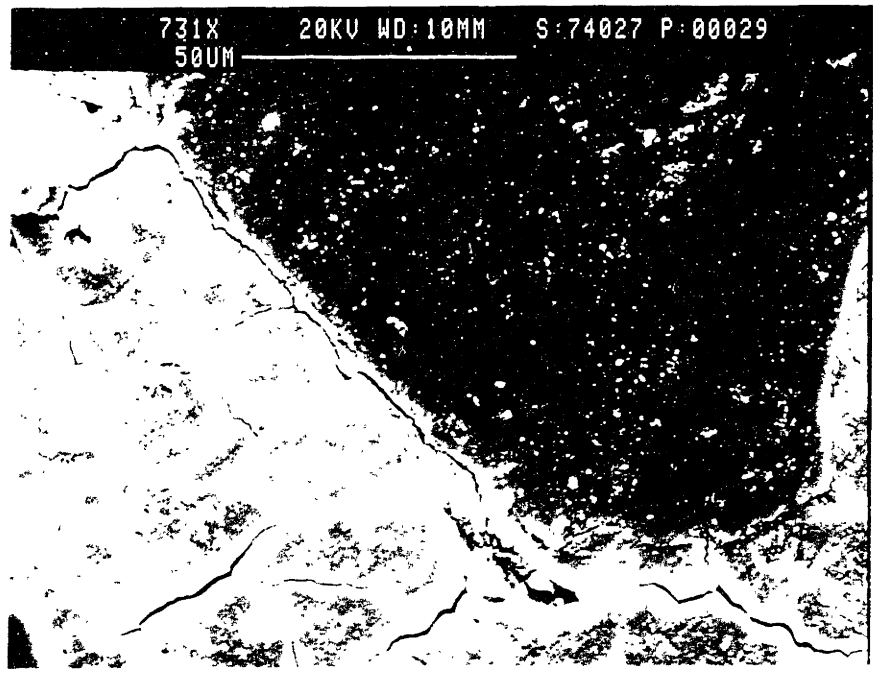

Figure 7-36: Shrinkage cracks in mortar (below) and along interface with sand particle (top)

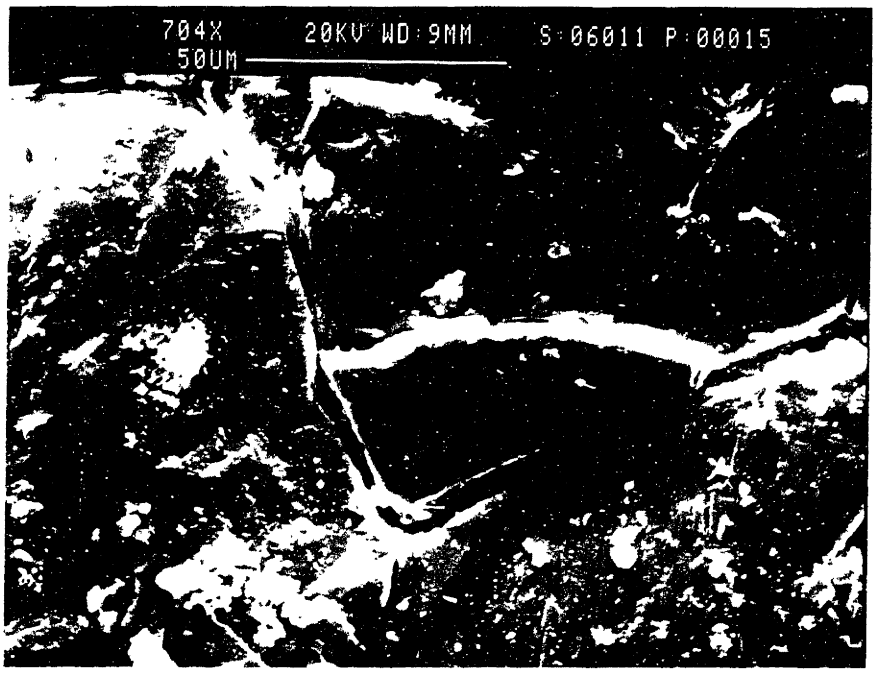

Figure 7-37: Secondary cracks caused by nearby energy release into macrocrack. Note that the crack travels along the sand particle until it kinks back into the mortar (top left). Also note the mortar crack originating at the stress singularity at the tip of the sand particle.

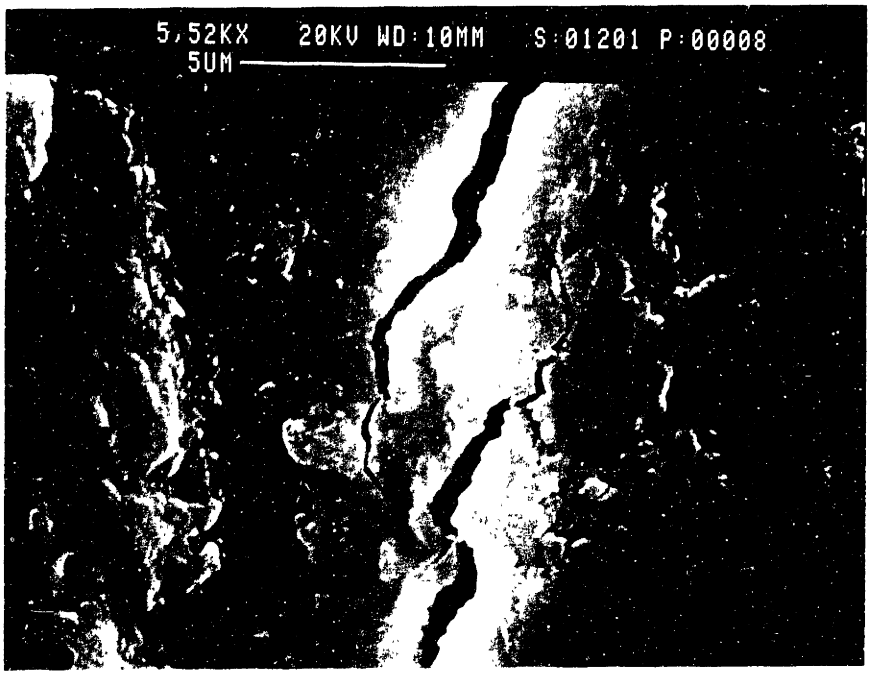

Figure 7-38: Two approaching microcracks bridged by mortar

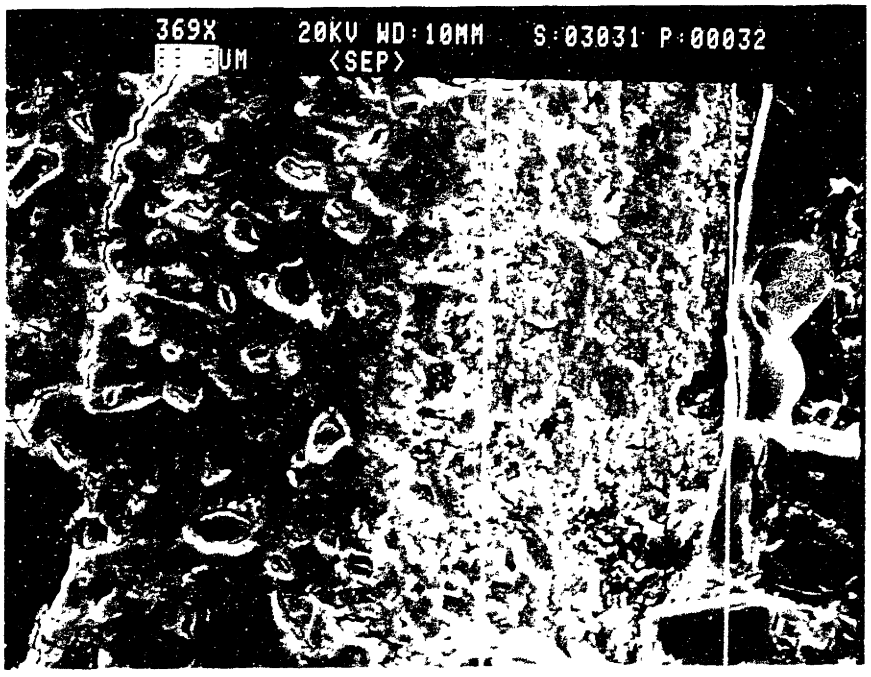

Figure 7-39: Interface between granite (right) and mortar, showing a disturbed zone with irregular appearance and higher porosity of about 90 μm width.

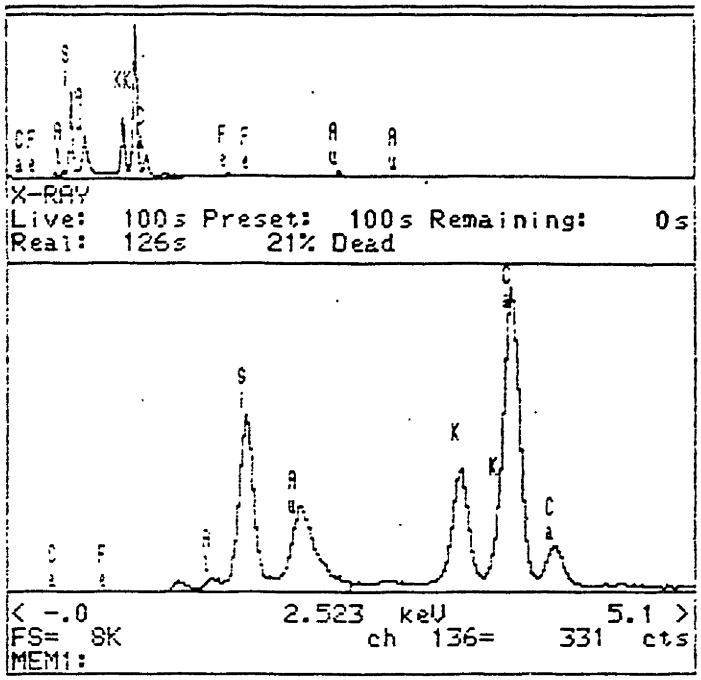

Figure 7-40: X–ray diffraction analysis of high–strength mortar at a distance of 1μm from an interface with a sand particle

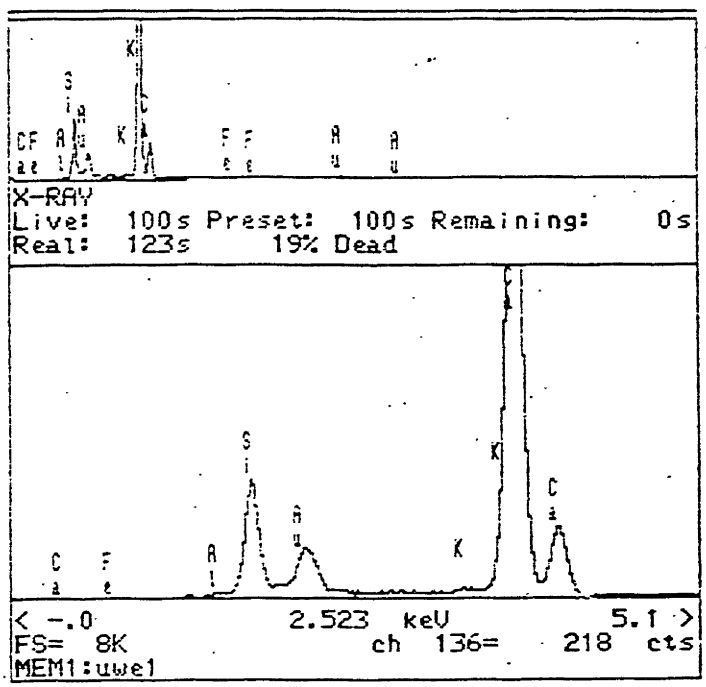

Figure 7-41: X–ray diffraction analysis of high–strength mortar at a distance of 20μm from an interface with a sand particle

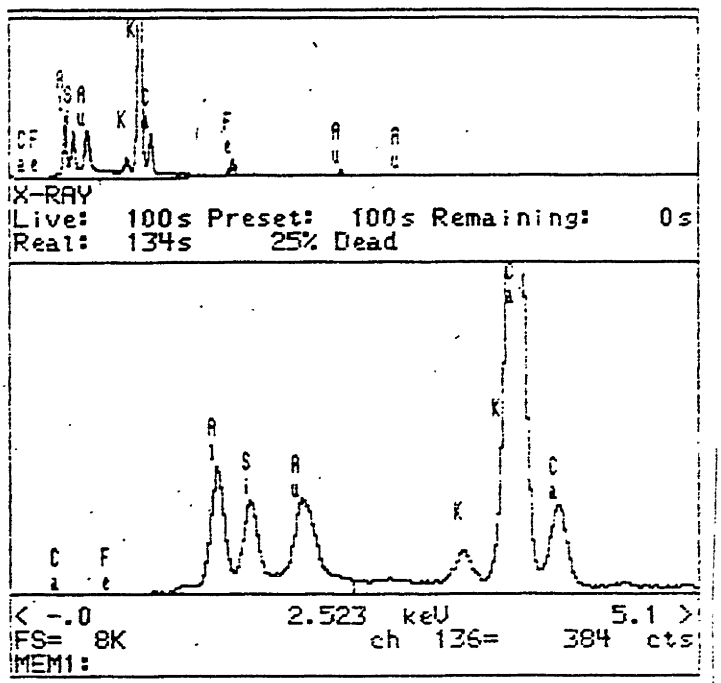

Figure 7-42: X–ray diffraction analysis of high–strength mortar at a distance of 45μm from an interface with a sand particle

Chapter 8

Summary, Conclusions, and Future Work

8.1 Summary

A fundamental study on interfacial fracture of high–strength mortar/aggregate composites as a model for high–strength concrete was performed. An analysis based on energy release rate concepts was used to compute interface fracture parameters from tests on sandwiched beam specimens. The beam specimens consisted of a layer of granite bearing epoxy resin as an artificial crack embedded in high–strength mortar and were tested using either a symmetric four–point bending set–up for Mode I or an asymmetric four–point shear set–up for mixed mode. The tests were performed using three different loading angles, a measure of the contribution of Mode I vs. Mode II, at about 0° (pure Mode I), 30°, and 60°. The specimen sizes for the investigation of the size effect were in the ratio of 1:2:3. Three different aggregate roughnesses were used: smooth (diamond saw cut), sandblasted, and flamed.

The compact beam specimen was developed in this study. It is essentially an improvement of the previously used sandwiched beam specimen. For the compact specimen, only the central portion incorporating the aggregate layer is cast, cured, and glued to previously cast mortar beams before testing.

The fracture loads of the tests on compact sandwiched were used to investigate

the size effect in interface fracture of high–strength mortar/granite interfaces as an example for interface fracture in high–strength concrete. At the same time, parameters such as interface fracture toughness k and energy release rate G_f were derived for each specimen. More than 230 specimens were tested.

8.2 Conclusions

8.2.1 Conclusions with Respect to the Size Scale Effect

- The tests show a strong size effect[1] for interface fracture of high–strength mortar/granite composites, independent of the type of granite, aggregate roughness, and loading angle used.

- For high–strength mortar/Mason granite interfaces with a height of 50.8 mm or more, failure can generally be calculated according to linear elastic fracture mechanics (LEFM).[2]

- The size effects exhibited by the specimens used in this study comply well with the size effect law proposed by Bažant [*Bažant* (1992)].

- For varying loading angles[3] with the same material combination,[4] large differences in the size effect parameters were obtained (see Table 7.18). This is mostly due to experimental scatter, however, the evaluation of the brittleness number as proposed by Bažant (1992) is extremely sensitive the results of the regression analysis of the test data. It is not justified to conclude that the higher the loading angle, the more brittle the interface.

[1] With respect to the fracture loads

[2] Because the smallest brittleness number was in general larger than 10.

[3] The loading angle expresses the ratio of pure opening to pure shear at the interface.

[4] For example, sandblasted Mason granite/7–day 81 MPa mortar or smooth Mason/28-day 83 MPa mortar.

8.2.2 Conclusions with Respect to the Influence of Aggregate Roughness and Type

- Increased aggregate roughness leads to increased interface fracture energy.
- It can be concluded from the fracture toughness curves that roughness induced shielding is responsible for the increase in fracture energy with increasing loading angle [*Hutchinson et al.* (1992)].
- In going from smooth to flamed surfaces the interface fracture energy is about tripled for loading angles between 0 and 60°. While the total available bonding area increases with increasing roughness, more and larger pores are created, thus reducing the possible bonding area. (See Figure 4-5.) However, as a result of the shielding effect, increased roughness leads to increased fracture energy at higher loading angles.
- No significant differences in interface fracture energy were obtained from the tests on Chelmsford and Mason granite, though they represent a strong and a weak granite, respectively

8.2.3 Conclusions with Respect to Interface Fracture Parameters

- Using the concept of the brittleness number, it can be justified to use linear elastic fracture mechanics instead of non–linear analysis to fully describe interface fracture problems in high–strength concrete composites.
- Two sets of specimens using 7–day and a 28–day mortar with almost identical compressive strength and Young's modulus were compared using the same aggregate and roughness. The results show an increase of roughly 40% in interface toughness for the 28–day mortar set. This can be mainly attributed to the pozzolanic reaction of condensed silica fume, which becomes noticeable only at later stages of hydration but has generally been considered less important

compared to the filler action of mineral admixtures. It leads to the conclusion that in early age high–strength mortar the strength is mainly provided by the cement paste, while in older mortar the strength is provided by the composite via stronger interfacial bonds.

- The interface fracture parameters obtained in this study compare well with data obtained by Lee, who used sandwiched beam specimens in Mode I and Brazilian disk specimens in higher loading angles and a comparable material combination [*Lee* (1993)], and others [*Alexander et al.* (1992b)]. However, compared to Lee, higher values for interface fracture toughness K and fracture energy G_f were found in Mode I, which is mostly due to the use of the compact beam specimen and a refined manufacturing procedure, and smaller values were found for higher loading angles, which is attributed to the different test specimens.

- It should be noted that although the fracture of interfaces made of high–strength mortar and granite shows a pronounced size effect, the fracture energy of the specimens of different sizes stays almost constant. This shows the validity of the performed tests, since the fracture energy should decrease only slightly with specimen size approaching infinity.

8.2.4 Conclusions with Respect to the Compact Specimen

- The compact sandwiched test specimen, which was specially designed is this study, has proven useful for the testing of interface fracture properties. The test results are greatly improved compared to standard sandwiched beam specimens because the influences of handling, thermal cracking, and storage could be drastically reduced.

- It is suggested to consider the compact specimen as a specimen for a standardized interface fracture test. This specimen has the following advantages: it is small, can be used in pure Mode I and mixed mode, requires only minimal testing equipment, and can easily be produced in large quantities to ensure

representative test results. The suggested size is the medium beam (10.16 cm height).

8.3 Recommendations for Future Work

The future work should involve the following studies:

- Develop appropriate composite beam models and study the influence of changes in the interface properties on the global behavior,
- Study of crack propagation scenarios on composite beams with circular inclusions having different relative material properties; identify major fracture mechanics parameters influencing different crack paths,
- Investigate the real concrete behavior with altered interface characteristics, correlate the results with those from composite model studies, and make recommendations for the design of high performance concrete.
- Perform numerical investigations on crack propagation
- Further compare 7–day and 28–day interfaces made of mortars with about the same compressive strengths.
- Correlate the size effect in normal strength mortar/granite interface fracture to the size effects observed in this study.

Bibliography

[*209* (1978)] ACI Committee 209. Prediction of creep, shrinkage, and temperature efefcts in concrete structures. *American Concrete Institute*, 1978.

[*226* (1987)] ACI Committee 226. Silica fume in concrete. *ACI Materials Journal*, 84:158–166, 1987.

[*363* (1984)] ACI Committee 363. State–of–the art report on concrete. *ACI Materials Journal*, 81:363–411, 1984.

[*Addis et al.* (1990)] B. J. Addis and M. G. Alexander. A method of proportioning of high–strength concrete. In W. T. Hester, editor, *High–Strength Concrete*, volume ACI, SP-121 of *Second International Symposium on Utilization of High Strength Concrete, Berkeley, California, May*, pages 287–308, May 1990.

[*Ahmad et al.* (1987)] S. H. Ahmad and S. P Shah. High strength concrete – a review. In *Utilization of High Strength Concrete*, pages 255–269. Tapir, 1987.

[*Aïtcin et al.* (1990)] P. C. Aïtcin and P. K. Mehta. Effect of coarse aggregate type on mechanical properties of high–strength concrete. *ACI Materials Journal*, 1990.

[*Alexander et al.* (1992a)] M. G. Alexander, S. Mindess, and L. Qu. The influence of rock and cement types on the fracture properties of the interafacial zone. In *Interfaces in Cementitious Composites*, volume 18 of *RILEM Proceedings*, pages 129–137, 1992.

[*Alexander et al.* (1992b)] M. G. Alexander, S. Mindess, and Lie Qu. The influence of rock and cement types on fracture properties of the interfacial zone. In J. C. Maso, editor, *Interfaces in Cementitious Composites*, RILEM Proceedings 18, Toulouse, pages 129–138. E & FN Spon (Chapman & Hall), Oct. 1992.

[*Bažant* (1984)] Z. P. Bažant. *Journal of Engineering Mechanics*, 4:518–535, 1984.

[*Bažant* (1985)] Z. P. Bažant, editor. *Mechancis of Geomaterials*. Wiley, J. and Sons, London, 1985.

[*Bažant* (1986)] Z. P. Bažant, editor. *U.S.–Japan Seminar on Finite Element Analysis of Reinforced Concrete Structures, New York*. American Society of Civil Engineers, 1986.

[*Bažant* (1987)] Z. P. Bažant, editor. *SEM/RILEM Int. Conference on Fracture of Concrete and Rock*. Society for Experimental Mechanics, 1987.

[*Bažant* (1992)] Z. P. Bažant. Fracture mechanics of concrete: Concepts, models and determination of material properties. In *Fracture Mechanics of Concrete Structures*, ACI Committee 446, Fracture Mechanics, pages 3–144. Elsevier Applied Science, 1992.

[*Bažant et al.* (1986)] Z. P. Bažant and Z. Cao. Size effect in shear failure of prestressed concrete beams. *ACI Materials Journal*, 83:260–268, 1986.

[*Bažant et al.* (1987)] Z. P. Bažant and Z. Cao. Size effect in punching shear failure of slabs. *ACI Structural Journal*, 84:44–53, 1987.

[*Bažant et al.* (1988a)] Z. P. Bažant and S. Sener. Size effect in pullout tests. *ACI Materials Journal*, 85:347–351, 1988.

[*Bažant et al.* (1988b)] Z. P. Bažant, S. Sener, and P. C. Prat. Size effect tests of torsional failure of plain and reinforced concrete beams. *Materials and Structures*, 21:425–430, 1988.

[*Bažant et al.* (1990a)] Z. P. Bažant and M. T. Kazemi. Determination of fracture energy, process zone length and brittleness number from size effect, with application to rock and concrete. *International Journal of Fracture*, 44:111–131, 1990.

[*Bažant et al.* (1990b)] Z. P. Bažant and M. T. Kazemi. Size effect on diagonal shear failure of beams without stirrups. Technical Report 89–8/498S, Center for Advanced Cement–Based Materials, Northwestern University, 1990.

[*Bjerkeli et al.* (1990)] L. Bjerkeli, A. Tomaszewicz, and J. J. Jemsen. Deformation properties and ductility of high–strength concrete. In W. T. Hester, editor, *High–Strength Concrete*, volume ACI, SP-121 of *Second International Symposium on Utilization of High Strength Concrete, Berkeley, California, May*, pages 215–238, May 1990.

[*Broek* (1993)] D. Broek. *Elementary Fracture Mechanics.* Kluwer Academic Publishers, fourth edition, 1993.

[*Brooks et al.* (1987)] J. J. Brooks, A. E. Gamble, and W. A. Al-Khaja. Influence of pulversised fuel ash and a superplasticizer on time–dependent performance of prestressed concrete beams. In *Utilization of High Strength Concrete*, pages 205–214. Tapir, 1987.

[*Büyüköztürk* (1993)] O. Büyüköztürk. Fracture mechanics parameters influencing the mechanical properties of concrete composites. Technical report, Massachusetts Institute of Technology, 1993.

[*Büyüköztürk et al.* (1992a)] O. Büyüköztürk and K. M. Lee. Interface fracture mechanics of concrete composites. In Z. P. Bažant, editor, *Fracture Mechanics of Concrete Structures*, pages 163–168. Elsevier Applied Science, 1992.

[*Büyüköztürk et al.* (1992b)] O. Büyüköztürk and K. M. Lee. Fracture of mortar–aggregate interfaces in concrete composites. In J. C. Maso, editor, *Interfaces in Cementitious Composites*, RILEM Proceedings 18, Toulouse, pages 139–148. E & FN Spon (Chapman & Hall), Oct. 1992.

[*Carpintieri* (1986)] A. Carpintieri. *Mechanical Damage and Crack Growth in Concrete.* Martinus Nijhoff Publishers, 1986.

[*Carpintieri et al.* (1984)] A. Carpintieri and A. R. Ingraffea. *Fracture Mechanics of Concrete.* Martinus Nijhoff Publishers, 1984.

[*Carrasquillo et al.* (1981a)] R. L. Carrasquillo, A. H. Nilson, and F. O. Slate. Microcracking and behavior of high strength concrete subjected to short–term loading. *ACI Journal*, 78:179–186, 1981.

[*Carrasquillo et al.* (1981b)] R. L. Carrasquillo, A. H. Nilson, and F. O. Slate. Properties of high strength concrete subjected to short–term loads. *ACI Journal*, 78:171–178, 1981.

[*Chatterji et al.* (1992)] S. Chatterji and A. D. Jensen. Formation and development of interfacial zones between aggregates and portland cement pastes in cement–based materials. In J. C. Maso, editor, *Interfaces in Cementitious Composites*, RILEM Proceedings 18, Toulouse, pages 3–12. E & FN Spon (Chapman & Hall), Oct. 1992.

[*Danielsen* (1987a)] S. W. Danielsen. Optimizing aggregate properties for high–strength concrete. In *Utilization of High Strength Concrete*, pages 73–84. Tapir, 1987.

[*Danielsen* (1987b)] S. W. Danielsen. Optimizing aggregate properties for high strength concrete. In *Utilization of High Strength Concrete*, pages 73–84. Tapir, 1987.

[*de Larrard* (1990)] F. de Larrard. Creep and shrinkage of high–strength field concrete. In W. T. Hester, editor, *High–Strength Concrete*, volume ACI, SP-121 of *Second International Symposium on Utilization of High Strength Concrete, Berkeley, California, May*, pages 577–598, May 1990.

[*de Larrard et al.* (1987)] F. de Larrard, C. Boulay, and P. Rossi. Fracture toughness of high–strength concrete. In *Utilization of High Strength Concrete*, pages 215–223. Tapir, 1987.

[*de Larrard et al.* (1992)] F. de Larrard and A. Belloc. Are small aggregates really better for making high–strength concrete. *Cement, Concrete, and Aggregates*, 14(1):62–66, 1992.

[*Detwiler et al.* (1989)] R. J. Detwiler and P. K. Mehta. Chemical and physical effects of silica fume on the mechanical behavior of concrete. *ACI Materials Journal*, 86(6):609–614, 1989.

[*Diamond et al.* (1992)] S. Diamond, S. Mindess, Lie Qu, and M. G. Alexander. Sem investigations of the contact zones between rock surfaces and cement paste. In J. C. Maso, editor, *Interfaces in Cementitious Composites*, RILEM Proceedings 18, Toulouse, pages 13–22. E & FN Spon (Chapman & Hall), Oct. 1992.

[*Dundurs* (1969)] J. Dundurs. Edge–bonded dissimilar orthogonal elastic wedges. *Journal of Applied Mechanics*, 36:650–652, 1969.

[*Elfgren* (1989)] L. Elfgren. Rilem, technical commitee 90 FMA. In *Fracture Mechanics of Concrete Structures.* Chapman and Hall, 1989.

[*Elfgren et al.* (1989)] Elfgren and Shah. Rilem workshop. In *Analysis of Concrete Structures by Fracture Mechanics.* Chapman and Hall, 1989.

[*England* (1965)] A. H. England. A crack between dissimilar media. *Journal of Applied Mechanics*, 32:400–402, 1965.

[*Erdogan* (1965)] F. Erdogan. Stress distribution in bonded dissimliar materials with crack. *Journal of Applied Mechanics*, 32:403–410, 1965.

[*Evans et al.* (1989)] A. G. Evans and J. W. Hutchinson. Effects of non–planarity on the mixed mode fracture energy of bimaterial systems. *Acta Metal*, pages 909–916, 1989.

[*Gerstle* (1979)] K. Gerstle. Material behavior under various types of loading. In *Proceedings of Workshop on High Strength Concrete, National Science Foundation*, pages 43–78, 1979.

[*Gettu et al.* (1990)] R. Gettu, z. Bažant, and M. Karr. Fracture properties and brittleness of high–strength concrete. *ACI Materials Journal*, 87(6):608–618, 1990.

[*Giæver et al.* (1987)] N. A. Giæver, E. Høysæter, and H. T. Øderud. High strength concrete - applications in bridge construction. In *Utilization of High Strength Concrete*, pages 573–584. Tapir, 1987.

[*Hammer et al.* (1990)] T. A. Hammer and E. J. Sellevold. Frost resistance of high–strength concrete. In W. T. Hester, editor, *High–Strength Concrete*, volume ACI, SP-121-23 of *Second International Symposium on Utilization of High Strength Concrete, Berkeley, California, May*, pages 457–488, May 1990.

[*Hanna et al.* (1989)] E. Hanna, K. Luke, D. Perraton, and P. C. Aitcin. Rheological behavior of portland cement pastes in the presence of superplasticizer. *ACI–SP 119*, pages 171–188, 1989.

[*He et al.* (1989)] M. Y. He, H. C. Cao, and A. G. Evans. Mixed mode fracture: The four–point shear specimen. *Acta metall. mater.*, 38(5):839–846, 1989.

[*Helland* (1990)] S. Helland. High–strength concrete used in highway pavements. In W. T. Hester, editor, *High–Strength Concrete*, volume ACI, SP-121 of *Second International Sym-*

posium on Utilization of High Strength Concrete, Berkeley, California, May, pages 757–766, May 1990.

[*Hillemeier et al.* (1977)] B. Hillemeier and H. K. Hilsdorf. Fracture mechanics studies on concrete compounds. *Cement and Concrete Research*, 7:523–535, 1977.

[*Holand* (1987)] I. Holand. High–strength concrete: A major research programme. In *Utilization of High Strength Concrete*, pages 135–146. Tapir, 1987.

[*Hua et al.* (1982)] G. Hua, M. W. Brown, and K. J. Miller. Mixed mode fatigue thresholds. *Fatigue of Engineering Materials and Structures*, 5(1):1–17, 1982.

[*Hutchinson* (1990)] J. W. Hutchinson. Mixed mode fracture mechanics of interfaces. *Metal–Ceramic Interfaces*, pages 295–306, 1990.

[*Hutchinson et al.* (1992)] J. W. Hutchinson and Z. Suo. Mixed mode cracking in layered materials. *Advances in Applied Mechanics*, 29:63–191, 1992.

[*Jakobsen et al.* (1987)] B. Jakobsen, A. Eikenes, and T. O. Olsen. Recent development and potentials for high–strength offshore concrete platforms. In *Utilization of High Strength Concrete*, pages 585–607. Tapir, 1987.

[*Kawakami* (1992)] H. Kawakami. Effect of aggregate type on the mechanical behaviour of concrete. In J. C. Maso, editor, *Interfaces in Cementitious Composites*, RILEM Proceedings 18, Toulouse, pages 179–186. E & FN Spon (Chapman & Hall), Oct. 1992.

[*Kim et al.* (1992)] J. K. Kim, H. Mihashi, K. Kirikoshi, and T. Narita. Fracture energy of concrete with different specimen size and strength by wedge splitting test. In Z. P. Bažant, editor, *Fracture Mechanics of Concrete Structures*, pages 561–566. Elsevier Applied Science, 1992.

[*Lee* (1993)] K. M. Lee. *Interface Fracture in High Strength Concrete.* PhD thesis, Massachusetts Institute of Technology, Department of Civil and Environmental Engineering, 1993.

[*Lee et al.* (1994)] K. M. Lee and Oral Büyüköztürk. Fracture mechanics parameters influencing the mechanical properties of high performance concrete. In *ACI 1994 International Conference on High Performance Concrete, Singapore*, Nov. 1994.

[*Leung* (1993)] C. K. Y. Leung. Engineering materials, MIT, lecture notes, 1993.

[*Malyshev et al.* (1965)] B. M. Malyshev and R. C. Salganik. The strength of adhesive joints using the theory of cracks. *International Journal of Fracture Mechancis*, 5:114–128, 1965.

[*Marti* (1989)] P. Marti. Size effect in double–punch on concrete cylinders. *ACI Materials Journal*, 86(6):597–601, 1989.

[*Maso* (1992)] J. C. Maso. Preface. In J. C. Maso, editor, *Interfaces in Cementitious Composites*, RILEM Proceedings 18, Toulouse. E & FN Spon (Chapman & Hall), Oct. 1992.

[*Mat*(1987)] Materials Research Society Symposium. *Microstructural Study of Different Types of Very High Strength Concrete*, volume 85, 1987.

[*Mehta* (1986)] P. K. Mehta. *Concrete: Structure, Properties, and Materials.* Prentice Hall Inc., 1986.

[*Mehta et al.* (1990)] P. K. Mehta and P. C. Aitcin. Microstructural basics of selection of materials and mix proportions for high–strength concrete. In W. T. Hester, editor, *High–Strength Concrete*, volume ACI, SP-121 of *Second International Symposium on Utilization of High Strength Concrete, Berkeley, California, May*, pages 265–286, May 1990.

[*Mitsui et al.* (1992)] K. Mitsui, Zongjin Li, D. A. Lange, and S. P. Shah. A study of properties of the paste–aggregate interface. In J. C. Maso, editor, *Interfaces in Cementitious Composites*, RILEM Proceedings 18, Toulouse, pages 119–128. E & FN Spon (Chapman & Hall), Oct. 1992.

[*Mitsuru et al.* (1986)] S. Mitsuru and K. Mitsunori. Resistance of the cement–aggregate interfacial zone to the propagation of cracks. *Cement and Concrete Research*, 16:653–661, 1986.

[*Monteiro et al.* (1986)] P. J. M. Monteiro and P. K. Mehta. Interaction between carbonate rock and cement paste. *Cement and Concrete Research*, 16:127–134, 1986.

[*Murakami* (1987)] Y. Murakami, editor. *Stress Intensity Factors Handbook.* Pergamon Press, 1987.

[*NAT*(1984)] NATO. *The Role for Fracture Mechanics in Conventional Reinforced Concrete Design*, Advanced Research Workshop on Application of Fracture Mechanics to Cementitious Composites, Sept. 1984.

[*Neville* (1973)] A. M. Neville. *Properties of Concrete.* Wiley and Sons, 1973.

[*Ngab et al.* (1985)] A. S. Ngab, F. O. Slate, and A. H. Nilson. Shrinkage and creep of high–strength concrete. *High Strength Concrete*, ACI SP-87:25–50, 1985.

[*Nilsen et al.* (1992)] U. Nilsen, Sandberg P., and K. Folliard. Influence of mineral admixtures on the transition zone in concrete. In J. C. Maso, editor, *Interfaces in Cementitious Composites*, RILEM Proceedings 18, Toulouse, pages 65–70. E & FN Spon (Chapman & Hall), Oct. 1992.

[*Oumera* (1991)] A. A. Oumera. Crack propagation in the aggregate–mortar interface regions of concrete. Master's thesis, Massachusetts Institute of Technology, Department of Civil and Environmental Engineering, 1991.

[*Penttala et al.* (1987)] V. Penttala and T. Rautanen. Microporosity, creep and shrinkage of high–strength concrete. In *Utilization of High Strength Concrete*, pages 409–432. Tapir, 1987.

[*Randall et al.* (1989)] V. Randall and K. Foot. High strength concrete for pacific first center. *Concrete International*, 11(4), 1989.

[*Rice* (1988)] J. R. Rice. Elastic fracture concepts for interfacial cracks. *Journal of Applied Mechanics*, 55:98–103, 1988.

[*Rice et al.* (1965)] J. R. Rice and G. C. Sih. Plane problems of cracks in dissimilar media. *Journal of Applied Mechanics*, 32:418–423, 1965.

[*Rice et al.* (1977)] Rice and Roy. Microstructure dependence of mechanical behavior of ceramics. *Treatise on Material Science and Technology*, II:199–381, 1977.

[*Roy et al.* (1975)] D. M. Roy and G. R. Gouda. Optimization of strength in cement pastes. *Cement and Concrete Research*, 5(2):153–162, 1975.

[*Ryell et al.* (1987)] J Ryell and J. A. Bickley. Scotia plaza: High strength concrete for tall buildings. In *Utilization of High Strength Concrete*, pages 641–653. Tapir, 1987.

[*Saouma et al.* (1989)] V. E. Saouma, J. J. Broz, E. Brüwiler, and H. Boggs. Fracture properties of dam concrete. *ASCE Journal of Materials in Civil Engineering*, 1989.

[*Sellevold* (1987)] E. J. Sellevold. The function of silica fume in high–strength concrete. In *Utilization of High Strength Concrete*, pages 39–49. Tapir, 1987.

[*Sellevold et al.* (1982)] E. J. Sellevold, O. H. Bager, T. Knudsen, and K. Jensen. Silica fume–cement pastes: Hydration and pore structure. Technical Report BML 82.610, Norwegian Institute of Technology, 1982.

[*Shah* (1979)] S. P. Shah. A summary. In *Proc. of a Workshop on High Strength Concrete*, pages 1–7, 1979.

[*Shah et al.* (1991)] Shah and Carpintieri. Rilem, technical commitee 89 fmt. In *Fracture Mechanics Test Methods for Concrete.* Chapman and Hall, 1991.

[*Shih et al.* (1985)] G. C. Shih and A. DiTommaso. *Fracture Mechanics of Concrete.* Martinus Nijhoff Publishers, 1985.

[*Shih et al.* (1989)] T. S. Shih, G. C. Lee, and K. C. Chang. On static modulus of elasticity of normal–weight concrete. *Journal of Structural Engineering*, 115(10):2579–2587, 1989.

[*Struble* (1988)] L. Struble. Microstructure and fracture at the cement paste–aggregate interface. In *Bonding in Cementitious Composites*, volume 114 of *MRS Symposia*, pages 11–20, 1988.

[*Struble et al.* (1980)] L. Struble, J. Skalny, and S. Mindess. A review of the cement–aggregate bond. *Cement and Concrete Research*, 10:277–286, 1980.

[*Struble et al.* (1983)] L. Struble and S. Mindess. Morphology of the cement–aggregate bond. *Int. J. of Cement Composites and Lightweight Aggregate*, 5:79–86, 1983.

[*Suo* (1989)] Z. Suo. *Mechanics of Interface Fracture.* PhD thesis, Harvard University, Division of Applied Sciences, 1989.

[*Suo et al.* (1989)] Z. Suo and J. W. Hutchinson. Sandwich test specimen for measuring interface crack toughness. *Materials Science and Engineering*, A107:135–143, 1989.

[*Suo et al.* (1990)] Z. Suo and J. W. Hutchinson. Interface crack between two elastic layers. *Int. J. of Fracture*, 43:1–18, 1990.

[*Swamy* (1986)] R. N. Swamy. Properties of high–strength concrete. *Cement, Concrete, and Aggregates*, 1(8):33–41, 1986.

[*Tada et al.* (1985)] H. Tada, P. C. Paris, and G. R. Irwin. *The Stress Analysis of Cracks Handbook.* Paris Productions Inc., second edition, 1985.

[*Teychenné et al.* (1978)] D. C. Teychenné, L. J. Parrot, and C. D. Pomeroy. The estimation of the elastic modulus of concrete for the design of structures. *Building Research Establishment*, 1978.

[*Thorenfeldt et al.* (1987)] E. Thorenfeldt, A. Tomaszewicz, and J. J. Jensen. Mechanical properties of high–strength concrete and application in design. In *Utilization of High Strength Concrete*, pages 149–159. Tapir, 1987.

[*Thorenfeldt et al.* (1990)] E. Thorenfeldt and G. Drangsholt. Shear capacity of reinforced high–strength concrete beams. In W. T. Hester, editor, *High–Strength Concrete*, volume ACI, SP-121 of *Second International Symposium on Utilization of High Strength Concrete, Berkeley, California, May*, pages 129–154, May 1990.

[*Williams* (1959)] M. L. Williams. The stress around a fault or crack in dissimilar media. *Bulletin of the Seismological Soeciety of America*, 49:199–204, 1959.

[*Wittmann* (1986)] F. H. Wittmann. *Fracture Toughness and Fracture Energy of Concrete.* Elsevier, 1986.